Underwater Wireless Optical Communications: Long-range High-data-rate Transmission and Performance Analysis

Tasnim Hamza

ÉCOLE CENTRALE MARSEILLE

N° attribué par la bibliothéque
XXXXX

TITRE:

Communications optiques sous-marines : Transmission longue-portée haut-débit et analyse des performances

THÈSE
pour obtenir le grade de DOCTEUR
délivré par ÉCOLE CENTRALE MARSEILLE
Discipline : Optique, Photonique et Traitement d'Image

Effectuée à l'INSTITUT FRESNEL et l'IFREMER
Présentée et soutenue publiquement par:

Tasnim HAMZA
le 23 mars 2017

Directeur de thèse : M. Salah BOURENNANE
Co-directeur de thèse : M. Mohammad-Ali KHALIGHI
École Doctorale : Physique et Sciences de la Matière

JURY :

Président du jury:	M. Laurent CLAVIER	Université de Lille
Rapporteurs:	M. Pascal CHARGÉ	Université de Nantes
	M. Laurent ROS	Université de Grenoble Alpes
Examinateurs:	M. Jan OPDERBECKE	IFREMER
	M. Pierre LÉON	IFREMER
Invités:	M. Yves CHARDARD	SubseaTech (Marseille)
	M. Chadi GABRIEL	Netatmo (Issy les Moulineaux)
Directeurs de thèse:	M. Salah BOURENNANE	École Centrale de Marseille
	M. Mohammad-Ali KHALIGHI	École Centrale de Marseille

ANNÉE : 2017

ÉCOLE CENTRALE MARSEILLE

N° assigned by library
XXXXX

TITLE:

Underwater Wireless Optical Communications: Long-range High-data-rate Transmission and Performance Analysis

THESIS
to obtain the degree of Doctor of Philosophy
issued by ÉCOLE CENTRALE MARSEILLE
Major: Optics, Photonics, Image Processing

Prepared at FRESNEL INSTITUTE and IFREMER
Presented and defended publicly by :

Tasnim HAMZA
on March 23 2017

Thesis advisor: M. Salah BOURENNANE
Thesis co-advisor : M. Mohammad-Ali KHALIGHI
Doctoral school : Physique et Sciences de la Matière

DOCTORAL COMMITTEE :

Jury President:	M. Laurent CLAVIER	Université de Lille
Rapporteurs:	M. Pascal CHARGÉ	Université de Nantes
	M. Laurent ROS	Université de Grenoble Alpes
Examiners:	M. Jan OPDERBECKE	IFREMER
	M. Pierre LÉON	IFREMER
Invited:	M. Yves CHARDARD	SubseaTech (Marseille)
	M. Chadi GABRIEL	Netatmo (Issy les Moulineaux)
Thesis advisors:	M. Salah BOURENNANE	École Centrale de Marseille
	M. Mohammad-Ali KHALIGHI	École Centrale de Marseille

ANNÉE : 2017

Remerciement

A l'issue de ce travail de recherche, je suis fermement convaincue qu'une thèse de doctorat est loin d'être un travail solitaire. De nombreuses personnes dont la générosité, la bonne humeur et l'intérêt manifestés à l'égard de ma recherche ont contribué à son aboutissement et sa réussite. C'est à ces personnes que je souhaite dédier ces remerciements, en espérant n'oublier personne.

En premier lieu, je remercie chaleureusement mon co-directeur de thèse Monsieur Mohammad-Ali Khalighi, pour la confiance qu'il m'a accordée en acceptant d'encadrer ce travail doctoral, sa grande disponibilité et ses nombreux conseils. Je le remercie pour sa forte implication, sa rigueur sans faille et ses qualités humaines d'écoute et de compréhension tout au long de nos années de collaboration doctoral. Son encadrement a été remarquable et déterminant pour la réussite de ce travail. Mes remerciements vont également à Monsieur Pierre Léon, mon co-encadreur et ingénieur de l'IFREMER pour son excellent encadrement et sa grande disponibilité malgré la distance. Je le remercie d'avoir mis à ma disposition toutes les ressources bibliographiques et matérielles dont j'avais besoin, pour son suivi régulier de mon avancement et pour les nombreuses discussions qui m'ont apporté une compréhension plus approfondie des divers aspects de mon sujet de recherche. Je remercie également mon directeur de thèse Monsieur Salah Bourennane ainsi que Messieurs Vincent Rigaud et Jan Opderbecke de l'institut IFREMER pour leur suivi et leur encadrement.

Ce travail n'aurait pas été possible sans le soutien de la région Provence Alpe Côte d'Azur et de L'Institut Français de Recherche pour l'Exploitation de la Mer (IFREMER) qui m'ont permis, grâce à une allocation de recherches et diverses aides financières, de me consacrer sereinement à l'élaboration de ma thèse.

Je remercie l'Institut Fresnel et son directeur Monsieur Stefan Enoch pour leur accueil chaleureux. Je tiens par la même occasion à remercier le personnel de l'institut surtout Claire, Nelly, Samia, et Marc... Ma gratitude s'adresse particulièrement à Frédéric Forestier et sa famille, qui m'ont accueilli chaleureusement dans leur maison, et m'ont offert un toit durant la préparation de ma soutenance. Je ne vous remercierai jamais assez. Je remercie également tous les membres de l'équipe GSM surtout Madame Caroline Fossati, Monsieur Mouloud Adel et Monsieur Julien Marot qui m'ont aidé à répondre à un grand nombre de questions pratiques et scientifiques. Je tiens aussi à remercier les membres des autres équipes surtout Monsieur Frédéric Lemarquis pour les discussions intéressantes sur les filtres optiques. Je remercie également Monsieur Hassan Akhouayri qui a notablement contribué à ma compréhension des problèmes de l'optique géométrique. De même, je tiens à saluer Imene Garali, Shihe Long et tous mes autres collègues au laboratoire pour nos discussions et les bons moments que nous avons passés ensemble.

Mes remerciements s'adressent également au centre méditerranéen de l'IFREMER à la Seyne sur Mer représenté par son directeur Monsieur Vincent

Rigaud. Je remercie en particulier les membres de l'unité sous-marine et tout particulièrement l'équipe S3E pour leur soutien et leur aide dans la mise en place et la réalisation de mes essais expérimentaux. Je tiens remercie également le staff administratif du centre surtout Cathy Dejouy, Jacques Chabrier, Brigitte.Duchene, ..., pour les efforts qu'ils ont réalises afin que j'achève mon travail dans les meilleures conditions possibles.

Par ailleurs, je souhaiterais adresser ma gratitude aux membres de mon jury de thèse de s'être rendu disponibles pour la soutenance. Je tiens à remercier Monsieur Laurent Clavier, professeur à l'Université de Lille, pour avoir accepter de présider mon jury de thèse. Je tiens à lui assurer ma profonde reconnaissance pour l'intérêt qu'il a porté à mon travail, et pour les remarques et questions pertinentes qu'il a soulevées pendant la soutenance. Je remercie également Monsieur Pascal Chargé, professeur à l'Université de Nantes, et Monsieur Laurent Ros, maître de conférence HDR à l'Université Grenoble Alpes, pour l'honneur qu'ils m'ont faite d'avoir participé à mon jury de thèse en qualité de rapporteurs, pour le temps consacré à la lecture du manuscrit, et pour les nombreuses suggestions et remarques judicieuses qu'ils m'ont indiquées. Je remercie également Monsieur Yves Chardard, directeur de Sub-Sea Tech Marseille, et Monsieur Chadi Gabriel, docteur de l'école centrale de Marseille, pour avoir accepté l'invitation à participer au jury et pour leurs remarques et questions pertinentes et les discussions intéressantes qui en découlaient.

Au terme de ce parcours, je remercie enfin celles et ceux qui me sont chers et que j'ai quelque peu délaissés ces derniers mois pour achever cette thèse. Leurs attentions et encouragements m'ont accompagnée tout au long de ces années. Je suis redevable à mes parents, pour leur soutien moral et matériel et leur confiance indéfectible dans mes choix. Je remercie également un ami cher, qui m'a apporté son soutien, et a fait preuve de beaucoup de patience durant ces trois ans, et n'a pas manqué de m'encourager constamment, mon compagnon Iyed Zahed. Finalement, une pensée toute particulière s'adresse à mon ange Malek, qui est né en cours de chemin, et qui par sa présence, m'a apporté beaucoup de joie et m'a donné le souffle pour aller jusqu'au bout, pour le rendre fier de sa maman.

Cette thèse a été réalisée grâce à un financement IFREMER - Région PACA

À mes parents, en esperant vous rendre fiers

List of Acronyms

APD Avalanche Photo-Diode .

AQ Active Quenching .

ARQ automatic repeat request .

AUV autonomous underwater vehicle .

BER Bit-Error Rate .

BL Beer-Lambert law .

DFE Decision Feedback Equalization .

DMT Discrete Mlti-Tone modulation .

DPIM Digital Pulse Interval Modulation .

EXT Extinction ratio .

FEC Forward Error Correction .

FOV Field Of View .

FSO Free-Space Optical communication .

FWHM Full-Width at Half Maximum .

IFFT Inverse Fast Fourier Transform .

IM/DD Intensity Modulation and Direct Detection .

ISI Inter-Symbol Interference .

LD Laser Diode .

LDPC Low-Density Parity-Check .

LED Light Emitting Diode .

LOS Line-Of-Sight .

LPF Low-Pass Filter .

LR Likelihood Ratio .

LT Luby Transform .

LTI Linear and Time-Invariant .

MAP Maximum A Posteriori estimation .

MIMO Multi-Input Multi-Output .

ML Maximum Likelihood .

MMSE Minimum Mean Square Error .

MPPC Multi-Pixel Photon Counters .

NLD Non-Linear Distortion .

OFDM Orthogonal Frequency Division Multiplexing modulation .

OOK On-Off Keying .

PAM Pulse Amplitude Modulation .

PAPR Peak-to-Average Power Ratio .

PD Photo-Detector .

PIN Positive Intrinsic Negative diode .

PMT Photo-Multiplier Tube .

PPM Pulse Position Modulation .

PQ Passive Quenching .

PSK Phase Shift Keying .

QAM Quadrature Amplitude Modulation .

QPSK Quadrature Phase Shift Keying .

RF Radio-frequency .

ROV Remotely-Operated Vehicle .

RS Reed-Solomon .

Rx Receiver .

SC Single Carrier .

SIM Sub-carrier Intensity Modulation .

SiPM Silicon Photo-Multiplier .

SNR Signal-to-Noise Ratio .

SPAD Single Photon Avalanche Diodes .

TDE Time Domain Equalization .

Tx Transmitter .

TZ Trans-impedance circuit .

UWOC Under-Water Optical Communication .

VLC Visible Light Communication .

VSF Volume Scattering Function .

WHOI Woods Hole oceanographic institution .

ZF Zero-Forcing .

List of Figures

List of Tables

Contents

Chapter 1

Introduction

Contents

1.1 General context

1.1.1 Interest in underwater environment

Water basins including oceans and lakes cover almost the third quarter of the earth surface, and play an important role in maintaining life on earth, including climate regulation, and oxygen production, for instance. Human kind is more and more relying on oceans for transportation, food production, bio fuel extraction, mineral exploitation, climate change monitoring, pollution monitoring, etc. Despite these critical issues, our knowledge of underwater environment remains very limited, often restricted to shallow waters, while deep waters remain a mystery, and as a matter of fact, by far less known than space. This is mainly due to the hostility of the water body, lacking oxygen, and exhibiting extremely high pressures.
This significant lack of knowledge of such important resources has raised a growing awareness within the scientific community over the last decades about the urgent and critical need for a careful monitoring, exploration, and exploitation of marine environment. Indeed, the human activities underwater have recently witnessed a important expansion thanks to the development and maturing of underwater robotics, including remotely-operated vehicles (ROVs) and autonomous underwater vehicles (AUVs). These last are able to navigate in difficult-access underwater locations, and are employed along with underwater sensor networks, for instance, to collect various data. However, the proper use of these latter is conditioned on the development of efficient, high bandwidth, and reliable communication solutions underwater.

1.1.2 Underwater Communication technologies

Classically, cabled or fibre-based techniques are used for underwater communications. They offer several advantages including high speed and reliable communication links. However, their use can be challenging in difficult-access locations and in deep sea as they will limit the range and manoeuvrability of the underwater vehicles. In addition, cables can easily be twisted by the underwater wildlife, and would consequently require relatively expensive maintenance operations. In such cases, there is a high interest in wireless communication techniques.
Wireless communication solution in sub-sea environments are expected to meet strict requirements such as a large bandwidth enabling high data transmission rates to handle large size data and reliable information transfer. The main communication solutions considered in this context are radio frequency (RF), acoustics, and optical communications. RF waves suffer from high attenuation in water, and their propagation range is though limited to a few meters. Acoustic waves are a strong alternative thanks to the ease of sound propagation in water. Although widely employed in practice for long range links, and despite the tremendous progress made in this field, acoustics-based communication underwater suffers from very limited bandwidth. For these reasons, a growing interest is steered toward optical communications. These latter provide unprecedentedly high data rates (on the order of Mbps to Gbps) for short and moderate ranges (up to several hundreds of meters typically) thanks to the large available bandwidth. Also, due to the high propagation speed of optical waves in water, optical transmission does not practically suffer from delay latency. Therefore, optical communication is regarded as an attractive alternative (or a potential complementary) solution to acoustic communication.

1.1.3 Wireless optical communication history

The interest in developing communication solutions in underwater environments dates back to Leonardo da Vinci [1]. The first reported practical uses of underwater acoustics for communicating underwater is reported to date to the early 1900s. After 1930, underwater telegraph systems employing acoustics waves were widely employed in submarines [2].
Interest toward underwater optical communications emerged a bit latter, during the 1970's and 1980's. The majority of the related work examined the feasibility of communicating with submarines from air-crafts or satellites. This application presented a number of critical challenges, since it required the laser signal to propagate long distances through the atmosphere, through the air/water interface, and finally through the challenging underwater environment. This required high power, high repetition rate blue/green sources . Only recently, with the advance in optroelectronics, optical underwater communication has revealed to be a viable alternative to the traditional acoustic communications.
Today, with the growing use of wireless optical links in the air, made the use of optical technologies for underwater communication on medium ranges appears to

be very promising. For instance, the free-space optical (FSO) communications technology, which is nowadays quite mature, has contributed to the development of cost effective, high sensitive optoelectronic devices (e.g. photo-detectors). Besides, the great interest toward visible light communications (VLC) has resulted in the manufacturing of energy-efficient light source technologies, i.e., light emitting diodes (LEDs).

1.2 Thesis objectives

As explained earlier, underwater wireless optical communications (UWOCs) have the advantages of high data rate transmission over moderate distances, up to several hundreds of meters. However, establishing an optical communication link is very challenging in underwater environment, where the optical signal is subject to high attenuation. Although several works have focused on the characterization of the underwater propagation channel, many related issues remain open. Among these, the effect of a background noise, such as solar rays underwater, on the system performance. Besides, the typical low levels of received signal imply the need for employing highly sensitive photo-detection technologies, so as to enable long range communications.

The objective of this thesis is first to analyze the performance of data transmission links based on commonly-used optoelectronic components for UWOCs. We particularly focus on the effect of solar background noise on the link performance, an open issue rarely considered in the literature. This can have an considerable effect on the system performance, particularly for shallow depths. Then, we study the feasibility of employing a very recent and promising photo-detector component, the Silicon photo-multiplier (SiPM). These components are very sensitive to low light intensities, and appear to be specially advantageous to use in underwater communication context in the aim of enabling longer transmission distances. We investigate the use of appropriate signaling schemes, including modulation schemes and channel equalization, so as to improve the data transmission rate and link span. Lastly, we validate a part of our theoretical results through a series of experiments.

More specifically, the thesis outline is presented below.

1.2.1 Thesis outline

In **Chapter** 2, we provide a literature survey of the current research on UWOCs. We present an overview of the state-of-the-art of this technology, the related challenges, the employed systems and components, and the reported achieved performance. The relevant related publications, research works, prototypes, and commercialized products are presented.

In **Chapter** 3, we study the effect of the background noise generated by solar radiations on the communication link performance. First, we present an analytic generic model of the solar noise and then study its impact on the underwater wireless optical communication link performance in terms of the link bit error rate (BER).

Our study considers three different photo-detector types, in order to highlight the practical limitations of establishing an UWOC link for each case. we show how the sensitivity to solar radiations varies depending on both the operation depth and the receiver characteristics. The results we present are insightful for UWOC system designers and also users when these links have to be deployed in relatively shallow waters where the propagation medium cannot be considered as dark.

In **Chapter** 4, we investigate and highlight the interest of employing SiPMs in the UWOC context. As explained, these components stand out for their high sensitivity to low optical signal levels, down to a single photon, and are considered in order to increase significantly the transmission range. Furthermore, we investigate different modulation techniques to be employed with SiPMs, in the aim of further improving the link performance.

In **Chapter** 5, we investigate the bandwidth limitations arising from both the underwater optical channel, and transmitter (Tx) and receiver (Rx) components, and determine the scenarios where they may effectively degrade the system performance in terms of data rate and link span. Then, we investigate the use of channel equalization technique in the frequency domain, which is a reliable and low complexity solution to surpass the bandwidth limitation imposed by the optoelectronic components. We show the improvement in the link data rate by using this promising solution.

In **Chapter** 6, we provide a description of the experimental setup we developed in collaboration with IFREMER, and the different electronic and optical components used therein. We present the main obtained results and compare them to the theoretical results we obtained previously.

Lastly, Chapter 7 concludes the thesis and gives some perspectives for future work.

1.2.2 Main contributions

In summary, the main contributions of this thesis are:

- Proposing an analytic expression of power attenuation within underwater optical channel, more adapted to a diffuse light beam such that of an LED, avoiding hence the resorting to computationally complex Monte Carlo-based simulations.

- Presenting an analytic generic model of the solar noise underwater, often neglected in previous works, and investigating its impact on a UWOC link performance.

- Investigating the suitability and feasibility of employing SiPMs in UWOC context, and demonstrating their interest for establishing long-range high-rate communication links.

- Comparing different modulation techniques to use with SiPM-based receives in the aim of enhancing the system performance.

- Investigating the use of frequency domain channel equalization to improve the maximum achievable communication distances and the tolerable data transmission rates.
- Designing and implementing a test-bed in order to validate a part of the theoretical results.

1.2.3 Author's publications

- M. A. Khalighi, C. Gabriel, T. Hamza, S. Bourennane, P. Léon, and V. Rigaud. *Underwater Wireless Optical Communication; Recent Advances and Remaining Challenges*. 16th International Conference on Transparent Optical Networks (ICTON), pp.1 – 4, Graz, Austria, Jul. 2014.
- T. Hamza, M. A. Khalighi, S. Bourennane, P. Léon, and J. Opderbecke. *On the Suitability of Employing Silicon Photomultipliers for Underwater Wireless Optical Communication Links*. IEEE 10th International Symposium on Communication Systems, Networks and Digital Signal Processing (CSNDSP), Istanbul, Turkey, Jul. 2016
- T. Hamza, M. A. Khalighi, S. Bourennane, P. Léon, and J. Opderbecke. *Investigation of Solar Noise Impact on the Performance of Underwater Wireless Optical Communication Links*. Optics Express, Vol. 24, Issue 22, pp.25832 – 25845, Oct. 2016.

Chapter 2

Overview of the State-of-the-Art

Contents

2.1 Introduction

The objective of this chapter is to provide a literature survey of current research on UWOCs. We present an overview of the state-of-the-art of underwater optical communications, the related challenges, the employed systems and components, and the reported achieved performance. Thus, we present a review of relevant related publications, research work, and mature technology products and prototypes.

In Section 2.2, we make a comparison of potential communication technologies underwater. We show that optical communication is of great interest compared to the widely used acoustic waves, offering several advantages, including high data rates. For a reliable communication establishment, it is mandatory to characterize the underwater optical channel. Thus, in Section 2.3, we focus on the overview and characterization of the aquatic optical channel. We study the physical phenomena which impact the propagation of light underwater, and establish a classification of waters upon their bio-optical characteristics. Based on this, we provide a model of optical power loss within the aquatic channel. We also review the channel impulse response and in particular the channel delay dispersion. In Section 2.4, we present the existing transmitter and receiver technologies employed in UWOCs, along with the mainly used signal processing techniques. Next, in Section 2.5, we present some practical challenges an UWOC system is facing, which can be perilous to the system performance. Then, some existing prototypes and commercialized UWOC systems are presented in Section 2.6. Lastly, Section 2.7 concludes the chapter.

2.2 Underwater communication technologies

In this section, we provide a brief overview of exist technologies employed for wireless communications in underwater environments, i.e. RF, acoustics, and optical communications. Presenting the main related works in the literature, we list the main features and impediments of the three communication technologies.

2.2.1 Acoustic communications

Acoustic communication is currently the most common technology for sensing and data transmission underwater and is regarded as a benchmark to which other underwater communication solutions are usually compared [3]. It is employed for various applications, for instance, marine research, oceanography, offshore oil industry, and defense [4]. In contrast to RF waves, and due to the ease of propagation in water, acoustic waves allow the establishment of communication links over relatively long ranges up to hundred of Kilometers [5]. Nevertheless, underwater acoustic communication faces a number of challenges. The major one is the hostility of the underwater acoustic channel. The signal suffers from extremely variable delays (depending on the water conditions such as salinity, temperature, and pressure) and is subject to relatively long latency, multi-path propagation, and fading. This results in some cases in poor transmission quality [5]. Also, given the limited channel bandwidth, this technology is not adapted to high data rate transmission and the data rate is typically limited to few Kbps [6]. Furthermore, the underwater acoustic antennas are bulky and expensive (often not adapted to the underwater system compacteness requirements), and energy greedy. This is due to the long transmission distance and the need for complex signal processing at the receiver to compensate channel distortion and interference. Lastly, acoustic communication systems suffer from several external noise sources such as submarines, ships, and mammals.

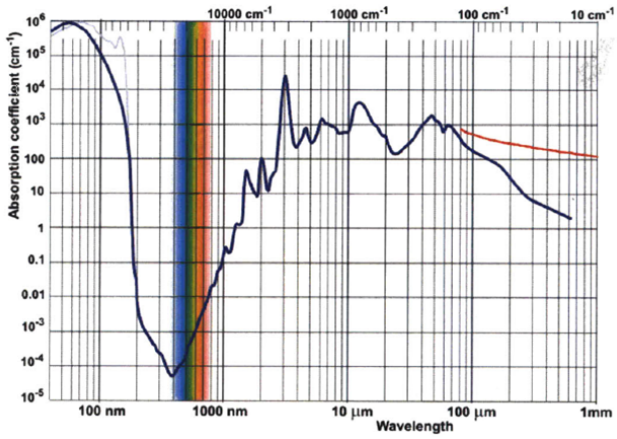

Figure 2.1: Absorption spectrum of electromagnetic radiation underwater, reproduced from [14].

2.2.2 RF communication

RF-based communication is employed in a number of applications in free space. The main strength of RF-based transmission is its capability of operating over long distances, and at high data rates.
Several research studies were focused on employing RF waves for underwater communication, e.g. [7, 8, 9]. However, the use of this technology is limited to very short links due to the high absorption of RF waves in water [3], see Fig. 2.1. Basically, Rf waves with extremely low frequency (ELF) band ($30 - 300$ Hz [10]) have been used for very low data rate long range communication between submarines. An RF-based communication is reported in [11], enabling MHz transmission over a distance of 100 m, yet requiring sophisticated and large antennas and a high transmission power on the order of 100 W.
In [12], a comparison of RF and acoustic communications is carried out, confirming the suitability of RF waves to short range communication with low data rates. It is reported to achieve 6 m link distance at 100 KHz, 16 m at 10 KHz and 22 m at 1 KHz. A solution based on multi-input multi-output (MIMO) configuration and quadrature phase shift keying (QPSK) modulation was proposed in [13] which was reported to achieve 48 Kbps over a distance of 2 Km.

2.2.3 Optical communication

Given the limitations of acoustic and RF technologies, UWOCs draw attention as an interesting solution, offering several advantages including unprecedentedly high data rates (on the order of tens to hundreds of Mbps) for relatively short ranges [15] (up to 200 m) thanks to the large available bandwidth. This property boosts the application scope, for instance, allowing the transmission of multimedia data with high definition, e.g. for the purpose of oceanographic monitoring. Furthermore, due

to the high propagation speed of optical waves in water, optical transmission does not practically suffer from latency [16]. Therefore, optical communication is regarded as an attractive alternative (or a potential complementary [17]) solution to long range acoustic communication [18, 19]. As a matter of fact, UWOC uses the visible band of the electromagnetic spectrum, where water is relatively transparent to light and absorption takes its minimum value (see the next section). Furthermore, UWOCs employ on the existing and mature opto-electronic components already developed and tested for fiber optic and free-space optical (FSO) communications in the air (e.g. high sensitive photo-detection technologies), which make the related systems reliable and cost-effective. Exemple of UWOC application are presented in Fig. 2.2.

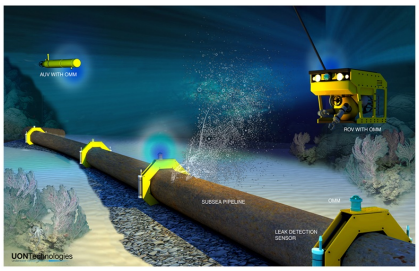

(a) Underwater oil and gas pipelines monitoring with UWOC networks [20].

(b) UWOCs employed for underwater envirmental monitoring [21].

Figure 2.2: Example of UWOC applications.

A comparison of the different aforementioned underwater communication technologies is presented in Table 2.1. Focusing on UWOC, we provide in the following a literature review of the related research work. Meanwhile, we explain the main challenges facing the optical signal, and the establishment of a reliable UWOC in general.

2.3 Underwater wireless optical channel

Modeling and characterizing the underwater optical channel is a key step for efficient, reliable, and robust UWOC system design. In this section, we first present the main challenges that faces light propagation within seawater, i.e., absorption and scattering. Then, we scrutinize the water classification models based on the related optical properties. Next, we present optical power attenuation model within the aquatic channel and investigate the channel impulse response.

2.3.1 Absorption and scattering

The optical signal underwater is subject to strong attenuation mainly due to absorption and scattering. The absorption phenomenon consists in a loss of intensity

Table 2.1: Comparison of different underwater communication technologies, adapted from [10]

Parameter	Acoustic	RF	Optical
Speed	1500 m/s	$\approx 2.25\,10^8$ m/s	$\approx 2.25\,10^8$ m/s
Data rate	∼ Kbps	∼hundred of Kbps	up to Gbps
Range	hundred of kilometers	up to ≈ 10 m	up to 100 m
Bandwidth	≈100 KHz	∼MHz	∼GHz
Tx power	tens of Watts (typical value)	up to hundred of Watts	few Watts
Attenuation	Distance and frequency dependent (0.1-4 dB/Km) [22]	Frequency and conductivity dependent $3.5 - 5$ dB/m [23]	0.1 dB/m (Deap ocean) - 10 dB/m (Shallow turbid)[24].

of the optical beam, resulting from the conversion of some photons' energy to another form, e.g. thermal. The scattering process consists in the change of direction angle of some photons, which deviate from their initial direction. Absorption and scattering are described by two coefficients (in m^{-1}) a and b, respectively. Let us consider an elemental volume of water ΔV, which has a thickness Δr, as shown in Fig. 2.3. The water is illuminated by a monochromatic collimated beam at a fixed wavelength λ, of spectral radiant power P_i. A certain amount of the incident power is absorbed by the water, denoted here by P_a, whereas another part of it is scattered. In order to model this latter, let us consider $P_\mathrm{s}(\lambda, \Psi)$, a portion of scattered light over a given angle Ψ (see Fig. 2.3). The total scattered power, denoted by $P_\mathrm{s}(\lambda)$, is defined as the summation of $P_\mathrm{s}(\lambda, \Psi)$ over all angles Ψ. The remaining power, P_t passes through the water unaffected. By conservation of energy, we have:

$$P_\mathrm{i}(\lambda) = P_\mathrm{a}(\lambda) + P_\mathrm{t}(\lambda) + P_\mathrm{s}(\lambda). \tag{2.1}$$

We define the absorbance A as the fraction of incident power, absorbed within ΔV. Likewise, the fraction of incident power, scattered in all direction is defined by the scatterance B; A and B being functions of the wavelength λ. Thus,

$$A(\lambda) = \frac{P_\mathrm{a}(\lambda)}{P_\mathrm{i}(\lambda)}, \quad B(\lambda) = \frac{P_\mathrm{s}(\lambda)}{P_\mathrm{i}(\lambda)} \tag{2.2}$$

In order to accurately describe the inherent water optical properties, it is more useful to define A and B per unit of distance, which comes to consider the already defined coefficients a and b. They are obtained by taking the limit of A and B as the water

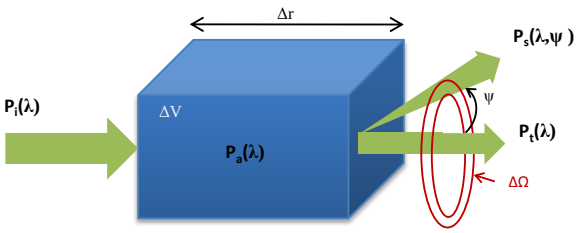

Figure 2.3: Illustration of absorption and scattering factors, reproduced from [10]

column thickness becomes infinitely small, and thus Δr tends to zero:

$$a(\lambda) = \lim_{\Delta r \to 0} \frac{\Delta A(\lambda)}{\Delta r}, \quad b(\lambda) = \lim_{\Delta r \to 0} \frac{\Delta B(\lambda)}{\Delta r} \tag{2.3}$$

The sum of these two parameters gives the overall beam attenuation coefficient c (in m^{-1}), which describes the loss of optical power per meter:

$$c(\lambda) = a(\lambda) + b(\lambda) \tag{2.4}$$

A commonly adopted model for quantifying the attenuation of light intensity underwater at a distance Z from the optical source, is the Beer-Lambert (BL) law, which considers an exponential decay of the signal level [25, 26]. The BL law describes power loss of a collimated light beam due to the combined effects of scattering and absorption. Denoting L_{ch} the aquatic channel power, we have :

$$L_{\mathrm{ch}}(\lambda, Z) = e^{(-c(\lambda)\, Z)}, \tag{2.5}$$

The strong assumption adopted by this law is that each scattered photon is considered as lost, and does not contribute to the value of the optical intensity at distance Z.
A common metric of the optical power attenuation underwater is given by the e-folding distance also called the attenuation length; it is defined as the distance over which the intensity of the light beam decreases by a factor e according to (2.5). For instance, turbid and clear waters have typical e-folding distances of 1 and 25 m, respectively [27].

2.3.1.1 Absorption

Absorption has a great impact on the achievable link span because it dramatically reduces the number of photons that reach the receiver. This process is highly dependent on the wavelength as well as on the composition of sea water and the concentration its optically influential components. The total absorption in water can be attributed to four main factors:

1. **Pure seawater**, involving water molecules and dissolved salts such as NaCl, $CaCl_2$ and KCl, which mainly contribute to its absorption spectrum. The

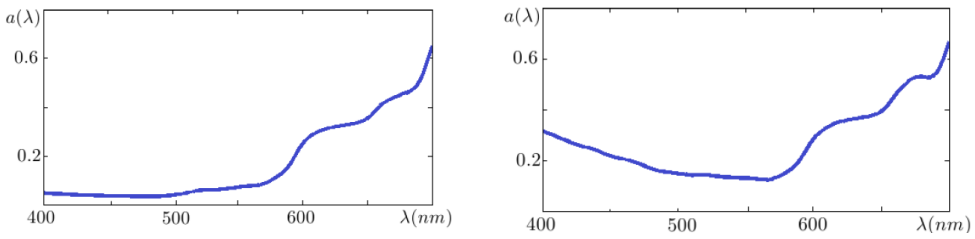

(a) (b)

Figure 2.4: Combined absorption spectra for different water types (a) open ocean and (b) coastal waters. Reproduced from [29]

related absorption effect is notably weak in the blue-green region of the visible spectrum; i.e. $\lambda \in [400 - 500\,\text{nm}]$ [28]. The associated absorption factor is denoted by a_{w}.

2. **Phytoplanktons**, which are photosynthesizing, microscopic marine organisms, and contain colored pigments including Chlorophyll which absorb a large amount of light. Chlorophyll is reported to dominate the absorption behaviour of phytoplanktons, so that the overall phytoplankton absorption coefficient a_{phy} is approximated by that of Chlorophyll [29], whose spectrum shows a peak around blue-green spectral region.

3. **Color dissolved organic material (CDOM)** also known as Gelbstoff, is composed of decaying organic matters or yellow substances from broken plant tissue, which turns into humic and fulvic acids that absorb in the blue region at $420 - 450\,\text{nm}$ [10]. Their concentration is relatively low in open waters and high in coastal waters. The related absorption coefficient is denoted by a_{g}.

4. **Non-algal materials**, which are composed of living organic particles (for instance bacteria, zooplankon, etc.). Although very different, they are grouped due to similar absorption behaviors. Their absorption coefficient is denoted by a_{n}.

The overall absorption of seawater can be written as the sum of the absorption coefficients of each of its aforementioned components multiplied by their concentration, denoted by C, as follows:

$$a(\lambda) = a_{\text{w}}(\lambda)\, C_{\text{w}} + a_{\text{phy}}(\lambda)\, C_{\text{phy}} + a_{\text{g}}(\lambda)\, C_{\text{g}} + a_{\text{n}}(\lambda)\, C_{\text{n}} \tag{2.6}$$

Typical absorption spectra of open ocean and coastal waters are presented in Fig. 2.4. The minimum absorption window is around $400-500\,\text{nm}$ for open ocean, and around $520 - 570\,\text{nm}$ for coastal waters.

2.3.1.2 Scattering

The scattering process, which causes the photons to deviate away from their original trajectory, is regarded as another major challenge in underwater optical

links. Indeed, the spatial spreading of the optical beam reduces the photon density captured at the receiver plane, and thus reduces the intensity of the received signal. Moreover, scattering can cause temporal spreading of the transmitted pulses due to scattered photons reaching the receiver. In fact, such scattered photons will travel a longer path than those reaching the Rx through a straight line. This is illustrated in Fig. 2.5. This pulse spreading (i.e. channel delay spread) can result in inter-symbol interference (ISI) when working at relatively high bit rates [10].
Scattering is reported to be sparsely dependent on the light wavelength (unlike absorption). It is mainly caused by suspended particulates present in water, and consequently is highly dependent on their concentration. Thus, scattering is more dominant in particulate-rich coastal areas than in open seas. In clearer waters, scattering is caused by the change of the water refractive index (due to variations in pressure, salinity and temperature), which results in the reflection or refraction of the light.

Mathematical description of scattering The volume scattering function (VSF) $\beta(\psi, \lambda)$ describes the ratio of the intensity of scattered light to the incident irradiance, per unit volume [30]. We consider two main assumptions for mathematical derivation of VSF. First, the water is assumed to be isotropic, so that its influence on the incident light is the same in all directions. Secondly, the incident light is assumed to be unpolarised. If these two assumptions are met, then scattering is azimuthally symmetric and would depend only on the scattering angle with respect to original path direction. In this case, the scatterance, defined in (2.2), describes the fraction of the incident scattered power scattered through an angle ψ, into a solid angle $\Delta\Omega$ centered on ψ, as shown in Fig. 2.3. Then, the VSF is given by:

$$\beta(\psi, \lambda) = \lim_{\Delta r \to 0} \lim_{\Delta\Omega \to 0} \frac{\Delta B(\psi, \lambda)}{\Delta r \Delta\Omega} \tag{2.7}$$

The scattering coefficient $b(\lambda)$, which resumes the contributions of scattering events over all angles, is obtained as follows:

$$b(\lambda) = 2\pi \int_0^{\pi} \beta(\psi, \lambda) \sin(\psi)\, \mathrm{d}\psi \tag{2.8}$$

Main related work Several previous works have considered the characterization of the scattering process within water. In [31], measurements of the VSF of various types of water was presented based on laboratory experiments and performance prediction models. It was concluded that a collimated beam (such as a laser beam) is scattered mostly in the forward direction. This finding was confirmed in [32], where the authors stated that clear ocean waters can be considered as strongly forward scattering. For this case, a single scattering approximation as assumed by BL law can effectively be adopted. However, for the case of more turbid waters, multiple

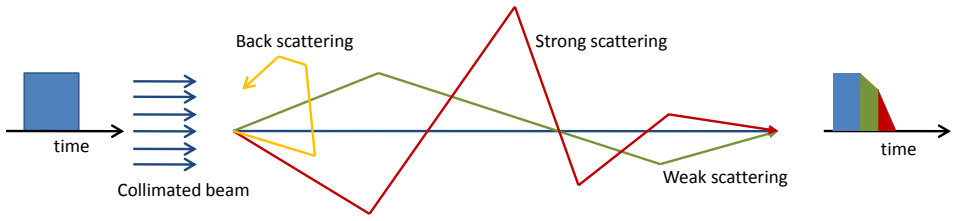

Figure 2.5: Illustration of temporal spreading caused by the scattering phenomenon

scattering events are more likely to happen, which results in a higher received signal intensity than that predicted by BL law. In [33], the authors presented the spatial and angular effects of scattering on a laser link using the radiative transfer equation (RTE). They demonstrated how captured scattered light by the receiver discredits the BL law approximation for relatively turbid waters. The effect of spatial and temporal scattering within turbid waters was further investigated in [34], for the cases of PSK and QAM-based modulations and demonstrated laser-based transmission link over a range up to 100 m. In [16], Gabriel *et al.* simulated the trajectory of propagating photons within an UWOC link using an elaborate Monte Carlo simulator, and demonstrated to which extent the BL law is pessimistic regarding the received light intensity at a given distance as water turbidity increases. As explained, the scattering impact becomes more significant in higher-turbidity waters, and consequently it is more likely that multiple scattered photons reach the Rx plane.

2.3.2 Water classifications

Several works have attempted to provide an optical classification of natural waters, based on their optical properties. To do so, particular attention has been devoted on the attenuation as a function of depth D, of the downward solar irradiance $E_{\mathrm{d}}(\lambda, D)$ (in $\mathrm{W/m^{-2}}$), which is defined as the radiant flux (power) propagating downward (with respect to the zenith axis) in the water and received by a surface per unit area. Indeed, commonly cited models in the literature (that we will present hereafter) classify water types according to the spectra of the attenuation coefficient of E_{d}, that we denote by $K_{\mathrm{d}}(\lambda, D)$ (in $\mathrm{m^{-1}}$). Parameter K_{d} is also referred to as downward diffuse attenuation coefficient.
Light attenuation in water, and consequently K_{d}, depend mainly on the level of water turbidity [35], defined in terms of the concentration of its optically active components [36]. A common hypothesis is that the main dissolved particle within open waters contributing to light attenuation, is the phytoplankton [36, 37]. The concentration of phytoplankton in sea waters is expressed in terms of the concentration of Chlorophyll-a, regarded as the major photosynthetic pigment underwater [36]. Thus, in analysing water optical properties, we need to consider the effects of both pure sea water and the Chlorophyll concentration [37].
The bio-optical models presented in the following aim to describe the relationship

between the Chlorophyll concentration and the resultant coefficient K_{d}.

2.3.2.1 Jerlov's classification of sea waters

Jerlov conducted a series of experiments in various regions to measure and analyze the transmittance of downward irradiance, defined as the ratio of E_{d} at a given depth D to the value at sea surface, as follows:

$$t(\lambda, D) = \frac{E_{\mathrm{d}}(\lambda, D)}{E_{\mathrm{d}}(\lambda, D = 0)} \tag{2.9}$$

These studies were conducted for wavelengths between 310 and 700 nm. The main results of his work can be found in [36, 38]. We have reproduced in Fig. 2.6 the corresponding measured irrandiance transmittance for $D = 1\,\mathrm{m}$, for various water types. Jerlov distinguished 14 different types of ocean waters referred to as the indexes I, IA, IB, II and III for open ocean waters, and indexes 1 to 9 for coastal waters [35]. Types I and 1 correspond to the clearest whereas types III and 9 correspond to the most turbid waters. The Jerlov types I-III are referred to as case 1 waters, where phytoplanktons are predominate (case of open ocean waters), while types 1-9 are referred to as case 2 waters, where yellow matters and terrigenous particles contribute predominately to the water optical properties [35]. These latter differ in the absolute value and spectral distribution of the downward irradiance attenuation coefficients. For instance, we have shown in Fig. 2.7 the mean values of $K_{\mathrm{d}}(\lambda)$ for the water depth range of 0-10 m, this for waters type I, II, 1, 5, and 9.
Although widely considered in the literature, Jerlov's water classification is often criticized for several reasons. First, it considers the optical properties of the water basins in general, without stating the specific contribution of the various water constituents [36]. Second, the classification is discrete and limited to particular types and classes of ocean waters where the measurements have been conducted. In addition, Jerlov did not provide any analytic relationship between his classification types and the related coefficients K_{d}. Thus, the related conclusions and findings can not be extended to other different water conditions. Moreover, Woźniar and *al.* reported in [36] that the spectra of K_{d} provided by Jerlov are considerably different from more recent experimental data. These limitations reduce the scope of applicability of Jerlov's classification. We present In the sequel some more recent water classifications, which are particularly distinguished by their continuous nature (i.e. being applicable to any water type, in contrast to the discrete set of water types considered by Jerlov).

2.3.2.2 Smith and Baker bio-optical classification

The classification of natural waters provided by Smith and Baker has the advantage of combining the biological characteristics and optical types of water components. It establishes an analytic relationship between the K_{d} coefficients and Chlorophyll

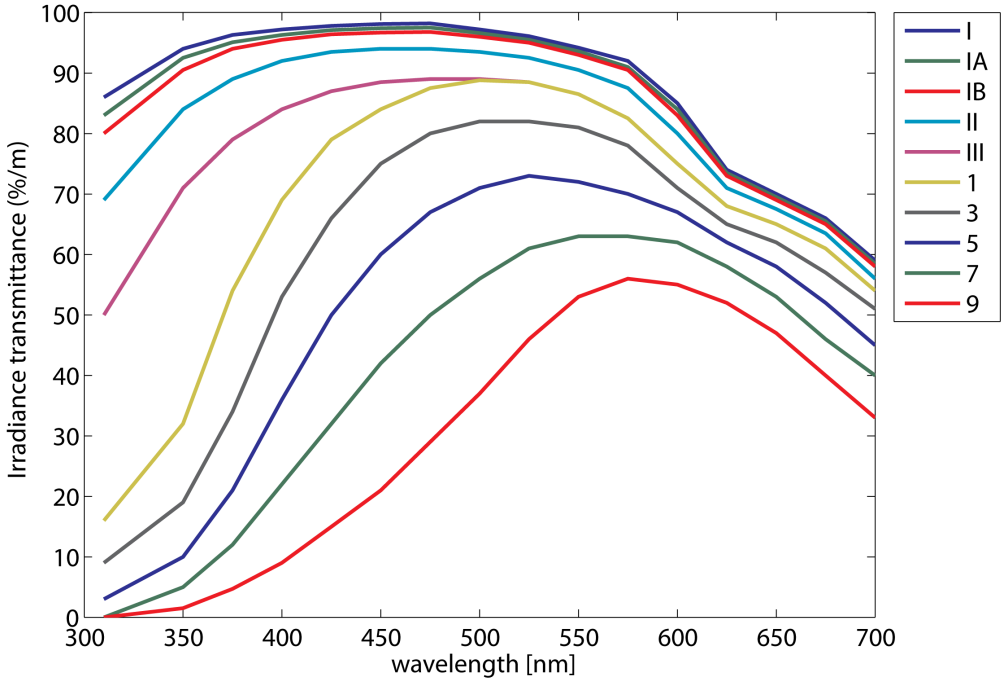

Figure 2.6: Jerlov's water mass classification based on transmitance, $D = 1\,\mathrm{m}$ [39].

a concentration C_{cl} as follows:

$$K_{\mathrm{d}}(\lambda) = \begin{cases} K_{\mathrm{w}}(\lambda) + k_{\mathrm{c},1}(\lambda)\,.\,C_{\mathrm{cl}} & \text{if } C_{\mathrm{cl}} < 1\,\mathrm{mg/m^3} \\ K_{\mathrm{w}}(\lambda) + K_{\Delta,2}(\lambda) + k_{\mathrm{c},2}(\lambda)\,.\,C_{\mathrm{cl}} & \text{if } C_{\mathrm{cl}} > 1\,\mathrm{mg/m^3} \end{cases} \tag{2.10}$$

where K_{w} is the downward irradiance attenuation due to pure water, and $K_{\Delta,2}$ denotes the attenuation due to optically active components with the exception of photosynthetic pigments, whose light attenuation contribution is provided by the factor $k_{\mathrm{c},1}$ and $k_{\mathrm{c},2}$ for small and high Chlorophyll concentrations, respectively. Values of K_{w} were obtained by experimental measurements in Sargasso Sea, where optically active substances were reported to be totally absent. An exhaustive table of values of the parameters in (2.10) can be found in [36] for a range of λ from 350 to 700 nm.

The main strength of Smith and Baker model is the fact that it provides a continuous classification of sea waters (in contrast to Jerlov's), where the C_{cl} is adopted as the optical water type index. However, it has some drawbacks due to the implicit adoption of several simplification hypotheses. For example, this model assumes that the light attenuation due to pigments is constant as a function of Chlorophyll concentration. In other words, it is assumed that $k_{\mathrm{c},1}$ is constant for $C_{\mathrm{cl}} < 1\,\mathrm{mg/m^3}$ and $k_{\mathrm{c},2}$ is constant $C_{\mathrm{cl}} > 1\,\mathrm{mg/m^3}$; however, these parameters significantly vary with C_{cl} [36]. Furthermore, for $C_{\mathrm{cl}} < 1\,\mathrm{mg/m^3}$, the contribution in light attenuation of other particulates (e.g. dissoleved organic matters) than pigment is neglected by

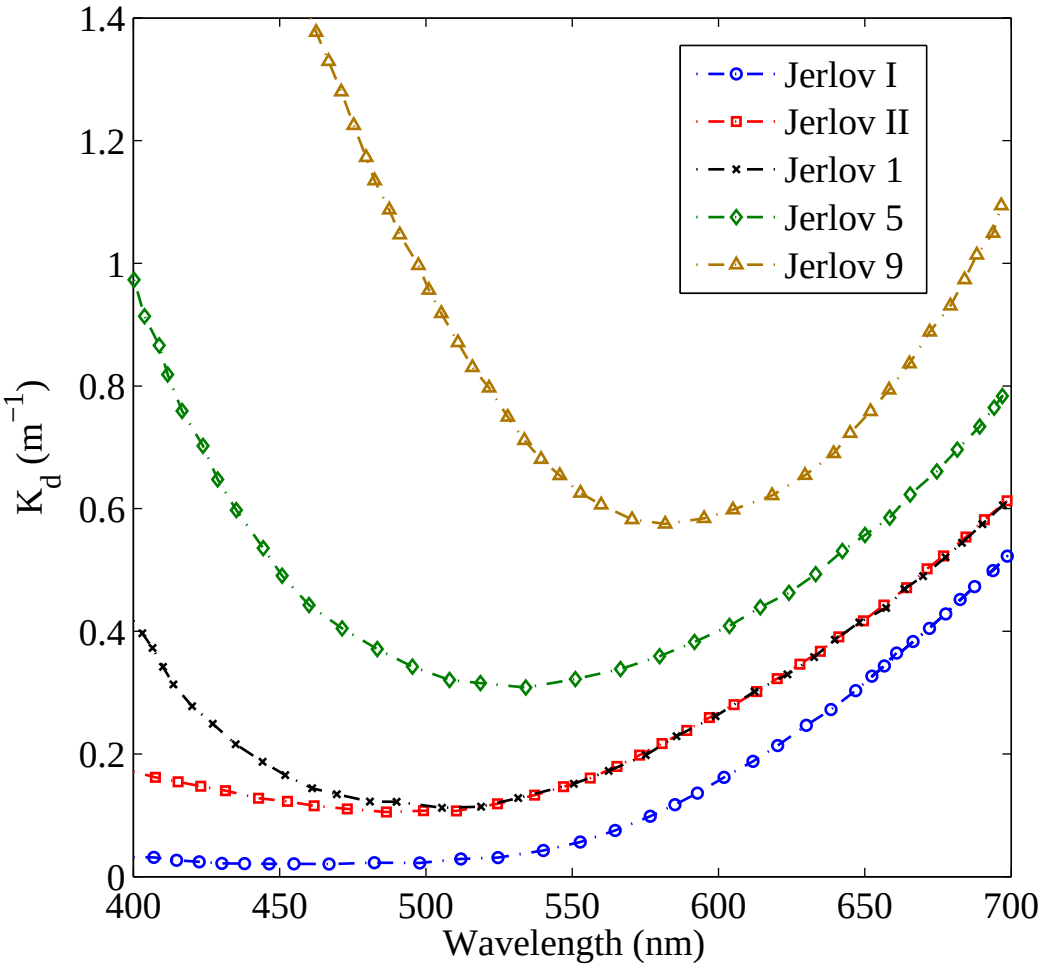

Figure 2.7: Mean values of the downward irradiance attenuation coefficient K_{d} for $D \leq 10\,\mathrm{m}$, for Jerlov water types I, II, 1, 5, and 9 [36].

this model, which is a non valid hypothesis in practice, see [36] for more details. Lastly, the expression of K_d in (2.10) is divided into two equations, with respect to a boundary of Chlorophyll concentration, and these equations lead to divergent values of K_d for $C_{cl} = 1\,mg/m^3$.
The next bio-optical model presented in the following overcomes these drawbacks.

2.3.2.3 Woźiniak's bio-optical water classification

This model is based on the statistical analysis of experimental data collected in different waters (lakes, seas, and oceans), having different C_{cl}. Although very similar to the Smith and Baker model, providing an analytic relationship between K_d and C_{cl} and adopting some of their hypotheses, like the values of K_w, the Woźiniak model provides a single expression of K_d as a function of C_{cl} . In addition, it takes into account the dependence of K_Δ and k_c on C_{cl}. We have:

$$K_d(\lambda) = K_w(\lambda) + C_{cl} \,.\, [C_1(\lambda) \,.\, \exp(-a_1(\lambda) \,.\, C_{cl}) + k_{c,n}(\lambda)] \tag{2.11}$$

where $C_1(\lambda)$ and $a_1(\lambda)$ are statistically derived parameters, whose values and the description of their computation procedure are presented in [36]. It has been reported in [36] that the analytic expression of K_d in (2.11) is coherent with some experimental measurements, for instance for $\lambda = 440\,nm$ with C_{cl} varying from 0.01 to $100\,mg/m^3$. An illustrative exemple of spectra of the downward irradiance attenuation coefficient K_d according to the Woźiniak's model, is presented in Fig. 2.8.

2.3.2.4 Other bio-optical models

There exist several other bio-optical classifications of water, based on statistical analyses, similar to the models proposed by Smith and Baker, and Woźniak. Among these, we can mention that of Austin and Petzold. This model allows the calculation of $K_d(\lambda)$ at all wavelengths from a value of $K_d(\lambda_0)$ measured for any given wavelength λ_0. This model is defined by a simple equation as follows:

$$K_d(\lambda) = \frac{M(\lambda)}{M(\lambda_0)}[K_d(\lambda_0) - K_w(\lambda_0)] + K_w(\lambda) \tag{2.12}$$

where K_w refers to the value of attenuation coefficient for pure sea water, and $M(\lambda)$ is a statistically derived coefficient. An exhhaustive table of values of K_w and $M(\lambda)$ can be found in [35]. This model is reported to be valid only for the case where $C_{cl} \leq 3\,mg/m^3$.
Another model is Morel's, also based on statistically derived variable. However, in contrast to the model of Austin and Petzold which determines K_d from measurements at one wavelength, Morel's model determines the value of K_d based on the actual Chlorophyll concentration. It is given by :

$$K_d(\lambda) = K_w(\lambda) + \chi(\lambda)\, C_{cl}^{e(\lambda)} \tag{2.13}$$

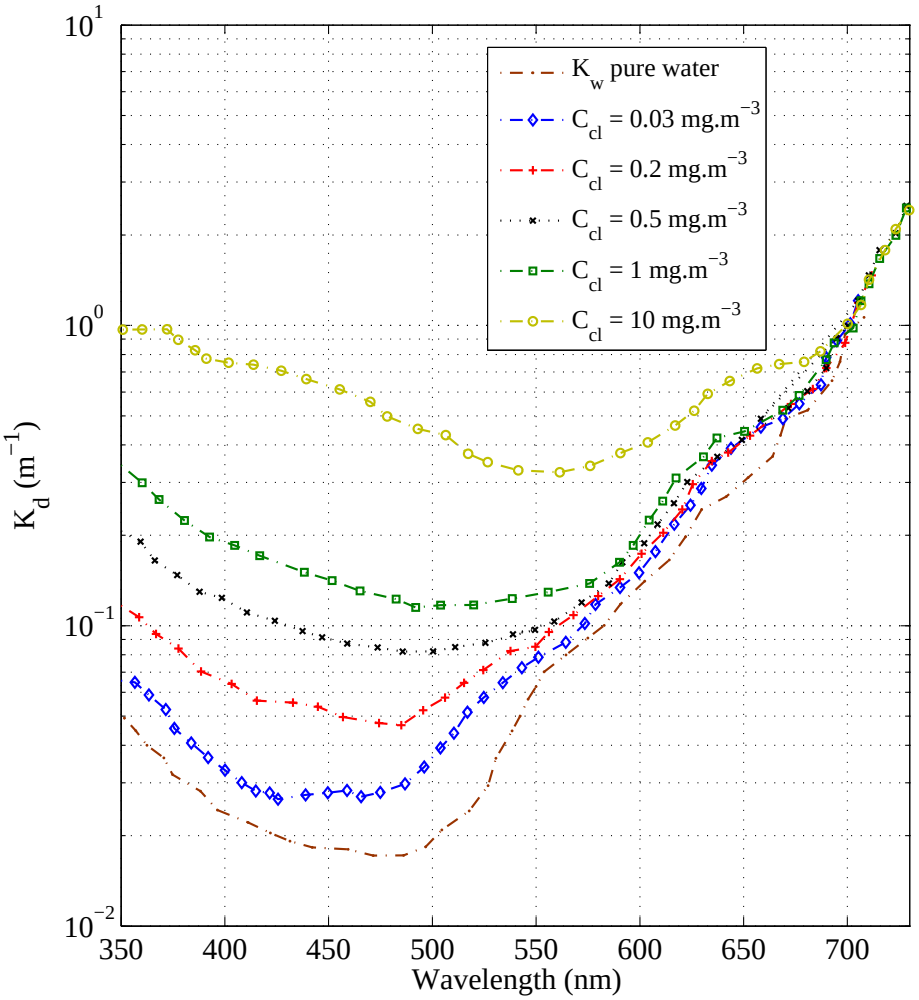

Figure 2.8: Spectra of the downward irradiance attenuation coefficient K_d according to the Woźniak's model, reproduced from [36].

Here, $\chi(\lambda)$ and $e(\lambda)$ are statistically derived functions that convert the Chlorophyll concentration C_{cl} in mg/m^3 into K_{d} in m^{-1}. This model is applicable only for Jerlov type 1 waters, which satisfies the condition $C_{\text{cl}} < 30\,\text{mg/m}^3$ [35]. The main weakness of this model is the high prediction error of K_{d}. The accuracy of Morel's model was examined in [35] where it was concluded that the gap between the predicted and the measured values of K_{d} can be on the order of a factor of two in Jerlov case 1 waters, and even larger for Jerlov case 2 waters.

2.3.2.5 Estimation of K_{d} in clear ocean waters

Our study is focused on UWOC within oceans and deep seas, which can be regarded as a Jerlov case 1 waters [40]. Thus, we can calculate the corresponding values of the diffuse attenuation coefficient K_{d}, with respect to the bio-optical models presented earlier, based on the Chlorophyll concentration. Hereafter, we will consider the typical Chlorophyll concentration of clean ocean waters $C_{\text{cl}} \approx 0.5\,\text{mg/m}^3$ [35, 40]. We will conduct our study in the bleu-green window of the visible spectrum, where the attenuation rates represented by K_{d} are relatively low. We will specifically consider two wavelengths $\lambda_1 = 532\,\text{nm}$ and $\lambda_2 = 470\,\text{nm}$, typically used in low turbidity waters. The estimation of the related values of K_{d} are presented it in Table 2.2. Giving that the obtained values are a bit different, and considering that the Woźniak's model is regarded to be more reliable than the other models, we will consider $K_{\text{d}} = 0.08\,\text{m}^{-1}$ for both wavelengths. In the following, in the aim of simplifying the notations, the diffuse attenuation coefficient will be denoted by K.

Table 2.2: Diffuse attenuation coefficient K_{d} in m^{-1}, calculated using the bio-optical models of water classification, $C_{\text{cl}} = 0.5\,\text{mg/m}^3$

	Jerlov	Smith & Baker	Woźniak	Morel
$K_{\mathbf{d}}(470\,\mathbf{nm})$	0.11	0.09	0.08	0.06
$K_{\mathbf{d}}(532\,\mathbf{nm})$	0.13	0.09	0.08	0.08

2.3.3 Optical power attenuation in water

The objective of this section is to describe the attenuation of light as a function of the distance it travels within the aquatic medium. The light underwater is subject to high attenuation due to the physical phenomena of absorption and scattering, which depend on water properties such as its degree of turbidity. They further depend on the light beam properties. In effect, depending on the optical source type, the light beam can be either collimated, which is the case for a laser diode for instance, or diffuse, which is the case of a LED with a radiation pattern approximated by the Lambertian model [41]. This two classes of light patterns suffer from distinct attenuation effects, as we will show in the following.

Several studies has been conducted to model the optical power loss within the aquatic channel. There exist several experimental works, where the solar irrandiance distribution underwater has been measured for various water types [30, 42]. In the context of UWOC, the related findings are useful for instance for the computation of ambient solar-induced background noise, as we will show in Chapter 3. Furthermore, the attenuation of a quasi-monochromatic optical signal, used for communication, is a key issue in this context.

2.3.3.1 Collimated beam attenuation

When considering a collimated beam, such as a laser beam, the intensity loss within the aquatic channel is often modeled by BL law as follows [16, 43, 26]:

$$E(Z,\lambda) = E(0,\lambda)\ \exp(-c\,Z) \tag{2.14}$$

where $E(Z)$ is the light intensity at a distance Z from the Tx and $E(0)$ is the emitted intensity. The attenuation coefficient c in units of m^{-1} is wavelength dependent and is equal to $a+b$, with a being the absorption and b the scattering coefficients, respectively (see Subsection 2.3.1). This parameter describes the effect of absorption and single scattering of photons.
As explained is Subsection 2.3.1, the BL law assumes than any photon subject to scattering (single or multiple scattering), is regarded as lost, i.e. it does not reach the Rx. This approximation is not always valid in practice, first because single scattered photons may still be captured by a Rx with an adequate aperture and second because a part of multiple scattered photons can reintegrate the light direction and be received within the Rx field of view (FOV) [43]. For the case of clear ocean waters where the absorption is predominant and the scattering events are less likely to happen, the BL law has been proven to be a good approximation of the channel loss [40]. However, as the water turbidity increases and thus the probability of multiple scattering, the BL law loses its accuracy [43]. For these reasons, several theoretical studies have used numerical simulations mainly based on Monte Carlo method for calculating the received power [16, 43, 44, 45]. Thereby, all parameters related to the Rx and the Tx, as well as the water optical properties can be precisely taken into account, and power loss estimation can be performed accurately.
Anathor analytic formulation of power loss is presented in [46] that combines the power loss by BL law and the loss due to spherical wave propagation. Also, a two-term exponential model for channel loss was provided in [44] for long distance communications and it was validated with MC simulations.
In all above mentioned works, optical power loss calculation has been based on the beam attenuation coefficient c, which is relevent for the case of a single narrow collimated beam [35]. However, this parameter cannot be used to describe the power loss of a diffuse or uncollimated beam. For such cases, the diffuse attenuation coefficient K is a more appropriate factor to describe power attenuation. Indeed, K describes by definition the power decrease versus Z of a diffuse uncollimated beam, consisting of photons propagating in all directions [35].

2.3.3.2 Diffuse light attenuation

When a diffuse light penetrates in water (e.g. solar radiations), it becomes increasingly diffuse and attenuates exponentially with depth. This prediction is consistent with the profiles of underwater solar irradiance attenuation versus depth presented in [30]. The optical power decay is then characterized by the diffuse attenuation coefficient K as follows [35, 26]:

$$E(\lambda, D) = E(\lambda, D_0)\ \exp\big(-K\,D\big), \tag{2.15}$$

where $E(\lambda, D_0)$ denotes the light irradiance at a depth equal to D_0, and D the vertical distance travelled by light. Equation (2.15) is essentially employed to compute the attenuation of sunlight in water [26]. Likewise, it can be employed for the case of an LED-based optical source, which is regarded as a diffuse light source. Considering (2.15), two important remarks should be taken into account:

Note 1: It implicitly assumes that K is independent of D. This assumption is rational for the case of homogeneous waters [35, 47]. In practice, K does depend on D and its variations have to be taken into account. This is due to the variation of the Chlorophyll concentration versus depth [37]. Thus, it is more convenient to write the expression of E as follows [39] (where λ was removed for simplicity):

$$E(D) = E(0)\ \exp\Big(-\int_0^D K(x)\,\mathrm{d}x\Big), \tag{2.16}$$

It has been reported that far from bottom and surface, K converges to an asymptotic value, denoted by K_∞. For instance for depths higher than $\sim 60\,\mathrm{m}$, according to the experimental depth profiles of K presented in [30], and $\sim$20 m as reported in [39]. The precise mathematical modelling of K is out of the scope of this work. That is why, for the sake of simplicity, we assume that K is almost constant for the considered depths, and take its pessimistic (highest) corresponding value K_∞. An illustative example of the variation of K versus depth is presented in Fig. 2.9 [39].

Note 2: One should keep in mind that(2.15) is applicable only to a case of a vertical communication link. This is due to the fact that, by definition, K is defined in terms of attenuation of a downward irradiance. Still, for a different link configuration, for instance a horizontal link, we can keep referring to (2.15) to describe the optical power loss. Indeed, there exist several K functions which describe the attenuation of light beam, depending on its propagation direction with respect to the zenith axis. Although semantically different (i.e. referring to completely different processes), all K factors are often equal and converge ultimately (for high depths within homogeneous waters) to the same constant value K_∞ [35].

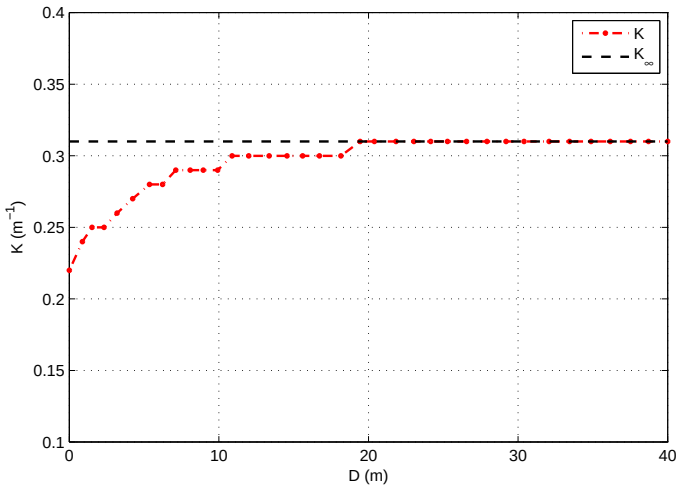

Figure 2.9: Computed downward diffuse attenuation coefficient K for highly scattering water, with $a = 0.2\,\mathrm{m}^{-1}$ and $b = 0.8\,\mathrm{m}^{-1}$, where the sun is at the zenith.

2.3.4 Channel impulse response

In addition to attenuation, an optical signal underwater may suffer from intersymbol interference (ISI), a direct consequence of pulse stretching caused by scattering (see Subsection 2.3.1.2). This leads eventually to the degradation of the communication link performance, particularly for the case of relatively high data transmission rates and over long distances [18, 48]. It would be necessarily to employ signal processing techniques at the Rx (i.e. channel equalization) in order to reduce the ISI effect. For these reasons, a careful characterization of the impulse response of the underwater channel and the quantification of the related time dispersion are among the key aspects in the design of a reliable UWOC link.
Several works investigated the time dispersion introduced by the UWOC channel and the resulting ISI. For instance in [48], a study of time dispersion versus the communication link span and the data rate was conducted for a polarized light. The author concluded that ISI strongly deteriorates the transmission quality as data rate increases (around Gbps), for the case of relatively long range links ($\sim 50\,\mathrm{m}$). On the other hand, Hanson *et al.* reported an error-free underwater optical transmission at 1 Gbps over a 2 m path within a laboratory water pipe. Measurements were conducted for several degrees of turbidity of water, and took into account different system parameters such as the Tx beam divergence and the Rx aperture size. The authors reported the absence of noticeable channel time dispersion due to multiple scattering.
In [16], the authors presented a realistic model for an underwater wireless optical channel using an elaborate Monte Carlo simulator which took into account different parameters including the water type and the Tx / Rx characteristics. Their study confirmed that except in highly turbid waters, the channel delay spread is negligible

when working over moderate distances (up to 50 m in clear waters). As a result, in most practical cases, the channel can effectively be considered as frequency non-selective and the signal does not suffer form any ISI at the Rx.
In [49], the authors carried out a series of experiments using a method allowing high sensitivity and high dynamic range measurement of the underwater channel frequency response, for different water turbidities. Measuring both spatial and temporal signal dispersion, they confirmed that in clear waters there is little or no temporal dispersion, while as turbidity increases, the optical signal suffers more from delay spread.

2.4 Design of UWOC system

A synoptic diagram of a typical UWOC link is presented in Fig. 2.10. It can be decomposed into three main parts: the Tx, the propagation underwater channel, and the Rx. The Tx consists in a data source that contains the bit streams to be transmitted. These latter are modulated and probably encoded, then converted to an optical signal by an optical source. After being optionally focused by some optics towards the Rx, and probably steered by a dedicated unit, the optical signal propagates through the aquatic channel. Optics could be employed at the Rx side to focus the received signal on the light collecting area of the photo-detector. As a matter of fact, inserting a lens in front of the photo-detector (which has typically a very small active area) has the advantage of increasing the received optical intensity. The PD converts the received light to an electrical current which passes then through a dedicated electronics, which typically consists in a trans-impedance (TZ) circuit (which converts current to voltage), a low-pass filter (LPF) (to limit the Rx noise level), and a sampling unit. Lastly, signal demodulation and decoding are conducted so as to retrieve the originally transmitted binary data.
In this section, we explain the different parts of an UWOC system described above and review the existing optical source and photo-detection technologies commonly employed in sub-sea optical communication. We also present the modulation schemes and the error correcting codes often employed in this context.

2.4.1 Transmitter

The main strength of optical communications underwater is the fact that they employ a mature and reliable existing technology, already used in optical fiber and FSO communications. Yet, UWOCs have specific and strict requirements, such as compactness, high energy efficiency, and a limited wavelength range mainly within the blue/green portion of the visible spectrum. For instance, even with a high Tx power level, UWOC link spans are limited to about 200 m at most, due to high attenuation of light beam in water. The typical transmitted power levels used in these systems range between several hundreds of mW to several Watts[10, 3].
The most popular choices for the optical source are LEDs and semi-conductor laser diodes (LDs). Solid-state lasers are rather forsaken; although providing interest-

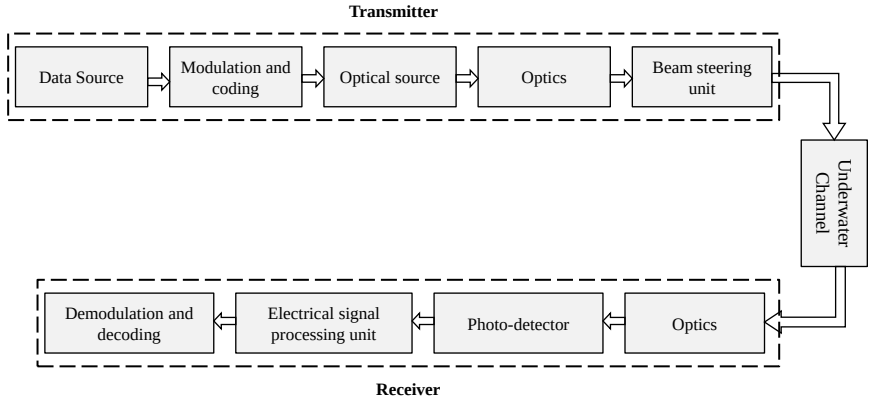

Figure 2.10: A synoptic diagram of a typical UWOC system, reproduced from [10].

ing power density and highly focused beam performance, they are more difficult to modulate at high frequencies and add complexity, volume, power-consumption and cost to the underwater optical communication system.
The LED and LD-based optical source technologies are reviewed hereafter, and a comparison of their characteristics and main key performance along to those of standard lasers are provided in Table. 2.3.

2.4.1.1 Laser diodes

An LD, also known as injection LD, is an electrically pumped semiconductor laser, with an active medium formed by a p-n junction of a semiconductor diode similar to that found in an LED. Commercially available direct-to-green (as opposed to infrared frequency-doubled laser) LD makes this technology a good candidate for UWOCs, offering several advantages including electrical efficiency and compact packaging.
LDs are the most common laser source in use today, employed in a number of UWOC test beds. For instance, in [18], Hanson *et al.* employed a LD-based Tx emitting at $\lambda = 532\,\text{nm}$ to establish an a high speed (up to 1 Gbps) link over a 2 m laboratory water tank. In [50], Cox reported a high data rate transmission, up to 400 Mbps, employing a 405 nm blue LD. In [51], Oubei *el al.* experimentally demonstrated a 2.3 Gbps UWOC link over 7 m using an LD with 1.2 GHz bandwidth and emitting at 520 nm. Another experimental work presented in [52], demonstrated a high speed 1.45 Gbps UWOC transmission employing a 405 nm LD, over 4.8 m distance. Lastly, in [53], Shein *et al.* presented a power efficient and compact UWOC system employing a 450-nm LD and reported a data rate of up to 2 Gbps over a 12 m, and 1.5 Gbps over a 20 m.
Over the past decade, the development of new materials have allowed the fabrication of LDs with improved performance, i.e., long lifetime, high efficiency up to 50%, high beam quality with highly focused light, and narrow spectral bandwidth (less

than 1 nm [3]). However, ond main weakness of LDs is the sensitivity of their spectral characteristics (such as mode spectrum, wavelength) to temperature, requiring hence a tight stabilisation of the operation temperature. Also, the Rx optical filter should accommodate any shift in the laser wavelength caused by temperature variation [3]. Another disadvantage of LDs, is their higher price compared to LED counterparts (typically by a factor of ten) [54].

2.4.1.2 LEDs

LEDs are semiconductor devices that emit light via the recombination of electrons and holes within the p-n junction when forward biased. Blue/green LEDs represent a popular light source technology in UWOC systems and have been employed so far in numerous in lab test beds [46, 55, 56] and prototypes, e.g. the AquaOptical modem developed by MIT researchers [57, 58].
LEDs offer several advantages such as good electrical-to-optical efficiency (around 10% [3]), emitting wavelengths ranging from 470 to 940 nm [59], supporting relatively high switching speeds up to 10 Mhz (e.g. the blue NICHIA NSPB510AS LED model[60]), low cost, compactness, less temperature dependency than typical LDs [10], and long operating lifetimes [61].
Due to their relatively large beam width, LED-based UWOC system are less concerned by link misalignment than the LD-based counterpart [62], although this comes at the price of higher geometric power loss at the Rx. Nevertheless, the beam divergence can be controlled by means of dedicated focusing optics [63] or array of LEDs [58].
Another impediment of LED transmitters is their relatively wide spectral bandwidth, on the order of $30 - 50$ nm full-width at half maximum (FWHM) [59]. This impacts directly the spectral width of the corresponding Rx optical filter, which can in turn lead to problems with sunlight rejection at relatively shallow depths (see Chapter 3).

2.4.2 Receiver

Given the typically high attenuation of the aquatic channel, UWOC receivers are expected to have high sensitivity in order to allow transmission over long enough distances. It also implies the need for large FOV receivers in order to capture the maximum of the beam intensity at a given distance. Obviously, a high photo-detection efficiency and gain, and a low Rx noise level are also among critical considerations. The choice of the photo-detector used at the Rx is thus of special importance. In the blue/green spectral range, the PD choices include:

- PIN photo-diodes, which are capable of fast response times but have no internal gain
- Avalanche photo-diodes (APDs), which provide an internal gains on the order of 100

Table 2.3: Comparison of the different light source technologies

Parameter	LED	Laser Diode	Solid State Laser
Modulation speed	100-300 MHz	More than 1 GHz	more than 1 GHz
Power	∼mW	∼hundreds of mW	from 10 W to 1 KW
Spectral bandwidth FWHM	$30-50$ nm[59]	<1 nm	<1 nm
Light source	Incoherent	Coherent	Coherent
Minimum output beam divergence	$\sim 0.5°$ (Wide)	$\sim 0.01°$ (Narrow)	$\sim 0.01°$ (Narrow)
Lifetime	Long	Medium	Medium
Temperature dependence	No	High; Needs temperature stabilization	High; Needs temperature stabilization
Driver electronics	Simple modulating current source	Simple modulated current source; Needs threshold and temperature compensation circuit	External optical modulator
Cost	Low; off-the-shelf optics and electronics	High; special high-grade optics and compensating electronics	High; special high-grade optics and compensating electronics
Electrical-to-optical conversion efficiency	∼10% [3]	∼50% [64]	from 0.1% to few percent [3]

- Photo-multiplier tubes (PMTs), which are vacuum tubes encompassing a photo-emissive surface (the photo-cathode) followed by an electron-multiplying structure, and have extremely high sensitivity and ultra-fast response.
- SiPMs built from APD arrays, with high sensitivity and relatively low operating voltage.

We provide a brief description of these four PD types in the following.

2.4.2.1 PIN photo-diode

A PIN photo-diode consists of a lightly doped intrinsic semiconductor region between two highly doped transparent P-type and N-type contact layers [65]. Silicon-based PINs are adapted to UWOCs as they have a good sensitivity at wavelengths ranging

from 300 to 1100 nm, work with low bias voltage on the order of 2-5 V, and feature a relatively low capacitance, resulting in a wide bandwidth, i.e., fast components. Furthermore, PINs are low cost and tolerate well exposure to ambient light.
The use of PIN photo-diodes for an UWOC modem was investigated in [57], where it was concluded that PINs are suitable for short to moderate range transmissions.

2.4.2.2 APDs

APDs are employed in a variety of applications such as long-range fiber-optic and FSO systems, positron emission tomography, particle physics, etc. They have the same semi-conductor structure as PIN photo-diodes but offer additional advantages such as a high internal gain (typically around 100), potentially faster response, and a higher quatum efficiency (defined as the probability that a detected photon generates an electron-hole pair) on the order of 70 - 90% [10]. However, APDs require high bias voltages and complex control circuitry, and they are more sensitive to ambient noise.
in the context of UWOC context, APDs have been considered in a few works. For instance, in [66], Cossu *et al.* reported 1 Gbps transmission over 2 m long path while employing an APD-based Rx. In [57], an APD was integrated within an optical modem prototype which was reported to attain an error-free communication at 4 Mbps over 2 m link distance.

2.4.2.3 PMT

A typical PMT consists of a photo-emissive cathode (photocathode) followed by focusing electrodes, an electron multiplier and an electron collector (anode) in a vacuum tube. When light enters the photocathode, it emits photoelectrons into the vacuum. These photoelectrons are then directed by the focusing electrode voltages towards the electron multipliers, also called dynodes, where electrons are multiplied by the process of secondary emission. The multiplied electrons are collected by the anode as an output signal.
Because of secondary-emission multiplication, PMTs provide extremely high sensitivity and exceptionally low noise among the photosensitive devices currently used to detect a radiant energy in the ultraviolet, visible, and near infrared regions. In addition to providing high internal gain in the order of 10^6 to 10^7, PMTs also feature a fast time response and a large photosensitive area [3]. However, they require a high operation voltage, and are more expensive, bulky, and easily damaged by exposure to ambient light.
PMTs have been employed in a fex recent UWOC test beds such as [18, 49, 56] as well as in the commercialized BlueComm modem [67].

2.4.2.4 SiPM

SiPMs also called SPMs or MPPCs for multi-pixel photon counters in the literature, are Silicon single photon sensitive devices built from APD array on a common

substrate. The idea behind this device is the detection of single photon events in sequentially connected APDs. The dimension of each single APD can vary from 20 to 100 nm, and their density can be up to 1000 per square millimetre. Every APD in an SiPM operates in the Geiger-mode and is coupled with other APDs by a polysilicon quenching resistor. Although the device works in digital/switching mode, the SiPM is an analogue device because all the microcells are read in parallel making it possible to generate signals within a large dynamic range for just a single square millimetre area device. The supply voltage (V_b) depends on the APD technology used, and typically varies between 25 and 70 V, thus 30 to 50 times lower than the voltage required for a typical PMT.
The main features of a SiPM are:

- a total quantum efficiency of about 20%, close to that of a traditional PMT
- A high internal gain of around 10^6 and a high sensitivity, comparable to these of a PMT.
- Insensitivity to external magnetic fields, in contrary to vacuum PMTs
- Small dimensions resulting in extreme compactness, low weight, and mechanical robustness.

We will present a detailed description and performance study of SiPMs, along with a comparison of their performance with those of PMTs and APDs in Chapter 4.

2.4.3 Signal modulation

The modulation scheme can affect considerably the performance of an UWOC system. Like in FSO or indoor visible light communication (VLC) systems, the most commonly used transmission schemes are based on intensity modulation and direct detection (IM/DD), where the simplest one is on-off keying (OOK) being interesting due to its implementation simplicity. In [68], Gabriel *et al.* compared the performances of several IM/DD schemes focusing on energy and bandwidth efficiency, as well as on practical implementation issues. They concluded that, although pulse position modulation (PPM) is optimal in the sense of energy efficiency, digital pulse interval modulation (DPIM) [69] would make a good compromise between link performance and complexity. Indeed, DPIM outperforms OOK in terms of BER for a given received signal-to-noise ratio (SNR), in particular for large number of bits per symbol [68] and it has a better bandwidth efficiency and optical peak-to-average power ratio (PAPR) compared to PPM. As another choice, sub-carrier intensity modulation (SIM) [70] can be employed where the classical RF modulation schemes (PSK or QAM) can be used by adding a DC level to the modulated signal before intensity modulation in order to preserve the phase information. The interest of the SIM schemes is the higher spectral efficiency that they can offer but at the expense of reduced energy efficiency due to the DC bias used to avoid negative amplitudes. On the other hand, in order to deal with the limited bandwidth of the optical components, an efficient approach is to use discrete multi-tone (DMT) modulation with

the further possibility of bit-loading. An experimental verification of the feasibility of such modulation schemes was presented in [71, 66].

2.4.4 Error correction coding

Given the highly attenuating propagation medium, to deal with low SNR at the Rx, a classical solution is to employ channel coding techniques. As a matter of fact, the most important noise sources are the thermal noise and the shot (quantum) noise in the case of using a PIN photo-diode or an APD, respectively [72]. Background radiations are practically negligible except in relatively shallow waters. In this context, forward error coding (FEC), a well known technique commonly used in communications to detect and correct errors, has been considered in several works such as [73, 74]. However, the main drawback of this technique is the fact that it increases the payload of the transmission. Furthermore, although simple and classical block codes such as Reed-Solomon (RS) codes can be used, better performance is obtained by using powerful channel coding techniques such as low-density parity-check (LDPC) codes and turbo-codes. These latter schemes require computationally complex decoders and are likely suitable for ∼Mbps data-rates typically, so that the real-time implementation of the Rx is feasible or when data detection is done off-line. For instance, the performance of RS, LDPC, and turbo-codes were compared in [74] using an experimental set-up where the superiority of LDPC codes was demonstrated. A better link reliability can be obtained through the use of appropriate coding at the data-link layer, in addition to the classical error correction coding at the physical layer. For instance, in AquaOptical II modem, an RS inner code is used together with a Luby transform (LT) outer code [46].

2.5 Other practical challenges

Apart from absorption and scattering, the transmission of the communication optical signal underwater faces various challenges, which can reveal to be very perilous to the link reliability and performance. Among these, we point out in the following subsection the effect of link of misalignment, channel turbulence, beam obstruction, and the presence of other light sources underwater.

2.5.1 Impact of link misalignment

In a typical UWOC system, angle scattering is highly peaked in the forward direction. Therefore, the optical beam has a high directivity, which turns out to be problematic from the point of view of system implementation. In fact, link misalignment is unavoidable in underwater systems, especially when communicating with an AUV. In fact, due to stringent constraints on energy consumption, precise localization and tracking mechanisms may not be feasible to employ. Misalignment errors can seriously impact the performance and reliability of the communication link. This is specially the case for small FOVs receivers. As explained in Section 2.4,

inserting a lens in front of the PD increases the received optical intensity, but also limits the Rx FOV and, hence, increases the sensitivity to link misalignment [75]. This problem is slightly alleviated in high turbidity waters where we can paradoxically benefit from beam spatial dispersion which helps reduce the sensitivity to link misalignments [49]. An efficient solution may be to use an array of LEDs at the Tx and/or an array of photo-diodes at the Rx. For instance, compact arrays of seven LEDs and seven PDs in the form of truncated hexagonal pyramid structures were used in [76] to achieve quasi-omnidirectional patterns. This allows a large overall Rx FOV and substantial Tx-Rx alignment simplification in practice. The further advantage of such arrays is that we can estimate the angle of arrival of the optical signal at the Rx in order to correct the Rx position/direction or to perform beam steering at the Tx electronically toward the best direction in order to optimize the energy consumption.

2.5.2 Turbulence

Turbulence is observed when water layers experience rapid changes in their refractive index. It results from changes in the salinity, pressure and temperature of the water, but also from ocean currents or underwater vehicles. Inhomogeneities and variations of the refractive index along the transmission path causes fluctuations in both intensity and phase of the received signal. This is also referred to as scintillation or fading, and can seriously affect the link reliability and performance.
The effect of signal fading caused by turbulence has been ignored in most previous works on UWOC, although a few recent works have considered the characterization of underwater turbulence in general. For instance, in [77, 78, 79], a study of underwater optical turbulence versus depth was carried out for investigating its impact on underwater imaging and the use of adaptive optics was discussed in [80] to overcome image degradation caused by turbulence. Furthermore, in [81], the authors presented an UWOC channel model which took into consideration the underwater turbulence. They proposed to employ a spatial diversity Rx in order to mitigate channel fading. It is shown in [82] that whereas temperature fluctuations have the major impact on turbulence in relatively shallow waters, salinity variations dominate as the water depth increases.
In [83], an analytical study of the performance of MIMO based UWOC systems was presented. The authors consider exploiting spatial diversity over UWOC links in the objective of mitigating signal fading induced by turbulence. The impact of this latter on the performance of a 25 m communication link within coastal waters was investigated, for the case of a data rate equal to 0.5 and 50 Gbps. It has been concluded that spatial diversity can improve the system performance (in terms of maximum achievable error-free link span), and partially mitigates the signal fading, especially for low data rates.

2.5.3 Beam obstruction

Maintaining a line-of-sight (LOS) between the Tx and the Rx is important for an UWOC link. In the underwater scenario, the probability of beam obstruction is higher, as compared to terrestrial FSO links, for example, and can be caused by any living organism such as schools of fish or marine animals that can potentially block the light beam. Obstruction by algae growth is another possibility for underwater systems that are more permanent in nature. Increased light availability causes more algae growth at the Tx lens of the communication system which will need an anti-algal coating or a regular cleaning.
Managing probable temporal link blockage necessitates the use of channel enforcing techniques such as automatic repeat request (ARQ), as investigated in [84] for the case of underwater sensor network. A more efficient approach is to combine ARQ with error correction coding, i.e. using hybrid ARQ [10].

2.5.4 Background optical noise

Another possible factor that can impact the UWOC link performance is the existence of other light sources than that employed for communication. For instance, deep sea fish and other marine life have bio-luminescence that occurs naturally when energy is released by a chemical reaction in the form of light. Typically bioluminescent transmission is in the blue region, of wavelength 450-550 nm, although there are a few cases of far red emissions. Another light source in the ocean is fluorescence by phytoplankton. This is the re-emittance of absorbed light at another wavelength, typically longer, and is observed mainly in zones where phytoplankton grows. Chlorophyll is the most significant pigment which causes fluorescence in phytoplankton, which is result of photosynthesis.
The main part of the background noise is likely caused by solar radiations underwater for relatively shallow depths. This will be discussed in details in Chapter 3 where we will show that sunlight can severally degrade the link performance for such low operation depths. Another parasitic light source which may have an important impact on UWOC link performance is underwater vehicles lighting. The precise modeling and quantification of the effect of this noise is out of the scope of this thesis, yet it would be an interesting point for future studies.

2.6 Existing systems and prototypes

A few UWOC units of limited application have been commercialized recently. For instance, Ambalux [85] has introduced a commercial UWOC system with a maximum data rate of 20 Mbps over ranges up to 40 m. Also, Sonardyne [67] has commercialized the BlueComm UWOC system which can operate over distances of up to 200 m with a maximum rate of 20 Mbps. On the other hand, several experimental set-ups or UWOC system prototypes have been realized during the past few years in order to characterize the underwater optical channel, to study the impact of special

modulation/coding schemes, or to investigate practical limitations and implementation difficulties of such links. Besides the aforementioned works in the previous subsections (e.g. [75, 71, 74, 86]), we provide hereafter a brief summary of the experimental results reported recently. This presentation is in no way exhaustive; we aim to provide a description of the most recent works that concern different applications or approaches. Among the first realized prototypes is the AquaOptical modem designed by MIT researchers. Its early version was capable of supporting a few Mbps transmission rate over a distance of a few meters [57]. An improved version, named AquaOptical II allows higher transmission ranges with higher data rates [58]. Recently, in [46], the authors proposed an end-to-end model for the transmission link, including light sources, the aquatic channel, optoelectronic circuitry, and optics of Tx and Rx, that they validated using the AquaOptical II modem.
One of the first successful laboratory experiments for high-rate UWOC was that presented in [18] where up to 1 Gbps data rate was achieved over a distance of two meters using a relatively high transmission optical power. The set-up was then used to study the channel frequency response. Since then, several laboratory set-ups have been designed to study different aspects of UWOC. In [87] the authors investigated the interest of spatial diversity in a turbulent medium by using a two-Tx two-Rx system, where a beam splitter was used to generate two parallel optical beams. Creating water turbulence by the injection of bubbles, they have shown that such a diversity system allows to reduce the fading-induced errors by a factor of ten. On the other hand, it was proposed in [76] to estimate the water quality at the Tx side from the backscattered light collected by a co-located Rx. The Tx can in this way adapt its power or transmission scheme to changing water conditions. The authors also proposed to use smart Tx-Rx by employing arrays of LEDs/PDs. Furthermore, the description of an optical telemetry system was presented in [63] where a 5 Mbps link was implemented at a range of 80 m, in particular. Lastly, using a laboratory set-up, the interest of DMT modulation to circumvent bandwidth limitation of optoelectronic components was investigated in [66].

2.7 Conclusion

In this chapter, we presented a review of the state-of-the-art related to UWOCs. We reviewed the fundamental issues related to the propagation medium and the main Tx and Rx components employed in this context, and presented the most relevant reported works.

Hereafter, we will present our research scope, and the main results and contribution of our work. The main assumptions that we will consider in the following chapters can be summarized as follows:

- Transmitter
  - monochromatic LED-based light beam

  - Intensity modulation
  - No error correcting/coding

- Channel
  - No signal fading due to channel turbulence
  - No signal obstruction
  - Perfect alignment of the Tx and the Rx

- Receiver
  - Direct detection
  - Perfect time synchronization with the Tx
  - Perfect channel knowledge at the Rx (for signal demodulation, if necessary)

Chapter 3

Solar Background noise study

Contents

3.1 Introduction

In this chapter, we focus on the effect of the background noise generated by solar radiations on the communication link performance. Although the solar noise is often assumed negligible underwater, this assumption is rational only when working in very deep waters, where the underwater channel can effectively be considered as dark [3]. To the best of our knowledge, the accuracy of this assumption has not been examined so far for the case of relatively low depths, typically less than a few hundreds of meters. Due to high water transparency in the case of clear ocean waters, the blue-green wavelengths of sunlight can deeply penetrate in water and can be detected using sensitive detectors even at depths larger than 600 m [30].

We present an analytical generic model of the solar noise and study its impact on the UWOC link performance in terms of BER. Our study considers three different PD types, i.e., PIN, avalanche photo-diode (APD), and photo-multiplier tube (PMT), in order to highlight the practical limitations of establishing an UWOC link for each case. Meanwhile, we take into account the characteristics of the other link components, such as the emitting source radiation pattern and power spectrum at the Tx, the optical filter at the Rx, as well as the Rx FOV and aperture size. We show that solar noise can strongly limit the BER performance of the UWOC link for relatively low depths, around several hundreds of meters for the case of a PMT or several tens of meters for a PIN PD.
In the numerical results that we will present, we consider some special assumptions on the properties of the solar radiations, link configuration, and water turbidity. Nevertheless, the main results that we present are quite insightful for the design of UWOC links that are likely to be established at relatively low depths.

The remainder of the chapter is organized as follows. In Section 3.2, we present some previous works that have considered background noise modeling and its impact on the performance of UWOC links. Then in Section 3.3, we present the UWOC system description including channel model and the Rx electrical noise for the three PD types. Next, the details on background solar noise modeling are provided in Section 3.4. Then, in Section 3.5, we present some numerical results to evaluate the impact of solar noise on the UWOC link performance. Lastly, Section 3.6 concludes this chapter.

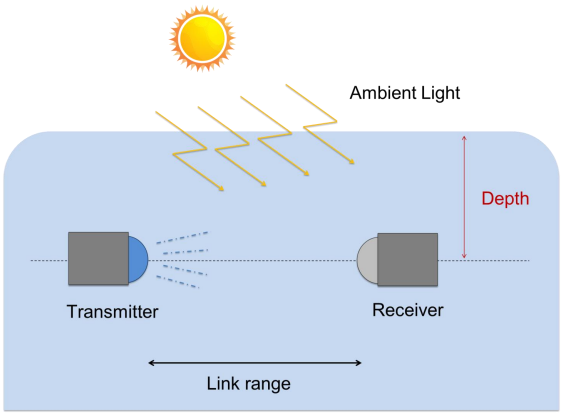

Figure 3.1: Schematic illustration of UWOC system operating under ambient solar radiations.

3.2 Literature review

The effect of solar noise in the context of UWOCs has been neglected in most previous works in the literature. Nevertheless, a few works have initiated studying

the impact of the background noise on an UWOC link. For instance, in [26], the authors presented some general considerations for the design of UWOC system and enumerated the different noise sources affecting the receiver. They considered *inter alia* the effect of background noise generated by ambient light on the system performance and provided the expression of the resulting shot noise as a function of solar radiance L_{sol} in $(\text{W m}^{-2}\,\text{sr}^{-1}\,\text{nm}^{-1})$. This last is given by:

$$L_{\text{sol}}(D,\lambda) = \frac{1}{\pi}\, E_{\text{d}}\, R_{\text{d}}\, L_{\text{fac}}\, \exp(-K_{\text{d}}\, D), \tag{3.1}$$

where E_{d} is the downwelling irradiance in $(\text{W m}^{-2}\,\text{nm}^{-1})$, R_{d} is the underwater reflectance of the downwelling irradiance, K_{d} is the diffuse attenuation coefficient, and D is the Rx depth. Also, L_{fac} describes the ratio of radiance observed at a specific viewing angle compared to that when looking straight down, and depends on the depth D and the wavelength λ. According to this equation, the calculation of L_{sol} depends on several factors for which exhaustive measurements are not available, to the best of our knowledge. For instance, for the specific case of $\lambda = 532\,\text{nm}$ and $D = 30\,\text{m}$, Reference [26] reports that L_{fac} ranges from 1 for a viewing angle equal to 180° (with respect to the zenith axis), 2.9 at 90°, and 333 at 0° (vertically-oriented link toward the sea surface). However, we did not find further measurements for variable operation depths, and/or viewing angles in the literature.

In [42] and [88], Tyler and Mobley presented the measured solar radiance distribution underwater but unfortunately their data were limited to relatively low depths, i.e., smaller than 60 m. On the other hand, presenting a preliminary study, Lacovara reported in [3] that background noise would generally limit the communication range by almost 20 m, without specifying the receiver opto-electronic components, e.g. the PD type nor the transmission conditions. Lastly, in [66], Cossu *et al.* carried out an experimentation under summer sunlight illumination and achieved a 'potentially error-free' UWOC transmission up to 58 Mbps over a 2.5 m range. However, although data acquisition was undertaken in the presence of sunlight, the resulting noise effect on the link performance was not identified precisely.

3.3 Main assumptions and system model

Let us consider a point-to-point communication link represented in Fig. 3.2. The Tx is assumed to use an LED. At the Rx, after photo-detection and trans-impedance amplification, the signal is low-pass filtered to limit the Rx noise, and then time-sampled prior to data detection to retrieve the transmitted bits. We consider three types of PDs, i.e., PIN, APD, and PMT. We will later extend this study to the case of SiPMs in Subsection 4.4.3. As previously explained in Section 2.4.2, whereas PIN PD is the 'classical choice,' APDs are interesting due to their inherent gain and have been considered in several previous experimental and theoretical works, e.g. [49, 46, 66]. PMTs, on the other hand, are low noise and have high sensitivity and gain, typically with a high bandwidth and a relatively large aperture, compared to semiconductor counterparts. They have also been considered in several works such

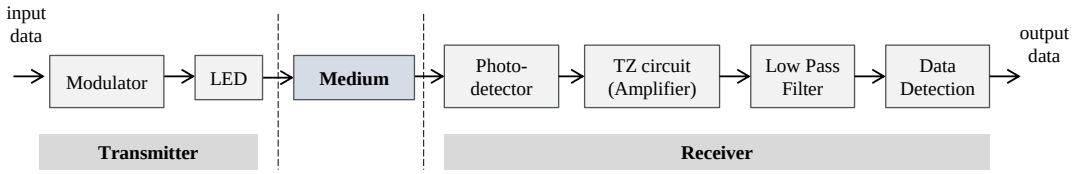

Figure 3.2: End-to-end general block diagram of UWOC communication link.

as [18, 49, 56]. Meanwhile, they are larger and more expensive, require high voltage for operation, are more easily damaged from exposure to high-intensity light, and have a limited dynamic range [3]. Note that our aim here is not to compare the relevance of using one PD type or another, but rather to focus on the impact that the solar background noise can have on the link performance when these components are used at the Rx, and the general trend of the dependency of the link performance on the Rx operation depth.

3.3.1 Underwater optical channel

The propagation of light under water is governed by the water optical properties [30]. Light can be subject to significant absorption and scattering due to its interaction with water molecules and dissolved particles, depending on both wavelength λ and water turbidity [35]. Hereafter, we consider $\lambda = 532\,\text{nm}$, which presents relatively low attenuation rates for low-turbidity waters [35]. Without loss of generality, we conduct our study for the case of clear ocean waters with the typical Chlorophyll concentration of $0.5\,\text{mg/m}^3$ [89].
For the sake of simplicity and in order to focus on the effect of solar noise, we model the power loss by the exponential decay model. This way, denoting the link span by Z, the channel loss L_{ch} is given by (refer to Section 2.3.3):

$$L_{\text{ch}} = \exp(-K\,Z), \tag{3.2}$$

where K is the diffuse attenuation coefficient. This model is better adapted to the case of an LED-based Tx, which cannot be considered as a collimated but rather a diffuse source, see [26].

3.3.2 Optical source power distribution

Without loss of generality, we model the LED radiation pattern by a generalized Lambertian model with azimuthal symmetry [90] as follows:

$$P_{\text{Tx}}(\phi) = P_{\text{t}}\,\frac{m+1}{2\pi}\cos^m(\phi) \quad [\text{W/sr}], \tag{3.3}$$

where P_{t} denotes the total emitted Tx power, $\phi \in [0, \pi/2]$ is the angle of irradiance, and m stands for the Lambertian order, given by $m = -\ln(2)/\ln(\cos(\phi_{1/2}))$, with $\phi_{1/2}$ being the Tx semi-angle at half-power.

3.3.3 Receiver optics considerations

The Rx employs a bandpass optical filter in order to attenuate the ambient light, i.e., background noise level. We denote by $T_s(\psi)$ the average filter transmission over the filter wavelength range $\Delta\lambda$ (i.e., filter bandwidth) for a specific angle of incidence ψ. We also consider an optical concentrator of gain $g(\psi)$, employed in order to increase the Rx effective area of light collection, A_{eff}. We have [91]:

$$A_{\text{eff}}(\psi) = \begin{cases} A_{\text{PD}}\, T_s(\psi)\, g(\psi)\, \cos(\psi), & 0 \leqslant \psi \leqslant \psi_c \\ 0, & \psi > \psi_c \end{cases} \tag{3.4}$$

where A_{PD} is the physical area of the PD, ψ is the angle of incidence, and ψ_c denotes the FOV (semi-angle) of the concentrator. We assume an idealized non-imaging concentrator [91], which provides a gain of:

$$g(\psi) = \begin{cases} \frac{n^2}{\sin^2(\psi_c)}, & 0 \leqslant \psi \leqslant \psi_c \\ 0, & \psi > \psi_c \end{cases} \tag{3.5}$$

where n is its internal refractive index. The advantage of using a non-imaging over an imaging concentrator is that it offers a higher FOV and therefore more flexibility regarding beam misalignments [92]. Note that by this model, we assume that the light received in the concentrator FOV is totally captured by the PD, i.e., neglect any limitation of the Rx FOV that could be caused by the PD.

3.3.4 Received optical power

Let us consider the Rx and Tx configuration illustrated in Fig. 3.3. Assuming perfect Tx-Rx alignment, the channel DC gain is given by [91, 93]:

$$H(0) = \begin{cases} \frac{m+1}{2\pi} \cos^m(\phi)\, \frac{A_{\text{PD}}}{Z^2}\, T_s(\psi)\, g(\psi)\, \cos(\psi), & 0 \leqslant \psi \leqslant \psi_c \\ 0, & \psi > \psi_c \end{cases} \tag{3.6}$$

where Z is the distance separating the Tx and the Rx, and ϕ and ψ are the Tx and Rx offset angle relative to the optical axis (i.e., the line-of-sight), respectively. Then, the received optical power P_{Rx} can be expressed as function of emitted power P_{Tx} as follows:

$$P_{\text{Rx}} = H(0)\, L_{\text{ch}}\, P_t. \tag{3.7}$$

3.3.5 Receiver electrical noise

In [72], Xu *et al.* provided a complete model for the Rx noise in terrestrial free-space optical communication systems. We use the main results of this paper in order to model the Rx electrical noises for the three cases of PIN, APD and PMT detectors within our context. We reasonably neglect the dark current noise assuming a Silicon

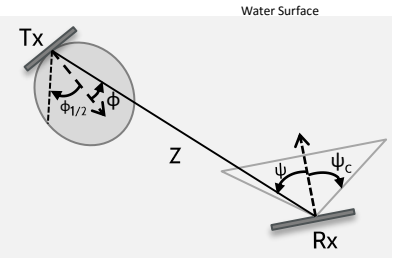

Figure 3.3: Illustration of the considered UWOC system and the related parameters.

(Si) PD for the case of PIN and APD [72, 94] and take into account the Rx thermal noise (mainly arising from the trans-impedance amplifier) and the photo-current shot noise, arising from input signal and/or background radiations.
The Rx thermal and shot noise are classically modeled by a zero-mean Gaussian and a Poisson random process, respectively. Concerning the latter, when the signal power or background radiations are of relatively high level, the corresponding average number of received photons is large enough so as to approximate the Poisson distribution by a Gaussian one [95] (obviously, this is not the case when working with very low signal levels where the Poisson model has to be used, as shown in [45]). The corresponding mean value is rejected by the ac-coupled receiver circuitry, therefore, the zero-mean Gaussian model also applies to the shot noise component [96]. The Gaussian model remains valid for the case of using an APD or similarly a PMT at the receiver (see [72] for more detail). Note that the square-law characteristic of the PD does not put into question this modeling. In fact, the contributions from the interaction of the signal with background radiations due to this non-linear characteristic of the PD can be practically neglected [72].

Let us denote by I the average photo-current generated by the PD, composed of signal (I_{s}) and noise (I_{b}) parts, that is, $I = I_{\mathrm{s}} + I_{\mathrm{b}}$. We have [72]:

$$I = \frac{\eta\, G\,(P_{\mathrm{s}} + P_{\mathrm{b}})\, e}{\hbar\, v} = I_{\mathrm{s}} + I_{\mathrm{b}}, \tag{3.8}$$

where η and G are the PD quantum efficiency and internal amplification gain, P_{s} and P_{b} denote the optical power of the desired signal and background radiations, and e, $\hbar$ and v denote the electron charge, the Planck constant, and the wave frequency, respectively. In the case of a PIN PD, we have $G = 1$. For an APD, the avalanche multiplication during the photo-detection process results in an internal amplification gain, $G = G_{\mathrm{APD}}$, that depends on the bias voltage and has its typical range between 10 and 200 [97]. For the case of a PMT, the produced output signal is obtained through photo-electron multiplication by means of secondary electron emissions, defined by the ratio δ at the multiplication stages, also called dynodes. Thus, the PMT is characterized by its internal gain $G = G_{\mathrm{PMT}}$, which depends on the number of dynodes n_{d} and the collection efficiency of the first dynode α. We have $G_{\mathrm{PMT}} = \alpha\, \delta^{n_{\mathrm{d}}}$ [98]. Hereafter, without loss of generality, we consider $\alpha = 1$.

Given (3.8), the general expression of the variance of the photo-current shot

noise is:

$$\sigma_{\text{sh}}^2 = 2\,e\,G\,F\,(I_{\text{s}} + I_{\text{b}})\,B, \tag{3.9}$$

where F is the PD noise figure, which is equal to one for a PIN PD. For the case of an APD, F depends on the ionization ratio ξ and the APD gain G_{APD} such that: $F = \xi G_{\text{APD}} + (2 - 1/G_{\text{APD}})(1 - \xi)$ [72]. For a PMT, F depends on the secondary electron emission ratio of the dynodes and is given by $F = \delta/(\delta - 1)$ [98]. Typical values of F for the case of PMT being close to unity, we consider $F \approx 1$ in this case. Also, we will denote by $\sigma_{\text{sh,b}}^2$ the variance of the shot noise arising from background radiations, that is,

$$\sigma_{\text{sh,b}}^2 = 2\,e\,G\,F\,I_{\text{b}}\,B. \tag{3.10}$$

On the other hand, the thermal noise is mostly generated by the load resistor of the TZ circuitry (see Fig. 3.2) and is modeled by a zero-mean Gaussian process of variance:

$$\sigma_{\text{th}}^2 = \frac{4KTB}{R_{\text{L}}}, \tag{3.11}$$

where K is the Boltzmann constant, T is the temperature in Kelvin, B is the Rx low-pass filter bandwidth, and R_{L} is the load resistance of the TZ amplifier.

Without loss of generality, we assume IM/DD, based on OOK, which has the advantage of implementation simplicity. Then, globally, the PD output current distribution is approximated by a Gaussian process that we denote by $\mathcal{N}(\mu_0, \sigma_0^2)$ and $\mathcal{N}(\mu_1, \sigma_1^2)$ corresponding to Off and On OOK symbols, respectively. We have:

$$\begin{cases} \mu_0 &= I_{\text{b}} \\ \sigma_0^2 &= \sigma_{\text{sh,b}}^2 + \sigma_{\text{th}}^2 = 2e\,G\,F\,I_{\text{b}}\,B + \frac{4KTB}{R_{\text{L}}} \end{cases} \tag{3.12}$$

$$\begin{cases} \mu_1 &= I_{\text{s}} + I_{\text{b}} \\ \sigma_1^2 &= \sigma_{\text{sh}}^2 + \sigma_{\text{th}}^2 = 2e\,G\,F\,(I_{\text{s}} + I_{\text{b}})\,B + \frac{4KTB}{R_{\text{L}}} \end{cases} \tag{3.13}$$

3.3.6 Signal detection

Let us denote by U_{out} the output voltage of the LPF at the Rx side, resulting from the current-voltage conversion by the TZ circuitry. Let us denote by $U_{\text{out,0}}$ and $U_{\text{out,1}}$ the output voltages corresponding to the bits '0' and '1', respectively. According to (3.12 -3.13), $U_{\text{out,0}}$ and $U_{\text{out,1}}$ can be approximated by the Gaussian processes $\mathcal{N}(\mu_0\,R_{\text{L}}, \sigma_0^2\,R_{\text{L}}^2)$ and $\mathcal{N}(\mu_1\,R_{\text{L}}, \sigma_1^2\,R_{\text{L}}^2)$, respectively. Thus, the probability density function of U_{out} is given by:

$$P(U_{\text{out}}|b) = \frac{1}{\sqrt{2\pi}\sigma}\exp\left(\frac{-(U_{\text{out}} - \mu)^2}{2\sigma^2}\right) \tag{3.14}$$

where b denotes the transmitted OOK symbols; for b = '0', we have $\mu = \mu_0 R_L$ and $\sigma = \sigma_0 R_L$, and for b = '1', we have $\mu = \mu_1 R_L$ and $\sigma = \sigma_1 R_L$.
We perform signal detection based on the maximum a posteriori (MAP) estimation criterion. Thus, the detected signal $\hat{b}$ can be estimated by :

$$\hat{b} = \arg\max_{b} P(U_{out}|b)\, P(b) \tag{3.15}$$

Assuming equiprobable symbols, i.e., $P(b) = 1/2$, $\hat{b}$ can be obtained by computing the likelihood ratio (LR) as follows [72]:

$$\mathrm{LR} = \frac{P(U_{out}|b=1)}{P(U_{out}|b=0)} = \frac{\sigma_0}{\sigma_1} \exp\left(\frac{(U_{out,0} - \mu_0 R_L)^2}{2\sigma_0^2 R_L^2} - \frac{(U_{out,1} - \mu_1 R_L)^2}{2\sigma_1^2 R_L^2} \right), \tag{3.16}$$

where $\hat{b} = 0$ for the case where LR < 1, else, $\hat{b} = 1$.

3.4 Solar noise modeling

3.4.1 Solar downwelling irradiance

In order to quantify the amount of solar irradiance captured by the Rx and its effect on the system performance, we consider the solar spectral downwelling plane irradiance that we denote by $E_{sun}(\lambda, D)$ in $\mathrm{W\,m^2\,nm^{-1}}$, where λ and D denote the wavelength and the operation depth (i.e., the depth at which the Rx platform is positioned), respectively. Measurements of E_{sun} at the sea level (i.e., at $D = 0$) can be found for instance in [39]. We have reproduced a part of these data in Fig. 3.4, where we notice an important difference between the presented irradiance plots, showing the strong dependence of E_{sun} on the weather conditions and sun positions (i.e., sunlight angle with respect to the zenith). Although these data do not describe the general case, using them allows us to approximate the Rx noise arising from solar radiations and therefore get an estimate of their effect on the system performance. In addition, these data are consistent with the measurements of the solar power spectral density by the American society for testing and material (ASTM) presented in [99].
Here, in order to investigate the worst impact of the solar noise on the Rx performance, we consider the case of the clear weather where the sun is located at the zenith. Under these conditions, E_{sun} reaches its peak value, as can be seen from Fig. 3.4, which is around $0.76\,\mathrm{W\,m^2\,nm^{-1}}$ for $\lambda = 532\,\mathrm{nm}$. When the sunlight penetrates in water, it decreases exponentially with the depth D [30]. We characterize the solar power decay underwater by the spectral diffuse attenuation coefficient K as follows (cf. Section 2.3.3):

$$E_{sun}(\lambda, D) = E_{sun}(\lambda, 0)\, t\, \exp\big(-K\, D\big), \tag{3.17}$$

Here, t is the water transmittance that is set to $t \approx 95\%$ for $\lambda = 532\,\mathrm{nm}$, based on the experimental data presented in [39] (see Fig.2.6). Although this value depends on the experiment conditions in [39], this could be considered as a typical

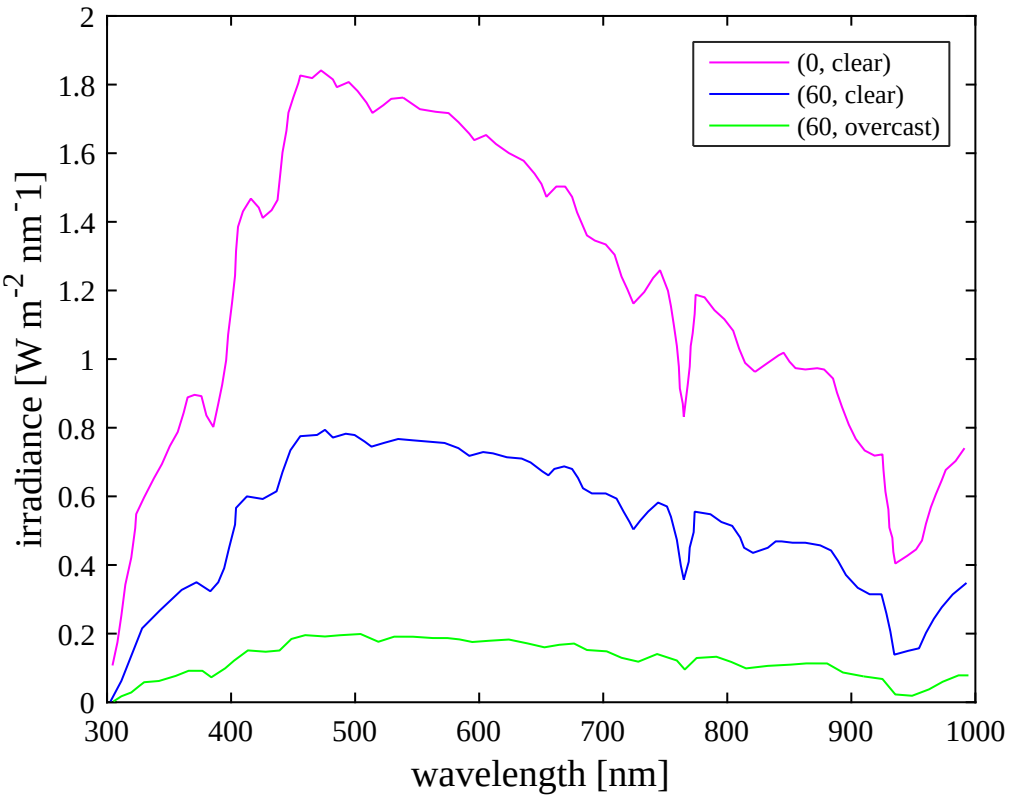

Figure 3.4: Sea-level solar spectral irradiance for different combinations of sun zenith angle and atmospheric conditions (reproduced from [39]).

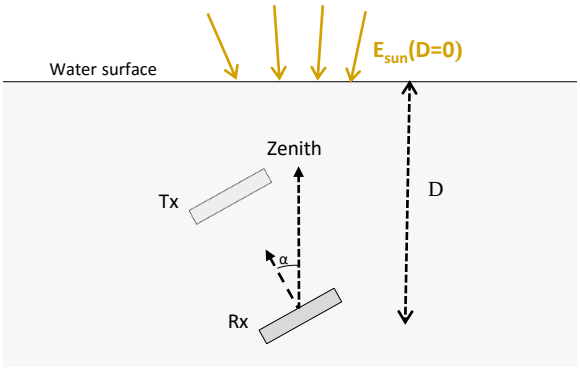

Figure 3.5: Illustration of the considered Sun and UWOC system configuration with the related position parameters.

value. Considering the case of clear ocean waters corresponding to a Chlorophyll concentration of $C \approx 0.5\,\mathrm{mg\,m^{-3}}$ (Jerlov type II water), we have $K = 0.08\,\mathrm{m^{-1}}$ for $\lambda = 532\,\mathrm{nm}$, according to the bio-optical models provided in Chapter 2.

3.4.2 Solar optical power

Let us consider the case study illustrated in Fig. 3.5, where α denotes the Rx inclination angle with respect to the zenith. The solar radiations captured by the PD generate an average photo-current I_b and a random component of variance $\sigma_\mathrm{b}^2 = 2\,e\,G\,F\,I_\mathrm{b}\,B$, see Subsection 3.3.5. In order to calculate I_b, we should first estimate the optical power of the solar noise captured at the Rx that we denote by P_b. Using E_sun, we can evaluate the sunlight irradiance (in $\mathrm{W\,m^{-2}}$) within the bandwidth $\Delta\lambda$ of the Rx optical filter. We assume that the Rx light collecting surface captures the solar irradiance according to the cosine law [47]. We further assume that there is no effect of obstruction or spatial filtering at the Rx side to limit the solar irradiance (this can be considered as a worst case). Then, P_b can be calculated as follows.

$$P_\mathrm{b} = \begin{cases} E_\mathrm{sun}(D)\,t\,\Delta\lambda\,\exp(-K\,D)\,A_\mathrm{eff}\,\cos(\alpha), & 0 \leqslant \alpha \leqslant \psi_\mathrm{c} \\ 0, & \alpha > \psi_\mathrm{c} \end{cases} \tag{3.18}$$

Note that by (3.18), we implicitly assume that the solar irradiation spectral density underwater is constant over the considered Rx optical filter bandwidth (typically on the order of several nm to several tens of nm), which is a fair approximation in practice [3].

3.5 Numerical results

We present in this section some numerical results in order to quantify the impact of solar noise on the performance of a typical UWOC link operating in clear ocean waters. The rationality of this choice of water type is that background light can

Table 3.1: Tx-Rx parameter specification

(a) Tx

Parameter	Value
λ	532 nm
$\Delta\lambda$	30 nm
P_{Tx}	100 mW
$\phi_{1/2}$	15 °
R_{b}	10 Mbps

(b) Rx

Parameter	Value
η	0.82
R_{L}	50 Ω
$\Delta\lambda$	30 nm
G_{APD}	50
ξ	0.02 (for APD)
n_{d}	9 (PMT) [101]
δ	6 (typical PMT) [98]

have its most significant impact on the link performance in clear waters, where it can penetrate in larger depths [3]. In fact, given the considered link configuration, although for higher turbidity waters we have a more significant contribution of multiple scattering effect in the received ambient light intensity at the Rx, the high channel loss due to absorption and scattering has a more dominant effect and makes the link less susceptible to solar noise, compared to the case of clear waters. Nevertheless, more in-depth investigation would be necessary for the case of a horizontal link.

We further assume perfect beam alignment and time synchronization between the Tx and the Rx. Data transmission is performed according to uncoded NRZ OOK signaling. This way, an information bit corresponds to transmitting a rectangular pulse of duration equal to the symbol duration and of intensity level $P_{\text{Off,OOK}}$ and $P_{\text{On,OOK}}$ corresponding to bits '0' and '1', respectively. We assume that for sending bit '0', we switch off the LED, i.e., we take $P_{\text{Off,OOK}} = 0$.

3.5.1 Parameter specification

The considered Tx and Rx parameters are specified in Table 3.1. Here, $R_{\text{b}} = 10\,\text{Mbps}$ is the data transmission rate, which can be readily attained using the typical off-the-shelf available LEDs (for instance, LUXEON Rebel Color components [90]). The LED is considered to emit at the wavelength $\lambda = 532\,\text{nm}$ with a Lambertian order of 20, resulting in $\phi_{1/2} \approx 15°$. We assume that the three PD types, i.e., PIN, APD, and PMT, have equal surfaces and quantum efficiencies. We also consider the bandwidth of $\Delta\lambda = 30\,\text{nm}$ for the passband optical filter that matches the LED spectral width [90] and, for the sake of simplicity, assume that $T_{\text{s}}(\psi) \approx 1$ [100].

We have not specified the Rx FOV ψ_{c} and A_{PD} in the table because as it can be seen from (3.18), the optical power P_{b} of the solar radiations captured at the Rx depends on both of these parameters. Therefore, in our performance study we will later consider a range of values for ψ_{c} and A_{PD} of practical relevance in order to describe various Rx configurations. The considered values of the Rx FOV and

Table 3.2: Simulated Rx FOVs

FOV	0.5°	1°	2°	4°	8°	16°	45°

Table 3.3: Simulated Rx aperture diameters

d_{PD}	5 mm	10 mm	1 in	2 in	3 in	4 in

aperture size are presented in Tables 3.2 and 3.3, where $A_{\mathrm{PD}} = \pi\, d_{\mathrm{PD}}^2/4$. It is worth mentioning that the receiver filters corresponding to the largest FOVs specified in Table 3.2 may not be practically realizable or will be very expensive, in particular, given the 30 nm filter bandwidth that we assumed, see Table 3.1(b). However, we consider these values here for the sake of completeness of our study.
On the other hand, in Table 3.3, the smallest aperture sizes correspond to the typical available PD devices (e.g. by Hamamatsu). The largest d_{PD} values, however, are less relevant for PIN and APD devices, given the relatively high data rate of 10 Mbps considered here. Nevertheless, considering these values is interesting as this allows to see the ultimate effect of the aperture size [102].

3.5.2 System performance in the absence of solar noise

In order to have a benchmark in our study of the impact of solar background noise on the performance of an UWOC link, we start by evaluating the system BER in the absence of solar noise. We conduct this study for the three PD cases described in Section 3.3.5. Note that our main goal is not to compare the performances of these PDs but rather to have a benchmark of their respective performances, useful for further investigations. We have presented in Fig. 3.6 the variations of BER versus link range Z, independently of the operation depth D (which does not influence the system performance in the present study), and for different values of the Rx FOV ψ_{c} and aperture diameter d_{PD}. Note that, calculating the Rx SNR for each Z, the BER for uncoded OOK can be readily calculated [103]. Here, the expression of the BER is given by [40]:

$$\mathrm{BER} = \frac{1}{2}\int_0^{\Upsilon}\left(\frac{1}{\sqrt{2\pi\sigma_1^2}}\exp\left(-\frac{(x-\mu_1)^2}{2\sigma_1^2}\right)\right)dx + \frac{1}{2}\int_{\Upsilon}^{\infty}\left(\frac{1}{\sqrt{2\pi\sigma_0^2}}\exp\left(-\frac{(x-\mu_0)^2}{2\sigma_0^2}\right)\right)dx \tag{3.19}$$

where Υ denotes the threshold level to be set so as to minimize the error probability, and (μ_0, σ_0^2) and (μ_1, σ_1^2) are defined in (3.12)-(3.13).

3.5.2.1 Effect of Rx FOV

We first fix the Rx aperture to $d_{\mathrm{PD}} = 5$ mm and investigate the effect of changing the Rx FOV ψ_{c}. This d_{PD} corresponds to the smallest PD size in Table 3.3 but is

typical of available PIN and APD devices. Results are shown in Figs. 3.6 (a), (c) and (e), for PIN-, APD-, and PMT-based receivers. The dotted horizontal lines correspond to BER = 10^{-4} that we consider as target BER. Note that a *raw* BER of 2×10^{-3} is usually considered as sufficiently low for an uncoded system, which can readily be reduced to less than 10^{-9} by employing error correction coding [104] (see [66, 105], for instance). For the three considered PDs, we notice an improvement in terms of maximum achievable link distance when ψ_c is reduced. Indeed, varying ψ_c form 45° to 0.5° allows an increase in the link span of about 50, 70, and 87 m, for the cases of using the PIN, APD and PMT, respectively. This increase in the link span is in fact due to the increase in the optical concentrator gain $g(\psi)$ by reducing the Rx FOV, see (3.5) (remember that in this section we assume the absence of solar noise). Considering $\psi_c = 0.5°$, we notice the maximum link range of 57, 93, and 147 m for PIN-, APD-, and PMT-based receivers, respectively, for a target BER of 10^{-4}. This illustrates the significant performance improvement when using a PMT, compared to PIN or APD, as expected. Notice that such a comparison is relevant because all the three PD types were assumed to have the same active area.

3.5.2.2 Effect of Rx aperture size

Let us now fix the Rx FOV to $\psi_c = 16°$ and see the impact on the performance by varying d_{PD}. Such a moderate Rx FOV would make a good compromise between facilitating link alignment and minimizing geometric optical power loss. Simulation results are presented in Figs. 3.6 (b),(d) and (f), for PIN, APD, and PMT cases, respectively. As expected, the maximum achievable link distance increases as the Rx aperture increases, since the captured intensity by the Rx is proportional to its collection area. Indeed, varying d_{PD} form 5 mm to 101.6 mm (4 inch), allows a distance gain of 38, 52, and 61 m, for the cases of PIN, APD, and PMT, respectively. It is worth mentioning that the largest PD sizes may be considered as irrelevant from a practical point of view. Especially, considering these values assumes that we are not concerned by the practical fabrication issues of the corresponding non-imaging concentrator. That is to say, we implicitly assume that we have adapted concentrator and optics to the PD size.

3.5.3 Impact of solar background noise

Now let us investigate the impact of background noise on the system performance. Our aim is first to elucidate the effect of solar radiations when using different PD types, and secondly to identify the conditions under which the assumption of neglecting the solar noise is rational.

3.5.3.1 Simulation parameters and assumptions

Because solar rays' power is attenuated as they penetrate in water, we study the BER performance as a function of the operation depth that we define as the Rx depth D. Considering a target BER of 10^{-4} in the absence of solar noise, we

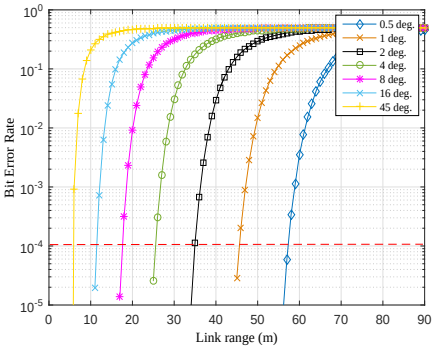

(a) PIN ($d_{\mathrm{PD}} = 5\,\mathrm{mm}$)

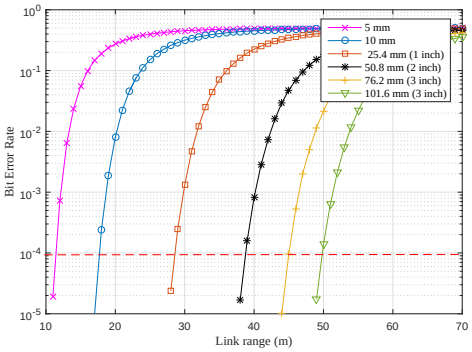

(b) PIN ($\psi_{\mathrm{c}} = 16^{\circ}$)

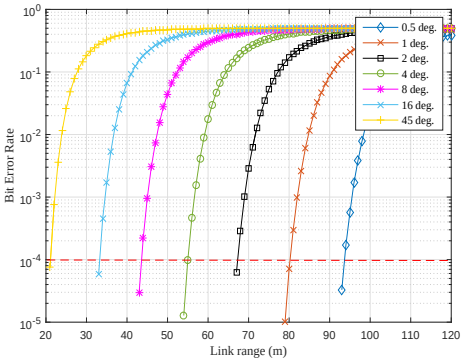

(c) APD ($d_{\mathrm{PD}} = 5\,\mathrm{mm}$)

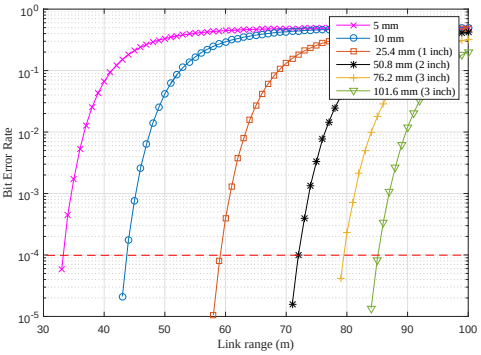

(d) APD ($\psi_{\mathrm{c}} = 16^{\circ}$)

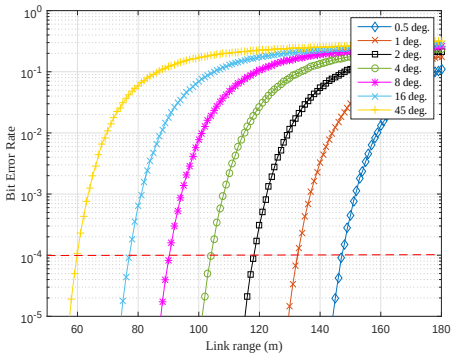

(e) PMT ($d_{\mathrm{PD}} = 5\,\mathrm{mm}$)

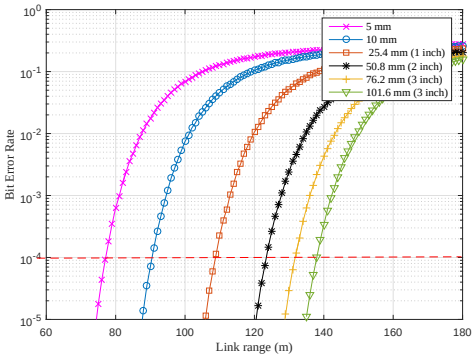

(f) PMT ($\psi_{\mathrm{c}} = 16^{\circ}$)

Figure 3.6: BER performance as a function of link range Z for PIN-, APD-, and PMT-based receivers in the absence of solar noise. P_{Tx}= 0.1 W, uncoded OOK modulation, Jerlov type II waters with Chlorophyll concentration of $C = 0.5\,\mathrm{mg.m}^{-3}$. Two cases of fixed Rx aperture size and fixed Rx FOV (left and right sub-figures, respectively) are considered.

fix the link range Z for each PD type, and investigate the variations of BER as a function of D in the presence of solar noise. We have provided the corresponding

Table 3.4: Link span Z(m) satisfying BER $\approx 10^{-4}$ for different Rx FOVs ψ_c in the absence of solar noise.

FOV	0.5°	1°	2°	4°	8°	16°	45°
PIN	57.1	45.4	34.9	25.3	17.3	11.1	5.6
APD	93.5	80.1	67.2	55.0	43.4	33.1	21.0
PMT	147.2	132.5	118.1	104.0	90.2	77.1	59.9

Table 3.5: Link span Z(m) satisfying BER $\approx 10^{-4}$ for different Rx aperture diameters d_{PD} in the absence of solar noise, $\psi_c = 16°$.

d_{PD}	5 mm	10 mm	1 inch	2 inch	3 inch	4 inch
PIN	11.1	17.4	28.3	38.6	45.0	49.7
APD	33.1	43.5	59.1	72.0	79.3	85.1
PMT	77.1	90.4	108.7	123.3	131.7	137.9

link spans Z for different values of the Rx FOV and aperture diameter in Tables 3.4 and 3.5, respectively. To study the impact of the solar noise, we consider the worst case configuration where the sun is at the zenith. This corresponds to the peak value of E_{sun} (see Section 3.4 and Fig. 3.4). We further assume that the Rx plan is directed towards the sea surface, i.e., we set $\alpha = 0°$, generating a maximum of captured solar irradiation, see (3.4)-(3.7) and Fig. 3.3. Note that although this assumption, as well as that of the absence of spatial filtering or obstruction, are not likely to happen in practice, this worst case study determines the maximum limitation on the system performance. In other words, for a set of system parameters, the specified 'pessimistic' noise-free depth will be valid for any system configuration and operation scenario. Nevertheless, the case of vertical links is typical, for instance, in the case of data upload from an AUV to a ship or a submarine, or in the case of data-muling by an AUV or an ROV.
An illustration of the afro-mentioned assumptions and the test scenarios are illustrated in Fig. 3.7. Note that the link range Z is being fixed for each test case, and its value depends on the considered configuration parameters (i.e. the value of FOV and / or d_{PD}) .

3.5.3.2 Solar noise impact as a function of Rx FOV

We have presented in Figs. 3.8 (a), (c) and (e) simulated BER results as a function of the Rx depth D for $d_{PD} = 5$ mm and the three PD types and different values of the Rx FOV. Note that the link span Z varies depending on the PD type and ψ_c, see Table 3.4. These figures illustrate the role of the Rx depth in the performance degradation caused by the solar noise. As expected, the Rx BER performance strongly deteriorates in relatively small depths. For instance, considering a small

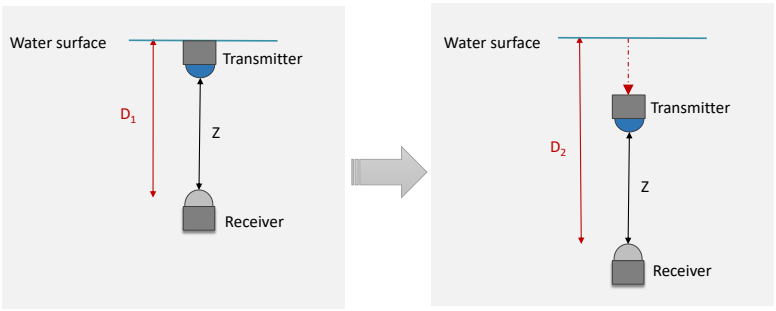

Figure 3.7: Illustration of the test scenarios simulated to estimate solar noise effect.

FOV of $\psi_c = 0.5°$, the BER approaches 10^{-1} at depths around 80, 190, and 325 m, for the cases of PIN, APD, and PMT, respectively. The BER converges to the target value of $\sim 10^{-4}$ (in the absence of background noise) for depths larger than about 140, 250, and 400 m for PIN, APD, and PMT cases, respectively. Given that we are considering the worst case configuration concerning the solar noise effect, we can for sure neglect the the solar background noise effect for depths larger than these values, whatever the transmission scenario. Here, reasonably, PMTs are more sensitive to background noise than APD or PIN PD.

Furthermore, we notice that increasing the Rx FOV makes the Rx performance less vulnerable to background noise. For instance, if we increase ψ_c form 0.5° to 45°, the minimum depth at which the target BER can be attained decreases by ~ 100 m for the three PD cases. In other words, by increasing the Rx FOV, the link performance is less affected by the background noise. This finding may seem strange since one may expect that a larger FOV should rather result in more collected solar radiations at the Rx, and hence, should impact more significantly the Rx performance. To explain this behavior, firstly note that for the different FOV values considered here, the signal level is kept as constant (the corresponding links spans can be found in Table 3.4). Secondly, remember that we are considering the use of a non-imaging concentrator at the Rx, for which a larger FOV corresponds to a smaller concentrator gain, see (3.5). This, in turn, results in a reduction of the intensity of the background radiations captured at the Rx.

3.5.3.3 Solar noise impact as a function of Rx aperture size

We have presented the simulated BER results in Figs. 3.8 (b), (d) and (f), for $\psi_c = 16°$ and different PD diameters, considered in Table 3.3. The corresponding link spans Z depend on d_{PD} and the PD type, see Table 3.5. We notice that, unlike the FOV, when the Rx aperture increases, the depth limit under which the Rx performance is not affected by the background noise, increases. Indeed, varying d_{PD} from 5 mm to 4 inch increases the depth limit by ~ 80 m for the three PD cases. In

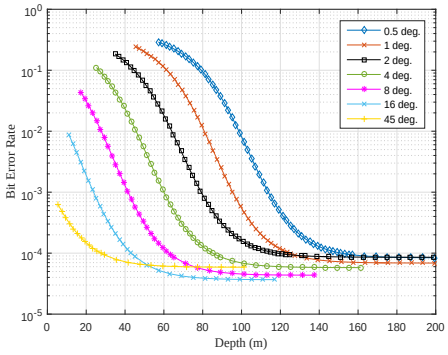

(a) PIN ($d_{\mathrm{PD}} = 5\,\mathrm{mm}$)

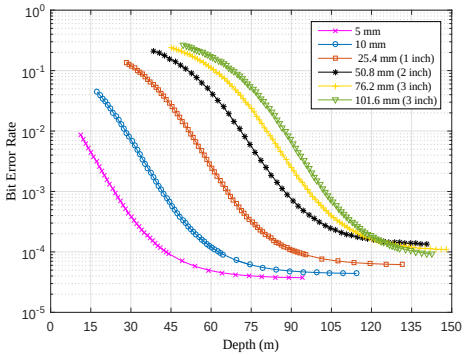

(b) PIN ($\psi_{\mathrm{c}} = 16°$)

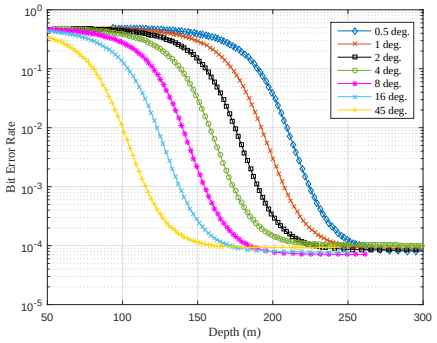

(c) APD ($d_{\mathrm{PD}} = 5\,\mathrm{mm}$)

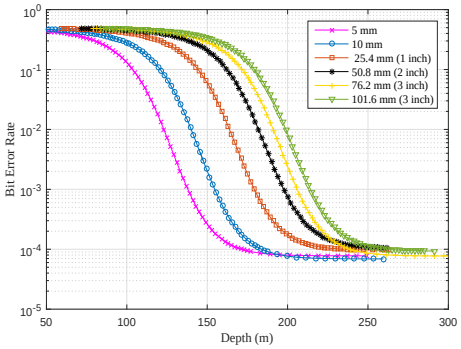

(d) APD ($\psi_{\mathrm{c}} = 16°$)

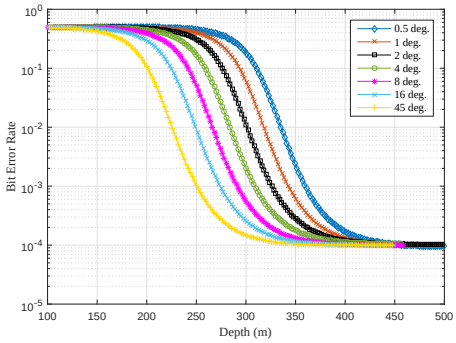

(e) PMT ($d_{\mathrm{PD}} = 5\,\mathrm{mm}$)

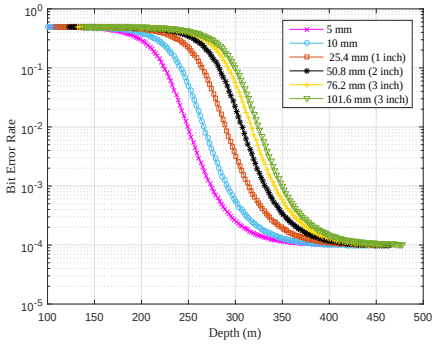

(f) PMT ($\psi_{\mathrm{c}} = 16°$)

Figure 3.8: Impact of solar noise on the BER performance as a function of the Rx depth D for PIN-, APD-, and PMT-based receivers. $P_{\mathrm{Tx}} = 0.1\,\mathrm{W}$, uncoded OOK modulation, Jerlov type II waters with Chlorophyll concentration of $C = 0.5\,\mathrm{mg.m}^{-3}$. Two cases of fixed Rx aperture size and fixed Rx FOV (left and right sub-figures, respectively) are considered.

other words, for increased PD size, the link performance is affected more considerably by the background noise. This is explained by the fact that the captured solar

radiation intensity by the Rx is proportional to the Rx collection area, assuming the ideal non-imaging concentrator at the Rx, see (3.4) and (3.18). Overall, for different link configurations, we can deduce from these results the minimum depth at which the communication can take place without being effectively impacted by the solar noise.

3.6 Conclusions and discussions

In this chapter, we investigated the potential impact of solar background noise on the performance of point-to-point UWOC links for the three PD types of PIN, APD, and PMT. Considering an accurate model for the received solar noise at the Rx, we presented through numerical results a comprehensive study of the noise effect on the system performance for different Rx parameters. In particular, we showed how the sensitivity to solar radiations varies depending on both the operation depth and the Rx characteristics. Indeed, for relatively low depths (typically less than 80 m), a PIN-based Rx has more robustness against the background noise, compared to APD- and PMT-based receivers. This latter was shown to be very sensitive to solar radiations and should be used in receivers working at relatively large operational depths, i.e., more than 200 m. The results we presented are insightful for UWOC system designers and also users when these links have to be deployed in relatively shallow waters where the propagation medium cannot be considered as dark.

The real impact of the background noise on the Rx performance depends on a number of parameters, including the sun position and its radiation intensity, the direction of the Rx as well as its aperture size and FOV, the type of Rx concentrator, the spectral/spatial response of the Rx optical filter, etc. Studying the effect of each parameter regarding the received solar noise on the PD would not be practically useful and exploitable. Therefore, in the presented simulation results, we considered the worst case for the link configuration where the maximum of the solar radiations was captured by the Rx, although such a case may rarely happen in practice. Nevertheless, the interest of studying this worst case is that the *pessimistic* limits that we provided for the effectively noise-free operation will apply to any other link configuration. In a real-field link deployment, the considered Rx types can tolerate smaller operation depths and can function in shallower waters that those deduced here. Thanks to the presented model, one can calculate the noise level for any specific link parameters and solar radiation PSD, and investigate the real impact on the link performance for a given UWOC link deployment scenario.

After this study of the background noise effect, we will hereafter focus on the extension of UWOC link span by using the recent and particularly promising photodetectors, i.e., silicon photo-multipliers. Our main objective is to attain high data rates when using these components. For this reason, we will consider the case where the system is operating in deep waters, i.e., at large enough depths where background solar noise can be neglected.

Chapter 4

Silicon Photomultipliers for UWOC applications

Contents

4.1 Introduction

Because of the strong attenuation in water due to the absorption and the scattering of light, UWOC link ranges are limited to few tens of meters typically unless PMTs are employed. The use of PMTs, however, goes along with disadvantages such as high sensitivity to ambient light, high operation voltage, and bulkiness, as explained in Section 2.4.2. In order to increase significantly the transmission range, and as a promising alternative to PMTs, here we investigate the use of very recent PDs, i.e., Silicon photomultipliers (SiPMs), which stand out for their high sensitivity to low optical signal levels, down to a single photon [106]. Compared to PMTs, SiPMs offer several advantages including low operation voltage, insensitivity to magnetic fields and mechanical robustness.

In this chapter, our main objective is to highlight the interest of employing the SiPMs in the UWOC context as compared to rather classical photodetectors of APDs and PMTs. Furthermore, we investigate different modulation techniques to be employed with SiPMs, in the aim of further improving the link performance. For this, we consider binary level modulation schemes, i.e., OOK and pulse position modulation (PPM); and also pulse amplitude modulation (PAM) which is a multi-level modulation schema. We study the bandwidth efficiency of these modulation techniques, and evaluate their performance in terms of the maximum achievable error-free link distance.

The remainder of the chapter is organized as follows. In Section 4.2, we present a literature review on SiPM components and their applications. In Section 4.3, an overview of SiPMs is presented including their working principle, performance parameters, and the photon-counting procedure. Next, we investigate the suitability of employing SiPMs in the context of UWOCs in Section 4.4. Then, in Section 4.5, we present a study of the suitable modulation techniques than can be employed with SiPMs. Lastly, Section 4.6 concludes the chapter.

4.2 Literature review

Whereas light emitting diodes are mostly used at the Tx in UWOC systems for the reasons of higher power, lower cost and beam alignment simplicity, the choice of the PD at the Rx remains debatable.

Remember from Section 3.3, the main classical PDs are PINs, APDs and PMTs. The PIN PDs appear to be an unsuitable within this context due to high optcal beam attenuation in the aquatic medium and are challenged by APDs, interesting due to their inherent gain. APDs have been considered in several previous experimental and theoretical works, e.g. [49, 46] and offer the advantages of a solid-state PD, such as mechanical robustness and compactness. On the other hand, PMTs have drawn particular attention in the context of UWOCs thanks to their high sensitivity to very low intensity signals (down to a few photons) and high gain [18, 49]. They have been considered in several experimental prototypes, e.g. in [107], and used in the BlueComm modem, developed by Woods Hole oceanographic institution (WHOI) and commercialized by Sonardyne [67]. However, PMTs are bulky and more expensive, require high voltage for operation, are very sensitive to magnetic fields, and are more easily damaged by exposure to high-intensity light, such as ambient light [3].

Very recently, SiPMs, also known as multi-pixel photon counters (MPPCs), have emerged as an interesting photo-detection solution when working with very low light intensity levels down to a single photon [106]. SiPMs have been reported to offer several advantages such as high gain ($> 10^5$), low operation voltage ($< 30\,\mathrm{V}$ for SensL SiPMs [106]), insensitivity to magnetic fields, mechanical robustness, and tolerance regarding exposure to ambient light. A summarized comparison between SiPMs and other PD types is presented in Table 4.1, [106].

Table 4.1: Comparing the characteristics of PIN, APD, PMT, and SiPM PDs (adapted from [106])

	PIN	**APD**	**PMT**	**SiPM**
Gain	1	$\sim 10^2$	$\sim 10^6$	$\sim 10^6$
Operational Bias	Low	High	very High	Low
Temperature Sensitivity	Low	low	Low	High [109]
Mechanical Robustness	High	High	Low	High
Ambient light exposure?	OK	OK	No	OK
Peak sensitivity wavelength	Red	Red	Blue/UV	Blue [110]
Readout / Electronics	Simple	Complex [10]	Simple	Simple
Size	Compact	Compact	Bulky	Compact
Sensitive to magnetic fields?	No	No	Yes	No

The use of SiPMs comes along with some challenges, among which the strong dependence of their performance on the bias voltage and the temperature for instance [108]. The main effects of temperature on the SiPM are a change in the breakdown voltage of the constituting photodiodes (see Section 4.3), affecting a number of the SiPM's characteristics, and in the dark count rate (see Section 4.3 for further details) [106]. Thus, for a stable functioning of SiPM-based receivers, it is crucial to regulate the operation temperature. Another major limitation of SiPMs is the relatively high level of signal-dependent noise that we will explain latter in this chapter.

The reflection about using SiPMs in optical communications was initiated in [111, 112], where the feasibility of their use as PD was proven. In [113] these devices were considered for the design of inexpensive yet very sensitive receivers for plastic optical fiber links, capable of detecting small number of photons over long distances. In [114, 115, 116], SiPMs were investigated in the context of long-distance and low-power visible light communications (VLC) together with optical orthogonal-frequency-division-multiplexing (OFDM) signaling; for instance, for downhole monitoring applications. In particular, an experimental work in [117] demonstrated a 200 Mbps data rate VLC link.

4.3 SiPM-based receiver

4.3.1 Working principle

An SiPM is a solid state detector comprising a densely packed array of micro APDs (typically 100 up to 10,000 per mm^2) operating in the Geiger mode, i.e. biased slightly 10 to 20 per cent [108] above the breakdown voltage. Under this operation mode, the APD, referred here to as a single photon avalanche diode (SPAD), has the advantages of large gain (on the order of 10^6) and high sensitivity to very low optical intensity levels (down to one photon). A schematic representation of an

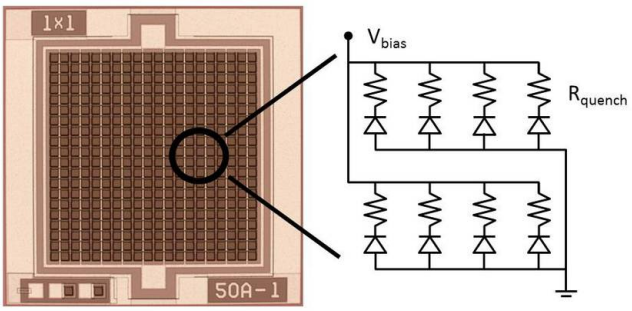

Figure 4.1: Top view and schematic of an SiPM reproduced from [118]. Each SPAD has an individual quenching resistor.

SiPM is presented in Fig. 4.1.

Quenching methods: When a photon hits the SPAD sensitive area, it launches an avalanche breakdown within the SPAD, resulting in a high current flow through the diode. In order to recover, each SPAD is connected to a load device (also called quenching device) whose main function is to lower the bias voltage across the diode; the combination SPAD-quenching device will be referred to as a micro-cell or a pixel hereafter. The discharge of one fired microcell leads to generating an output pulse, whose amplitude and characteristics are independent of the incoming light intensity. The simplest and common approach to halt the diode breakdown is to employ a high Ohmic resistor, connected in series with the SPAD (see the inset circuit schematics of Fig. 4.2); This method is known as passive quenching (PQ). The functioning cycle of a passively quenched SPAD is depicted in Fig. 4.2. It consists in the following steps:

- **Step (1)**: The SPAD is biased above the breakdown voltage, at $V = V_{\text{bias}}$. Initially, it is in an idle mode, i.e., ready to detect an incoming photon.
- **Step (2)**: A photon hits the SPAD sensitive area and launches a discharge which results in a high current flow through the diode.
- **Step (3)**: The quenching device, here a resistor, halts the discharge by lowering the bias voltage down to the break down voltage, denoted by V_{bd}.
- **Step (4)**: The diode recharges until $V = V_{\text{bias}}$ where it returns to the idle state.

Another case figure consists in employing a dedicated electronic circuit to quench the SPAD beakdown. It proceeds by decreasing the SPAD bias voltage under the breakdown voltage for a certain period of time until the breakdown is quenched [108]. This method is known as active quenching (AQ). The functionning cycle of an AQ is identical to that described in Fig. 4.2. Although an AQ devise is reported to provide higher counting rates, a tight SiPM parameter control, and no SPAD

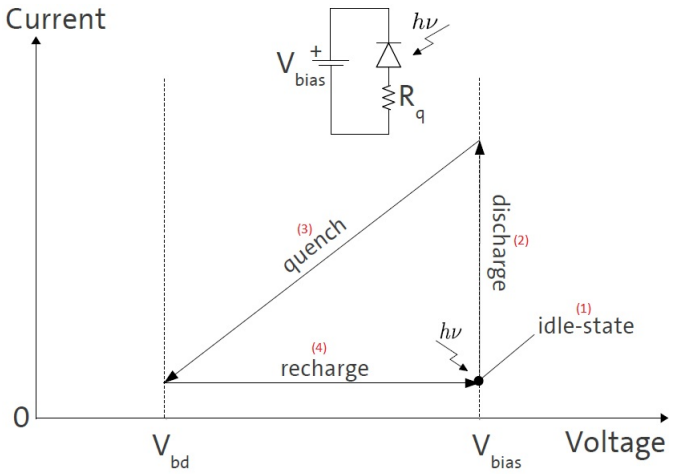

Figure 4.2: The current voltage dependence of a working SPAD with passive quenching, reproduced from [119]. The diode discharge is triggered by the detection of a photon.

paralysis due to saturation (see Section 4.3.4), it is more complex, and requires more power and area. In addition, to the best of our knowledge, there exist very few products that employ AQ technology, with a very reduced number of constituting micro-cells (less than ten typically), e.g. 1×8 SPAD by ID Quantique [120]. In contrast, passive quenching-based SiPMs (PQ-SiPMs) have been developed in large scale, are composed of a large number of micro-cells (up to 10,000) [121], and offer light sensitivity performances comparable to those of AQ-SiPM [41].

4.3.2 Performance parameters

The performance of an SiPM depends on several parameters, that we introduce hereafter.

Photon detection efficiency (PDE): The PDE is the statistical probability that a photon will heat the sensitive area of the SiPM and will generate a Geiger pulse from one of the micro-cells composing it. It is defined as the product of the quantum efficiency, the fill factor, and the probability that a detected photon will generate an avalanche. Here, the fill factor is equal to the ratio of the active area to the total physical area of the SiPM, taking into account the physical gaps between the micro-cells. The value of the PDE depends on both light wavelength and the bias voltage. We denote this parameter by Υ_{PDE}.

Dark count rate (DCR): The dark photon counting is the main source of the SiPM noise. It results from the breakdown of a micro-cell due to thermally generated electrons, instead of the signal payload photons. This results in the modification (and as a matter of fact, the increase) of the SiPM photon count output. Note that the signals resulting from the breakdown of the cell, due to either photoelectrons or thermally generated electrons, are identical [116].

The average number of dark counts per second is referred to as DCR and is regarded as a fixed and signal-independent noise. Hereafter, the average DCR of an SiPM is denoted by f_{DCR}.

After-pulsing (AP) probability: The AP is a noise source affecting the SiPM PD. It is defined as the re-trigger of one SPAD by trapped carriers at its output from previous avalanche events. Thus, this noise is regarded as signal dependent. We denote the probability of AP by P_{AP}.

Optical cross-talk (CT): The CT is another noise source within the SiPM. It occurs when an avalanching micro-cell initiates a breakdown in one or several neighbouring micro-cells. It is defined by the probability P_{CT}, whose value depends on a the SiPM over-voltage (difference between the bias and the breakdown voltages, i.e., $V_{\mathrm{bias}} - V_{\mathrm{bd}}$) and the distance between neighbouring microcells [106].

Dead time: The micro-cell dead-time, τ_{d}, also known as the recovery time, is a key parameter of an SiPM. It is the time needed by a micro-cell to recharge (step (4) in Fig. 4.2). During this time interval, the SPAD is unable to detect any arriving photon. Thus, τ_{d} is also referred to as the microcell reset period and for the case of PQ-SPAD is given by $\tau_{\mathrm{d}} = C\,R_{\mathrm{q}}$, where C is the effective capacitance of the microcell and R_{q} is the value of the quench resistor. Since C depend upon the micro-cell area, the reset time will vary for different microcell sizes; an SiPM composed of 100μm diamter SPADs having a significantly longer reset time than that with 20μm diamter SPADs [106].

4.3.3 Photon-counting procedure

When the incoming light (and thus the photon flux) hits the photo-sensitive area of the SiPM, each micro-cell proceeds to individual photon counting. Given that it is operating in the Geiger mode, the SPAD can be assumed as an ideal single photon counter whose detection process can be approximated by a Poisson distribution (illustrating the shot noise effect) [116]. The SPAD generates an output pulse as a reaction to the detection of a photon, as described earlier. Counting these pulses over a time interval Δt is equivalent to counting the number of detected photons over Δt; The sum of the individual SPAD counts forms the SiPM output [116]. Thus, the information about the detected light intensity is generated by the internal superposition of the signal of all fired microcells [118]. This is schematically illustration in Fig. 4.3, where N stands for the number of SPADs composing the SiPM, $C_{\mathrm{ph}}(i)$ corresponds to the photon count related to SPAD number i, and C_{ph} is the SiPM photon-count output. It should be noted that this operation procedure is only valid when the device is operating in the linear mode, i.e. where the SiPM output is proportional to the input signal magnitude.

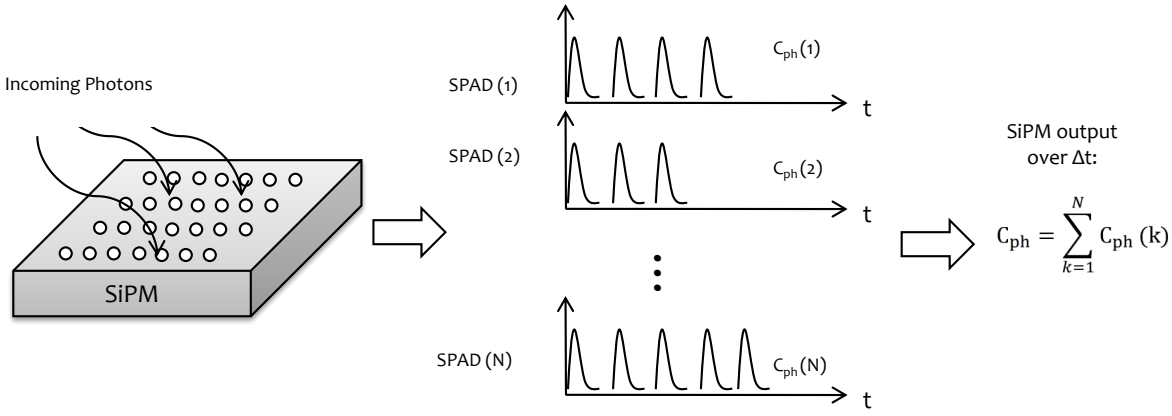

Figure 4.3: Photon-counting procedure with an SiPM PD

Mathematical formulation: As explained above, the output photon count C_{ph} of the SiPM is equal to the sum of individual counts from the SPADs, $C_{\text{ph}}(i)$:

$$C_{\text{ph}} = \sum_{i=1}^{N} C_{\text{ph}}(i)\,. \tag{4.1}$$

We assume that the SiPM has an ideal photon counter behaviour and model its photo-detection by a Poisson distribution [116] as follows:

$$\Pr(C_{\text{ph}} = k) = \exp(-\mu)\,\frac{\mu^k}{k!}\,, \tag{4.2}$$

Here, μ denotes the average photon count and is expressed as a function of the captured optical power by the Rx as follows [114]:

$$\mu = \left(\frac{\Upsilon_{\text{PDE}}\,P_{\text{Rx}}}{E_{\text{ph}}} + f_{\text{DCR}}\right)\,(1 + P_{\text{AP}} + P_{\text{CT}})\,T\,, \tag{4.3}$$

where T denotes the bit time and $E_{\text{ph}} = \hbar c/\lambda$ is the energy of photon, with $\hbar$, c, and λ being the Planck constant, the speed of light, and the light wavelength, respectively.

4.3.4 Non-linear distortion

The main challenge related to SiPM use is the fact that its response suffers from a non-linear distortion (NLD) [116]; When the incoming optical signal is lower than a certain level, the SiPM operates in a linear mode. Then, above a certain signal level, and before saturation, the SiPM output deviates slightly from the linear response. This is because a single microcell can detect only one photon at a time, i.e., it generates a single output pulse regardless of the number of incident photons that initiated it. As the number of incident photons per microcell per second increases, the probability that two or more photons will interact in the same microcell at the

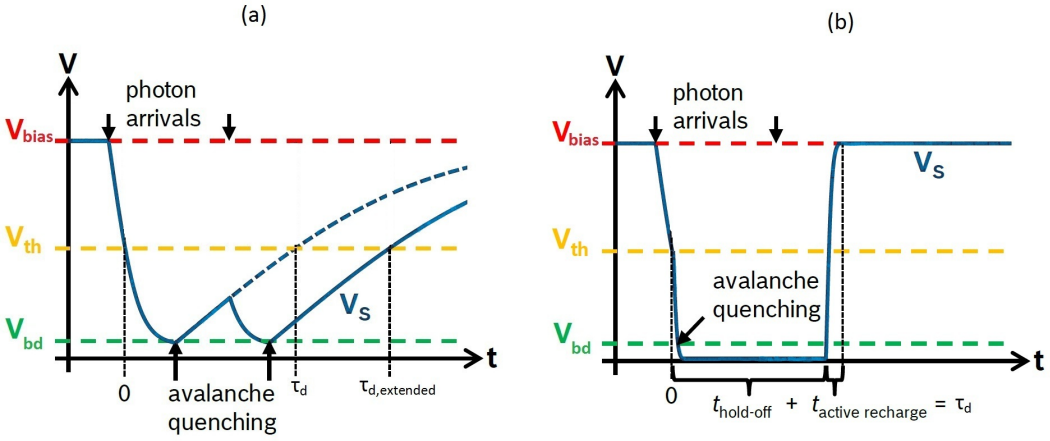

Figure 4.4: Variation of the SPAD voltage V_s when an extra-incident photon arrives during the dead time τ_d, for a (a) PQ- and (b) AQ-SPAD respectively, reproduced from [122]

same time will increase. So, the SiPM goes into a saturation regime as the number of detected photons approaches the number of microcells N.
The related SPAD behaviour depends further on the quenching device. Indeed, for the case of passive quenching, the extra-photon arrivals, although uncounted, extend the microcell dead-time, causing the SPAD to collapse. This is illustrated in Fig. 4.4(a): When an incident photon triggers an avalanche, the SPAD voltage V_s (blue line) is reduced below V_{bd}. The resistor R_q then recharges the junction capacitance. Now, as long as V_s exceeds V_{bd}, the SPAD can be triggered by another photon. In such case (as shown in the figure), V_s remains below the threshold voltage of the trigger circuit V_{th}, hence extending the dead time and "paralyzing" the photon detection [122]. For this reason, the PQ-SPAD, and therefore the PQ-SiPM, is said to be a paralyzable detector [116]. On the other hand, for the case of active quenching, the incoming photons during the dead-time are not counted and do not prolong the dead-time, see Fig. 4.4(b). Hence, AQ-SPADs are called non-paralyzable detectors [116]

Mathematical formulation: In contrast to the average measured photon count μ given in (4.3)), we define μ_{PQ} and μ_{AQ} respectively as the real average photon-count of a PQ- and AQ-SiPM during a bit time T. The relation between μ_{PQ} and μ for instance can be formulated based on a paralyzable-detector model adopted from nuclear particle physics instruments [122, 116], as follows:

$$\mu_{PQ} = \mu \exp(-\frac{\mu \tau_d}{TN}) \tag{4.4}$$

$$\mu_{AQ} = \frac{\mu}{1 + \frac{\mu \tau_d}{TN}}, \tag{4.5}$$

In order to illustrate these relationships, we simulated the output photon count of an SiPM versus the input optical power, P_{Rx}, for the two counting time intervals of $\Delta\mathrm{t} = 1\,\mu\mathrm{s}$ and 1 ms, assuming $N = 10,998$ and $\tau_d = 90\,\mathrm{ns}$ (the other considered SiPM parameters are presented in Table 4.2, next section). The results are presented in Fig. 4.5 which clearly shows the two operation regimes of the SiPM. During the first regime, the curve of the output photon count versus P_{Rx} exhibits a linear bahaviour until a maximum photon count (depending on $\Delta\mathrm{t}$). Above this limit, the photon count is constant for the case of AQ-SiPM whereas it drops sharply and marks the start of the saturation regime for the case of PQ-SiPM. Note that the saturation point in terms of the maximum accepted photon rate (or equivalently P_{Rx}) is constant for both counting time intervals, and is on the order of 10^{10} Photons/sec. This confirms the fact that, considering the dead-time constraint, an SPAD is practically able to detect photons at a maximum rate of $R_{\max} \approx 1/\tau_d$ [122, 123], resulting in an $R_{\max} \approx N/\tau_d$, here about 10^{10} Photons/sec, for the case of SiPM.

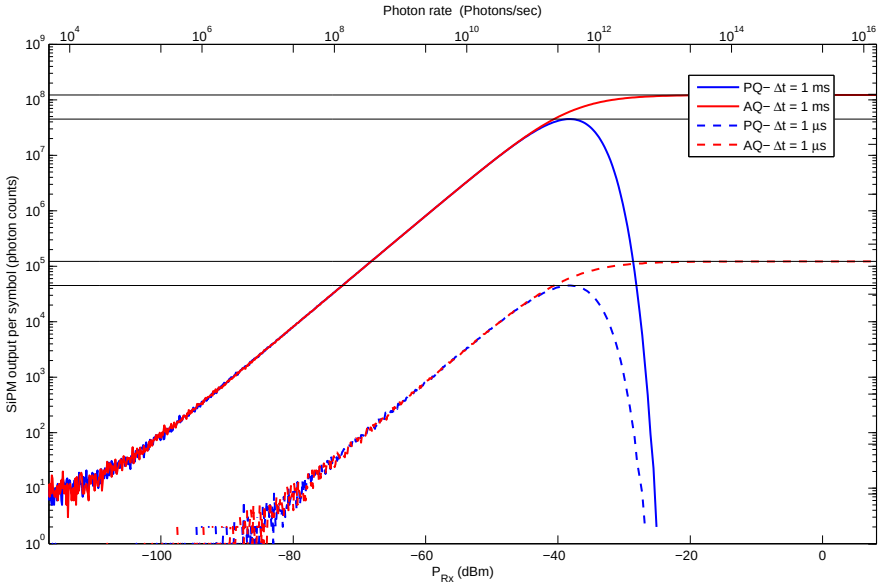

Figure 4.5: SiPM photon-count output as a function of optical received power P_{Rx} and the incoming photon flux (photon rate), for the cases of AQ (red) and PQ (blue).

4.4 Employing SiPMs in UWOC

In this Section, we investigate the interest and feasibility of employing SiPMs in UWOC applications. Considering a typical link configuration, we evaluate the performance of an SiPM-based Rx and illustrate its advantage, compared to the case of using an APD. In fact, as we explained earlier in Subsection 4.3.1, an SiPM is composed of a number of APDs biased above the breakdown voltage, whereas in the

classical APD use, the PD is biased below its breakdown voltage. We also compare the SiPM performance to that of a PMT-based Rx, reported to have equivalent quality in terms of Rx sensitivity, for instance. based on these results, we then discuss the relevance of using SiPMs in the UWOC context.

4.4.1 Main assumptions and system model

We consider a point-to-point communication link, as depicted in Fig. 4.6 with an LED-based Tx. Here, we suppose that the SiPM output is discrete and consist in photon count values, thus we do not consider time sampling of the PD output signal for the case of SiPM. Without loss of generality, we model the LED radiation pattern P_{Tx} by a generalized Lambertian model with azimuthal symmetry described by (3.3) and rewritten below:

$$P_{\text{Tx}} = P_{\text{t}} \frac{m+1}{2\pi} \cos^m(\phi) \quad [\text{W/sr}],$$

The LED is considered to emit at $\lambda = 470\,\text{nm}$ (the considered SiPM PDE exhibits its peak value in the blue region of the spectrum [106]) with a Lambertian order of $m = 45$, corresponding to $\phi_{1/2} \approx 10°$.

We conduct our study for the case of clear ocean waters, with a typical Chlorophyll concentration of $C = 0.5\,\text{mg/m}^3$ corresponding to a diffuse attenuation coefficient of $K = 0.08\,\text{m}^{-1}$. We also consider the case of coastal waters of type Jerlov 5. For this latter, given that the corresponding K value cannot be predicted using bio-optical models presented in Section 2.3.2, we performed experimental measurements in a location close to the docks of Ifremer Institute (located in La-Seyne-Sur-Mer, Toulon), in the south of France. We measured the water turbidity with a C-Star transmissometer from Wet Lab [124] and obtained a turbidity scale equal to 4 in NTU (Nephelometric Turbidity Units), and a transmittance of 65% at 475 nm. These findings confirm the water type of Jerlov 5, referring to Fig. 2.6. Also, the measured K was around $0.5\,\text{m}^{-1}$.

We model the optical power loss by an exponential decay model (see Subsection 2.3.3). This way, assuming perfect Tx-Rx alignment, the captured power P_{Rx} at the Rx is given by:

$$P_{\text{Rx}} = P_{\text{Tx}} \exp(-K\,Z) \frac{A_{\text{PD}}}{Z^2}\,, \tag{4.6}$$

where Z is the distance between the Tx and the Rx and A_{PD} is the physical area of the PD.

Concerning the Rx noise for the case of an APD and a PMT, we take into account the photo-current shot noise, arising from the input signal but reasonably neglect the shot noise arising from background radiations, assuming that our system operates in deep waters (see Section 3.6). We also take into account the thermal noise, mostly generated by the load resistor of the TZ circuitry. Note that the TZ circuitry is useless for the SiPM case and is used only for the APD and PMT cases, see the next section. Further details on Rx noise modeling for the cases of APD and PMT were given in Subsection 3.3.5.

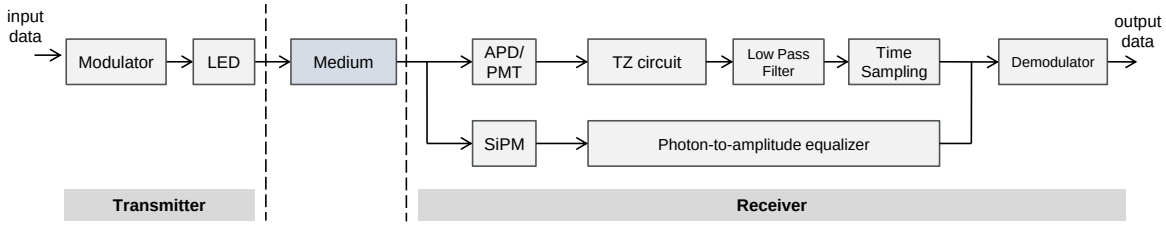

Figure 4.6: End-to-End general block diagram of the UWOC communication link.

BER analysis We consider IM/DD transmission, based uncoded NRZ OOK modulation. Let us denote by P_0 and P_1 the transmitted optical power for bits '0' and '1', respectively. Referring to (4.6) and (4.3)-(4.5), we calculate the corresponding average numbers of received photons, that we denote by μ_0 and μ_1 for off and on states, respectively. For OOK demodulation at the Rx, we define a suboptimal detection threshold μ_{th} as follows:

$$\mu_{\text{th}} = \frac{\mu_0 + \mu_1}{2}\,. \tag{4.7}$$

For instance, for the case of SiPM-based Rx, , the error probability P_{e}, can be calculated as [114]:

$$\begin{aligned} P_{\text{e}} &= \frac{1}{2}\Pr\Big(C_{\text{ph}} \leq \mu_{\text{th}} | \mu = \mu_1\Big) + \frac{1}{2}\Pr\Big(C_{\text{ph}} > \mu_{\text{th}} | \mu = \mu_0\Big) \\ &= \frac{1}{2}\Big[1 - F_{\text{c}}(\mu_{\text{th}}, \mu_0) + F_{\text{c}}(\mu_{\text{th}}, \mu_1)\Big]\,, \end{aligned} \tag{4.8}$$

where $F_{\text{c}}(x, y)$ denotes the cumulative distribution function of random variable x (here, Poisson-distributed) with parameter y.

4.4.2 Numerical results

In this section, we present some simulation results in order to study the performance of an SiPM-based Rx for UWOC links. The considered SiPM parameters are specified in Table 4.2, which correspond to the SensL B-series 30020 SiPM [121]. Here, we take the data rate $R_{\text{b}} = 1\,\text{Mbps}$, which can be readily attained using the typical off-the-shelf available LEDs. In order to make a fair comparison between SiPM, APD, and PMT, we assume that the two latter receive an equal power level to that detected by the SiPM at a given link range Z. This comes to assume that the considered APD and PMT have equal physical areas to that of SiPM. Yet, it must be noted that, whereas the physical areas of PMT and APD are almost totally photo-sensitive, the fill factor of an SiPM is typically on the order of 40%.

Let us first set the extinction ratio of OOK modulation $\text{EXT} = P_0/P_1$ to 0. We have presented the link BER performance of the cases of PQ- and AQ-SiPM, APD, and PMT as a function of Z in Fig. 4.8. To start, we have shown in Fig. 4.7 plots of the received power P_{Rx} as a function of Z for the two water types considered here.

Table 4.2: Rx parameter specification

Parameter	Value
SiPM PDE, Υ_{PDE}	0.31
SiPM area	$9\,\mathrm{mm}^2$
SiPM Dark Count Rate, f_{DCR}	6.6 MHz
SPAD dead-time, τ_{d}	90 ns
Number of SPAD in SiPM, N_{SPAD}	10998
Probability of Cross-Talk, P_{CT}	0.1
Probability of After-Pulsing, P_{AP}	0.01
APD load resistance, R_{L}	$50\,\Omega$
APD gain, G	50
APD ionization ratio, ξ	0.02

If we consider a target BER of 10^{-4}, from these results, an SiPM-based Rx achieves (for both cases of AQ and PQ detectors) a communication link span around 68 and 17 m for the cases of clear and turbid waters, respectively. The attainable link range for the APD-based Rx is limited to about 28 and 9 m only. Note that at the maximum range, for instance in clear ocean water case, P_{Rx} is around -72 dBm for the case of an SiPM-based Rx (in contrast to -50 dBm for the case of APD-based Rx) which shows the capability of SiPMs to work under very low signal levels. On the other hand, we notice that the PMT-based Rx achieves a link distance on the order of 80 and 19 m for the cases of clear and turbid waters, respectively. Thus, at equal received power, the PMT allows to increase the link range by around ten meters in clear ocean waters, but it provides equivalent performance in turbid waters, compared with SiPM-based Rx. These results confirm that the SiPM is potentially a serious challenger to PMT, taking into account its lower implementation complexity and higher operational flexibility.
We also notice from Fig. 4.8 that NLD as a result of the PD saturation, arises for the case of PQ-SiPM for $P_{\mathrm{Rx}} \geq -22$ dBm, corresponding to $Z \leq 4$ m in clear and $Z \leq 2$ m in turbid waters. So, unless for too short link distances that would be rather unlikely to happen in practice, the PQ-SiPM is not concerned by the NLD problem. Note that we do not notice this behavior for the case of an AQ-SiPM.
Note: One must note here that the BER equalling 1, observed when the PQ-SiPM is suffering from saturation, must be considered with a hindsight; In effect, when a PQ-SiPM enters the saturation phase, this corresponds in practice to the component being collapsed, and, under such conditions,it would have stopped working. Thus, this value of BER does not correspond to an actual acceptable transmission BER. Yet, we chose to keep this value here so as to considered it as an indicator of the ignition of the SiPM saturation phase.

In order to get more insight into the impact of NLD on the link performance, let us now investigate the case where EXT $\neq 0$, which is mostly the case in practice

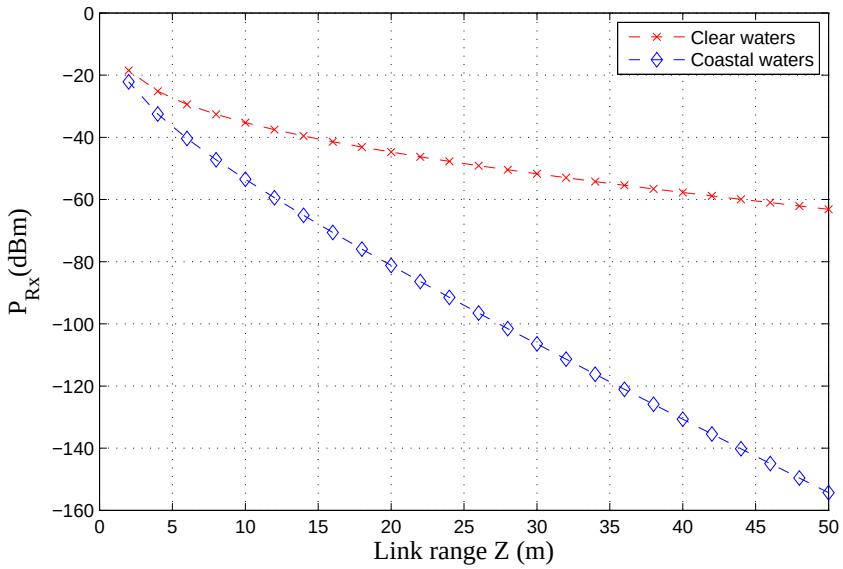

Figure 4.7: Received power P_{Rx} versus Z for the case of clear and turbid coastal ocean waters, by an SiPM-based Rx.

because we cannot switch off the LED completely at the given high data rate. As our objective is to present a comparative study between different photodetectors, for the sake of simplicity, we consider hereafter only the case of clear ocean waters. Simulation results are presented in Fig. 4.9(a) and (b) for the cases of AQ- and PQ-SiPM, respectively. We notice that the SiPM performance strongly depends on the EXT parameter. Indeed, when we increase EXT from 0 to 0.8, the maximum achievable link span for a target BER of 10^{-4} is reduced from $\sim 68\,\mathrm{m}$ to $\sim 40\,\mathrm{m}$ for both AQ- and PQ-SiPM cases. This could be expected since increasing EXT means that the power levels corresponding to bits '0' and '1' are closer to each other, resulting in a higher error probability according to (4.8). We also notice that the NLD effect is manifest at a larger Z as EXT increases, and this is also valid for the case of AQ-SiPM, although we noticed an NLD-free performance for this latter for EXT $= 0$. For instance, for EXT $= 0.8$, the NLD limitation occurs at $Z \leq 4\,\mathrm{m}$ for the case of AQ-SiPM, while this lower limit of the link span increases to about $12\,\mathrm{m}$ for the case of PQ-SiPM. We conclude that, overall, not only a relatively high EXT ratio reduces significantly the link span for a target BER, it also impacts the range of Z over which SiPM operates in the NLD-free (i.e., linear) mode.

4.4.3 Impact of solar noise on the SiPM performance

In order to complete our study of SiPM suitability for UWOCs, we investigate here the impact of solar noise on the performance of this component. To do so, we proceed as in Chapter 3, by studying the link BER variation versus the Rx operation depth D. First, we fix the link span, corresponding to a target BER of around $\sim 10^{-4}$.

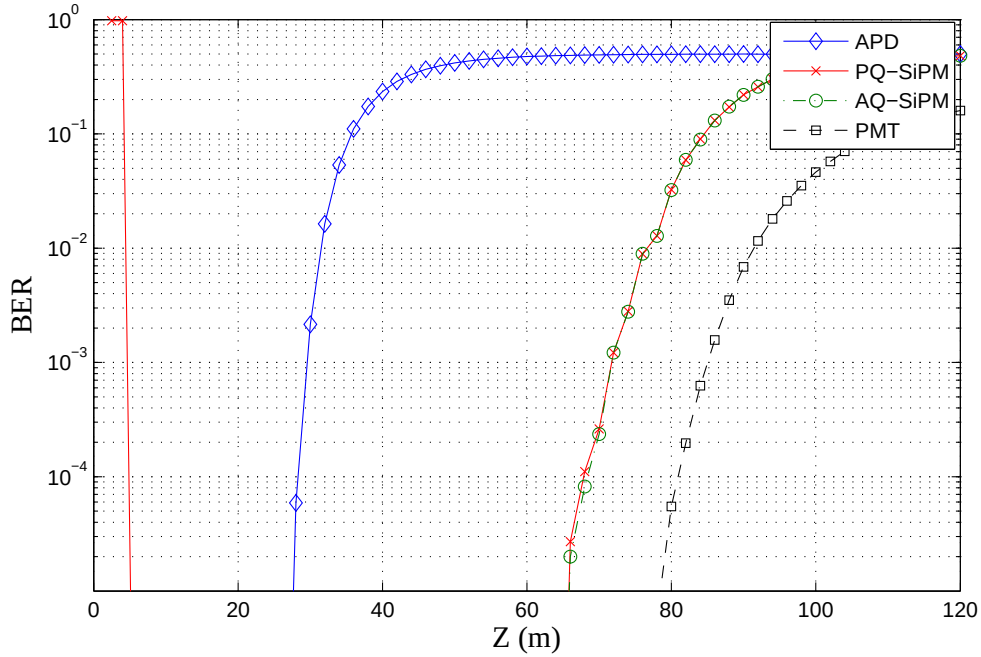

(a) Clear waters with $K = 0.08\,\mathrm{m}^{-1}$

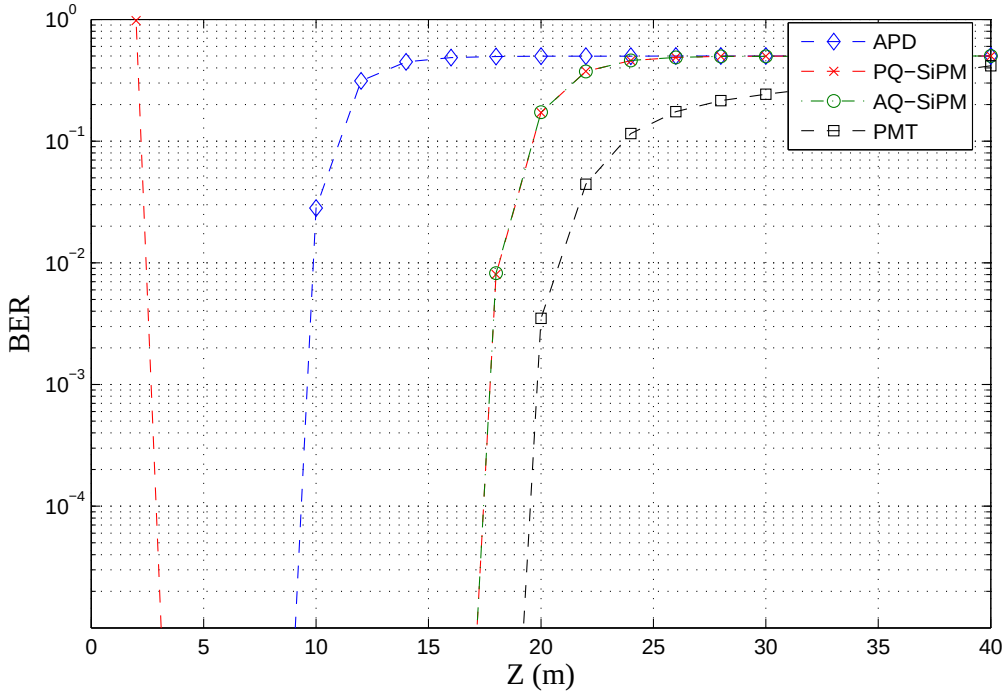

(b) Coastal waters with $K = 0.5\,\mathrm{m}^{-1}$

Figure 4.8: BER performance as a function of link distance Z for AQ- and PQ-SiPM, APD, and PMT-based receivers. $P_1 = 1\,\mathrm{W}$, EXT $= 0$, uncoded NRZ-OOK modulation, $R_\mathrm{b} = 1\,\mathrm{Mbps}$.

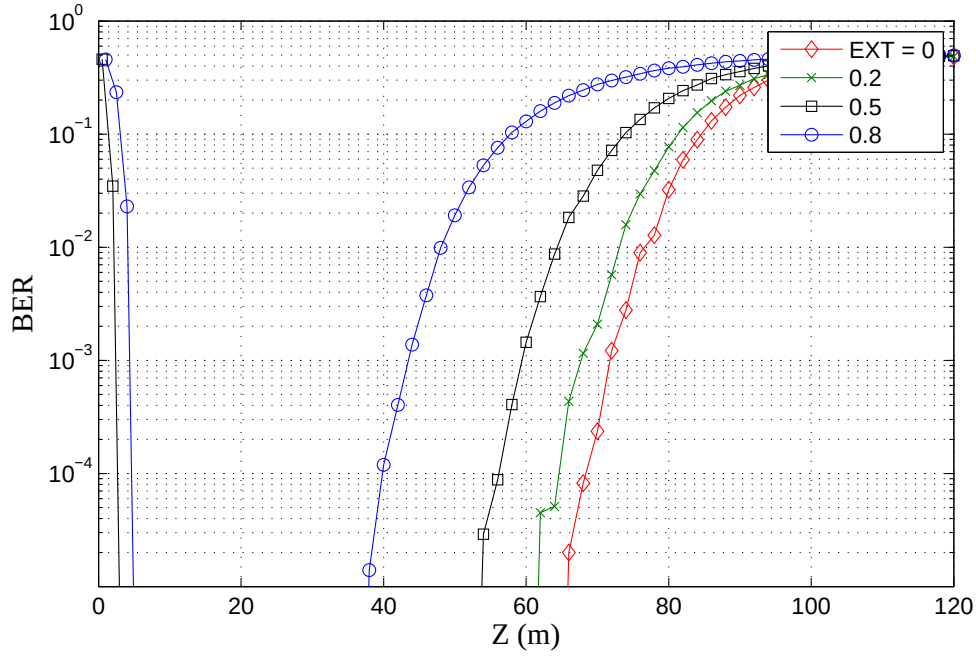

(a) AQ-SiPM

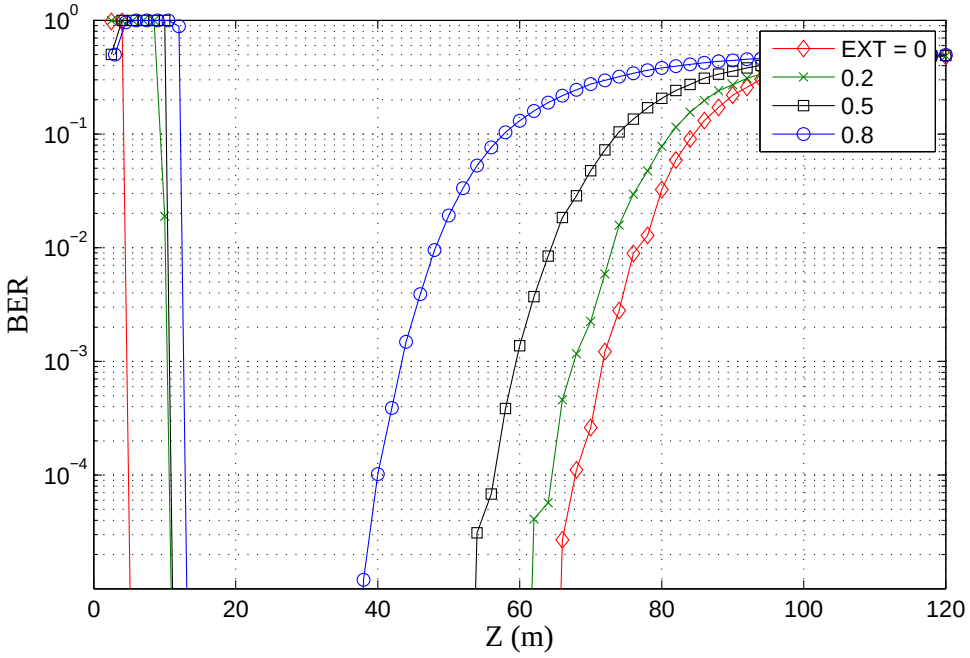

(b) PQ-SiPM

Figure 4.9: BER performance as a function of link distance Z for AQ- and PQ-SiPM-based Rx, considering different extinction ratios. $P_t = 1\,\mathrm{W}$, uncoded NRZ-OOK modulation, $R_b = 1\,\mathrm{Mbps}$, clear ocean waters.

According to Fig 4.8(a), we set the corresponding $Z = 69\,\text{m}$, and then obtain the transmission BER for different D. The simulation results are presented in Fig. 4.10. We notice that for depths smaller than 250 m, the SiPM performance is highly affected by the solar ambient light. Beyond this limit, the SiPM is not affected by the background noise where the BER converges to 10^{-4}. Compared to a PMT-based link, whose BER performance is severely degraded by solar noise for depths down to 350 m typically, we can conclude that the SiPM PD tolerates better the solar noise, while having close tolerance to this noise as an APD counterpart.

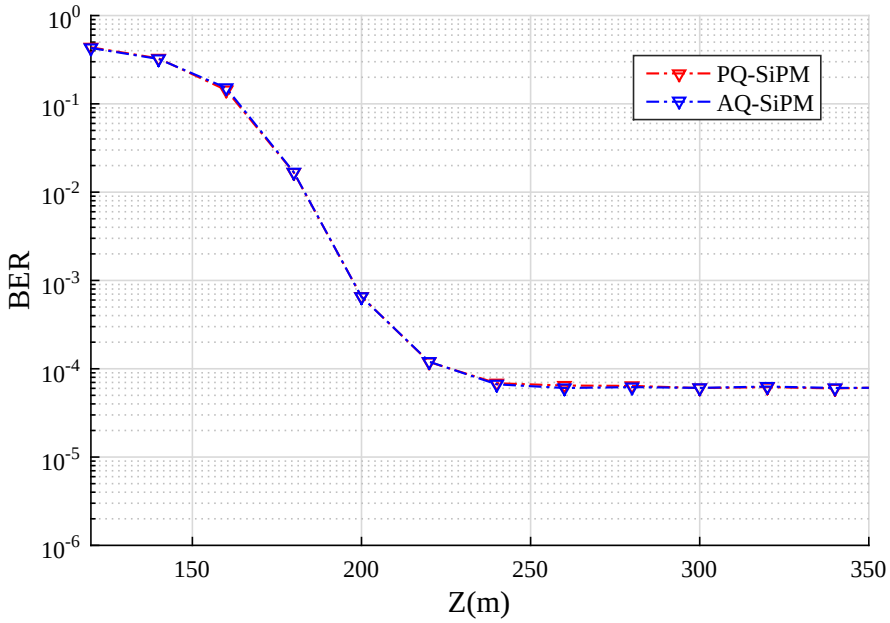

Figure 4.10: Impact of solar noise on the BER performance of an SiPM-based system.

4.5 Basic modulation techniques with SiPM

In the previous Section, we proved the suitability of using SiPMs in the context of UWOC and demonstrated that they can readily extend the transmission span compared to APDs, for instance. We investigate here the performance of basic IM/DD transmission techniques when using an SiPM at the Rx. We devote a special attention to the data transmission rate, the attainable link spans and the bandwidth (BW) requirements.

We will consider the use of a PQ-SiPM PD at the Rx. This is justified by the fact that AQ- and PQ-SiPM based Rx have an almost equivalent performance but the latter components are in general less expensive with a much larger number of microcells. At the time of writing this manuscript, the number of SPADs for commercially available AQ-SiPMs is very limited (e.g. $N = 8$ for the ID Quantique

SiPMs [120]), whereas PQ-SiPMs with quite large number of SPADs exist. As PQ-SiPM, we will consider the SensL B-series 30020 SiPM [121] with $N = 10998$ in the following.
In order to do a fair comparison of the different modulation schemes, we fix the average transmitted power P_{av} for all modulations.

4.5.1 Binary-level modulations

This category of modulation techniques conveys the information through the variation of the signal magnitude between two levels within the symbol duration. We specifically consider the OOK and pulse position modulation (PPM).

NRZ OOK We consider the simple NRZ OOK modulation as benchmark in this study. Denoting the bit rate by $R_{\text{b,OOK}}$, we consider the occupied signal bandwidth as $B_{\text{OOK}} \approx R_{\text{b,OOK}}$. Also we have:

$$P_{\text{av}} = (P_{\text{On,OOK}} + P_{\text{Off,OOK}})/2 \tag{4.9}$$

PPM PPM is the optimal slotted binary modulation in terms of energy efficiency. In addition, when a hard detection is performed at the Rx, PPM do not require dynamic threholding for optimal detection, in contrast to OOK [40]. However, this comes at the expense of an increased bandwidth requirement, thus, a lower bandwidth efficiency.
Let us consider an L-ary PPM where a symbol corresponds to $M = \log_2(L)$ bits. Each symbol duration is divided into L slots, with $(L-1)$ slots set to 'Off' state, i.e. corresponding to the transmission of an optical power of $P_{\text{Off,PPM}}$, and one slot set to 'On' state, with an optical power of $P_{\text{On,PPM}}$). The position of the 'On'-slot within the symbol duration depends on the corresponding M bits.
We assume that the emitted power level corresponding to the 'Off' is the same as for OOK and PPM. Fixing the average transmitted power P_{av} for the two modulation, we have:

$$\begin{cases} P_{\text{Off,PPM}} &= P_{\text{Off,OOK}} \\ P_{\text{On,PPM}} &= \frac{L}{2} P_{\text{On,OOK}} - \frac{(L-2)}{2} P_{\text{Off,OOK}} \end{cases} \tag{4.10}$$

The relation between the bit rate and the required bandwidth for the case of a PPM modulation is expressed as $B_{\text{PPM}} \approx L\, R_{\text{b}}/\log_2(L)$. Increasing the modulation length L results in a higher bandwidth, and thus requires a fast switching of the Tx electronic circuits. This can be very challenging due to the limited speed of the existing opto-electronic components. Furthermore, it would make the Rx slot synchronization more complex [125]. Increasing L results also in a higher PAPR according to (4.10).

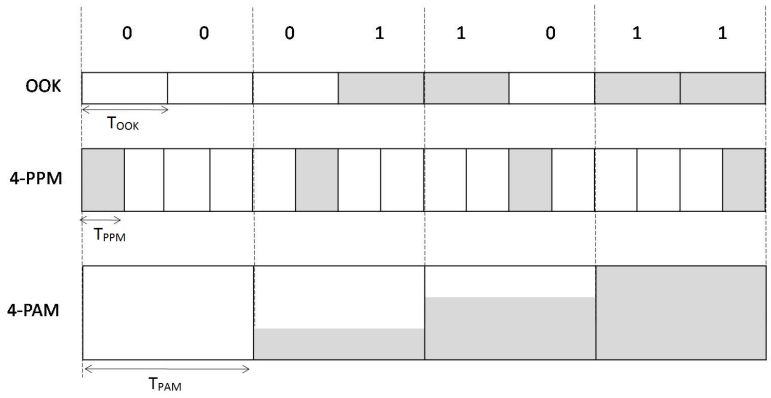

Figure 4.11: Illustration of the considered intensity modulation schemes.

4.5.2 Multilevel modulation PAM

With optical PAM, the information is conveyed on the signal intensity which takes L levels. OOK is the simpliest form with $L = 2$. L-ary PAM ($L > 2$) has the advantage of bandwidth efficiency compared to OOK and PPM, which is particularly interesting given the bandwidth limitation of typical opto-electronic components (e.g. LEDs and/or PDs). Denoting again the number of bits per symbol by $M = \log_2(L)$, the required bandwidth of PAM equals $B_{\text{PAM}} = B_{\text{OOK}}/M$. From a practical implementation point of view, to use of PAM, the Tx should be able to change the intensity level depending on the M bits being transmitted. This can be accommodated readily in the UWOC context since most of the time, a number of LEDs are used at the Tx in order to increase the Tx power, and hence the link span. PAM signaling can be realized then by switching on and off a set of LEDs.
given the fixed P_{av}, we can show that the intensity levels corresponding to L-PAM in terms of OOK intensity levels are given by:

$$P_{\text{Tx}} = P_{\text{Off,OOK}} + k\frac{(P_{\text{On,OOK}} - P_{\text{Off,OOK}})}{(L-1)}; \quad \text{for } k = 0, 1, ..., (L-1) \tag{4.11}$$

An illustrative example of OOK, L-PPM and L-PAM is shown in Fig. 4.11.

4.5.3 Comparison of modulation schemes

In order to compare the performance of OOK, L-PPM and L-PAM, we consider two different cases of fixed bit rate, R_{b}, and fixed modulation BW (corresponding to system BW limitation), where in addition to evaluate the maximum attainable range, we contrast the BW efficiency and data rate of these modulations. For the simulation results that we will present, we consider the system model presented in Section 4.4, for a PQ-SiPM-based Rx operating in clear ocean waters.

4.5.3.1 Fixed data rate transmission

Let us consider the case where the transmission data rate is fixed to $R_b = 1\,\text{Mbps}$ and compare the performance of the considered modulation schemes in terms of BERs as a function of the link span Z. Simulation results are presented in Fig. 4.12. We notice that generally PAM modulation offers smaller Z_{max} compared to PPM for a given BER. For instance, setting the target BER to 10^{-4}, the largest Z for the considered modulation schemes are equal to 52, 64, and 88 m corresponding to 4-PAM, OOK and 16-PPM, respectively. Meanwhile, the required bandwidths for these schemes equal 500 KHz, 1 MHz, and 4 MHz, respectively. A more detailed comparison is presented in Table 4.3. Thus, the gain obtained in terms of link span for PPM, comes at the expense of bandwidth efficiency.

Table 4.3: Comparison of BW requirements and transmission distance of different modulations for $R_b = 1\,\text{Mbps}$

Modulation	BW	$[Z_{min}, Z_{max}]$
OOK	1 MHz	[10, 64]
4-PAM	500 KHz	[12, 52]
8-PAM	334 KHz	[12, 42]
16-PAM	250 KHz	[13, 32]
4-PPM	2 MHz	[10, 78]
8-PPM	2.6 MHz	[12, 84]
16-PPM	4 MHz	[16, 88]

4.5.3.2 Bandwidth limited transmission

Let us now consider the case where the system bandwidth is limited to 1 MHz. Plots of simulated BER as a function Z are presented in Fig. 4.13. We again notice that PAM offers a worse performance than OOK, and the PPM achieves the largest Z_{max}. for instance, for the considered modulation schemes and for a target BER of 10^{-4}, the largest Z are equal to 46, 64, and 98 m corresponding to 4-PAM, OOK and 16-PPM respectively. Note that the corresponding transmission rates are 2 Mbps, 1 Mbps, and 250 Kbps, respectively. A detailed comparison is presented in Table 4.4. We again notice the trade off between the data rate and the maximum achievable link span. For instance, the increase of Z_{max} offered by PPM comes at the expense of a lower bit rate. On the other hand, although PAM provides a shorter transmission range, it offers a high data rate for the given bandwidth limitation of 1 MHz.

4.6 Conclusion

In this chapter, we demonstrated the feasibility of using SiPM detectors in UWOC systems. On the one hand, we showed that these PDs provide significant perfor-

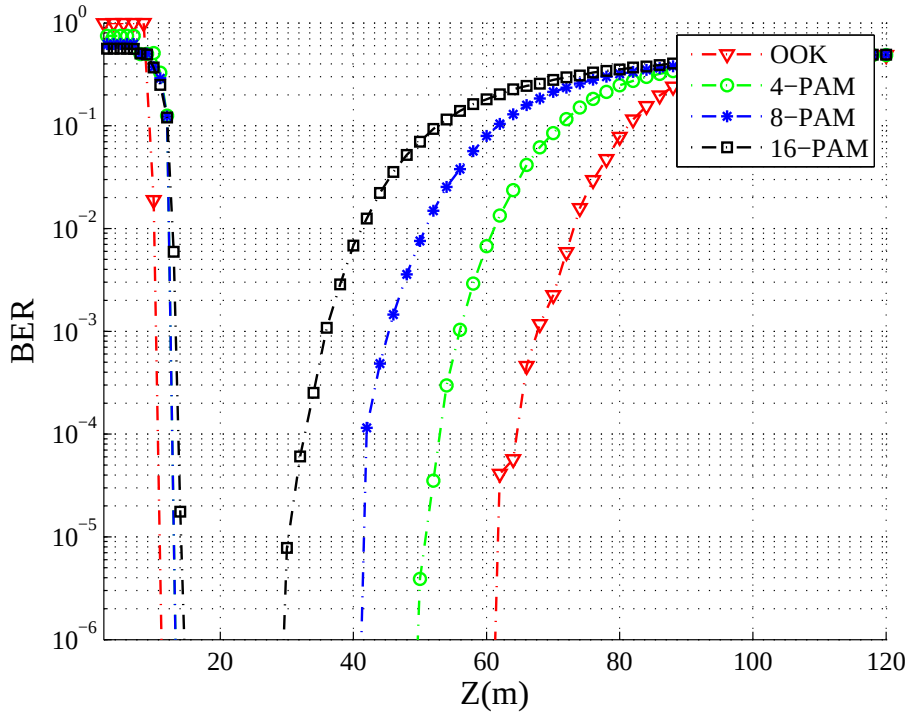

(a) PAM

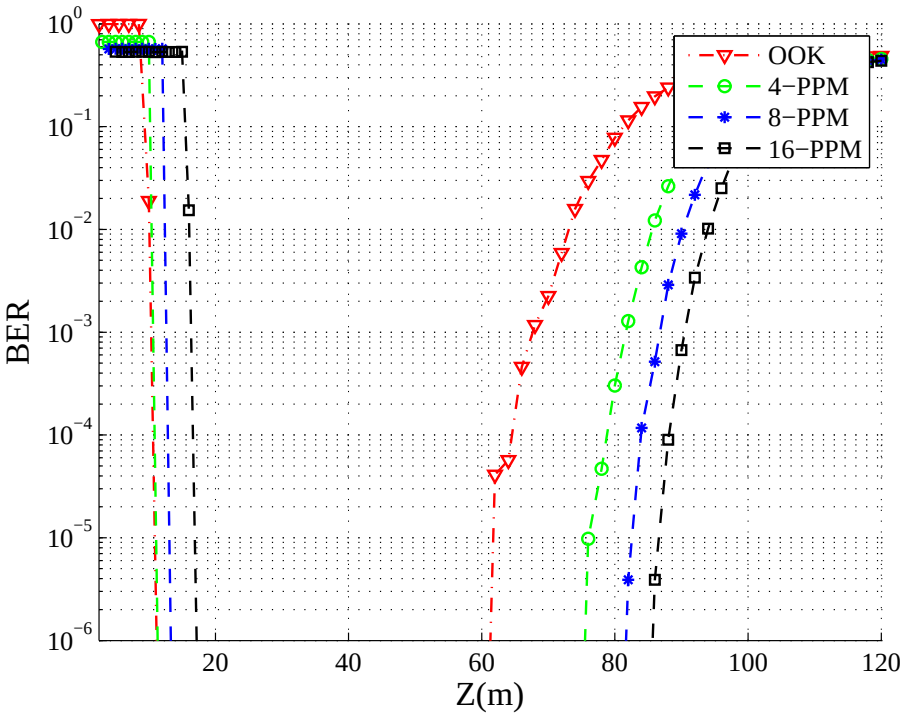

(b) PPM

Figure 4.12: BER performance as a function of link distance Z for PQ-SiPM-based Rx and different modulation schemes, for a fixed $R_{\mathrm{b}} = 1\,\mathrm{Mbps}$, $P_{\mathrm{On}} = 1\,\mathrm{W}$ and EXT = 0.2 for OOK, clear ocean waters.

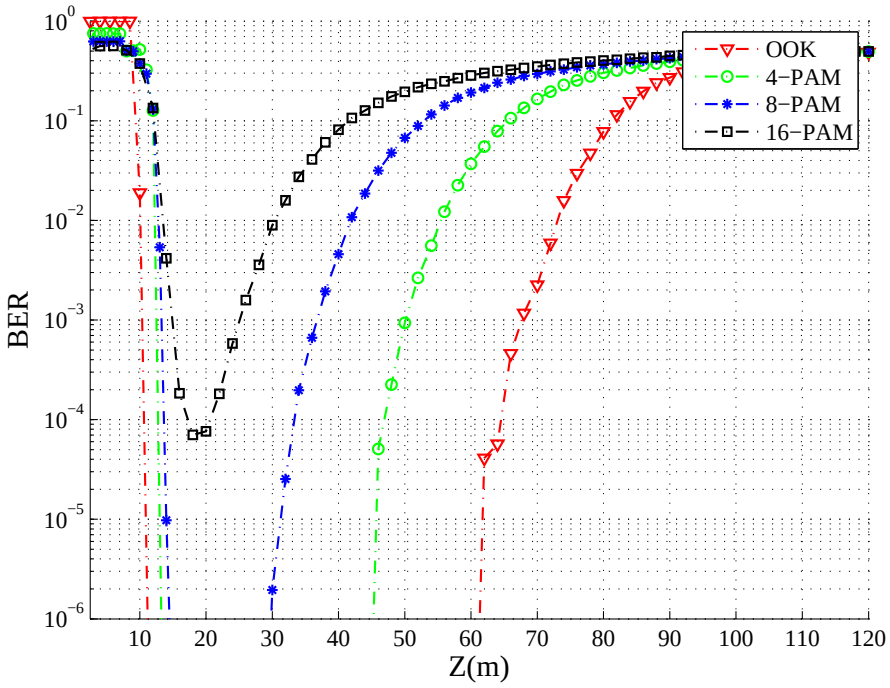

(a) PAM

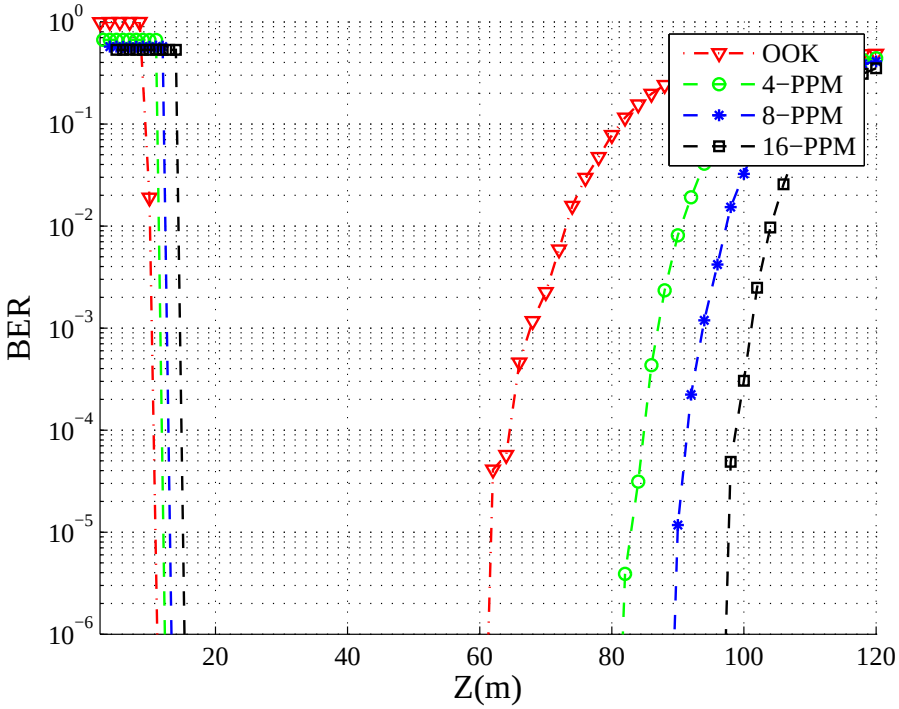

(b) PPM

Figure 4.13: BER performance as a function of link distance Z for PQ-SiPM-based Rx and different modulation schemes, for a fixed BW = 1 MHz. P_{On}= 1 W and EXT = 0.2 for OOK, clear ocean waters.

Table 4.4: Comparison of data rate and transmission range of different modulations, BW=1 MHz

Modulation	R_b	$[Z_{min}, Z_{max}]$
OOK	1 Mb/s	[10, 64]
4-PAM	2 Mb/s	[12, 46]
8-PAM	3 Mb/s	[13, 32]
16-PAM	4 Mb/s	[14, 20]
4-PPM	500 Kb/s	[11, 84]
8-PPM	337 Kb/s	[12, 90]
16-PPM	250 Kb/s	[14, 98]

mance improvement compared to the case of APDs, when working with very low signal intensity levels, e.g. for long link spans. We also showed that SiPMs provide equivalent performance to those of PMTs, adding several advantages like compactness and mechanical robustness, for instance. On the other hand, we studied the effect of non-linear distortion generated by the SiPM operation mode and showed that its impact on the link performance and range strongly depends on the LED extinction ratio. In fact, increasing the EXT parameter reduces the operation flexibility in terms of the maximum and minimum achievable link spans for a given target BER performance. Meanwhile, we showed that the limitation due to non-linear distortion occurs in very short link ranges,e.g. lower than a few meters for EXT < 0.5.

Furthermore, we investigated two basic modulation techniques of PPM and PAM, in the aim of further improving the performance of SiPM-based systems in terms of link distance and transmission data rate. We showed that a trade-off between bandwidth efficiency, and maximum achievable link span should be considered. PPM enables longer range communication links in contrast to PAM which is interesting in terms of data rate. For instance, for the system parameters we considered in this chapter, to insure BER $< 10^{-4}$, the link span can be increased to 100 m with 16-PPM compared to 40 and 60 m for 4-PAM and OOK, respectively. However, this comes at the expense of increased bandwidth of factor 4, compared to OOK for a given data rate. In other words, when BW constraint is imposed, PPM provides a quite lower data rate. There, PAM becomes an interesting alternative, yet with an energy efficiency penalty. The 4-PAM scheme appears to make a good compromise between link span an data rate.

In the next chapter, we will focus on the bandwidth constraints arising from optoelctronic components, i.e. LED and SiPM. For this, we will study the impulse responses of the aggregate channel (including the Tx, the Rx, and the aquatic channel) implicitly assumed flat up to now, and investigate its impact on the system performance. Next, we will investigate efficient signal processing techniques in the aim of further improving the transmission performance, in terms of both the

maximum achievable data rate and attainable link distance.

Chapter 5

Enabling high data-rate transmission by frequency domain equalization

Contents

5.1 Introduction

In this chapter, we investigate the bandwidth limitations arising from both the underwater optical channel, and the Tx and Rx components, and determine the scenarios where they may effectively degrade the UWOC link data rate. Indeed, even though the UWOC channel can be non-frequency selective most of the time [16], an LED has a limited operational bandwidth [126], which can result in ISI at the Rx for the case of relatively high data rates. Furthermore, an SiPM PD can impose additional limitation on the transmission bandwidth.
Although we implicitly assumed in the previous chapter a flat frequency response for the SiPMs for the considered bandwidth ranges (in the order of several MHz),

we show here that this assumption needs to be revisited. In fact, as we explain in the following, the SiPM suffers from a limited operation bandwidth, which can impose constrains on the maximum tolerable data transmission rates. This can rise critical challenges in the design of high-rate underwater communication links when employing SiPMs. After this preliminary study, we investigate the use of channel equalization in the frequency domain (FDE for frequency domain equalization), which has the advantage of lower implementation complexity, as compared to the rather classical time domain equalization. We show the improvement in the link data rate by using this promising solution.

The remainder of this chapter is organized as follows. In Section 5.2, we give a review of the channel equalization techniques. Next, in Section 5.3.2, we present the UWOC channel model and the related main assumptions. Then, FDE is presented in Section. 5.4 together with a set of simulation results. Lastly, Section. 5.5 concludes the chapter.

5.2 Literature review

5.2.1 Time domain equalization

A traditional approach to reduce ISI effect within a single carrier (SC) transmission is to perform time domain equalization (TDE) at the Rx [127]. There exist various TDE techniques with different degrees of computational complexity, ranging from optimal approaches such as MAP symbol detection, maximum likelihood (ML) sequence detection, to suboptimal linear equalization methods such as zero-forcing (ZF), and minimum mean square error (MMSE) symbol estimation, and non-linear MMSE decision feedback equalization (DFE) [128]. The main weaknesses of these techniques is their relatively high computational complexity for real-time implementation [129].

An alternative solution to face channel frequency selectivity consists in performing channel equalization in the frequency domain. A common approach consists in orthogonal frequency division multiplexing modulation (OFDM) with single-tap FDE. The OFDM technique consists on transmitting data over several closely-spaced orthogonal sub-carriers. This way, the communication channel, originally frequency selective, is divided into a set of parallel frequency non-selective channels, each one corresponding to a sub-carrier. As a consequence, channel equalization is simplified to single-tap equalization per sub-channel, which has a much lower computational complexity compared to SC-TDE couterpart [128]. However, the main drawback of the OFDM technique is its relatively high PAPR resulting from the summation of a large number of sub-carriers [129]. In the UWOC context, the high PAPR makes the transmitted signal more likely to suffer from strong non-linear distortion, in particular in the form of the so-called clipping noise, due to the limited linear operation range of the LED [130].

5.2.2 Optical OFDM

Several works have investigated so far the use of optical OFDM (O-OFDM) modulation scheme in wireless optical communications, particularly within VLCs, in the aim of overcoming the limited modulation bandwidth of the LEDs and achieving high data-rate transmission. Given that the bandwidth of an LED is typically on the order of several MHz, several recent works on VLC have reported data rates up to several hundreds of Mbps by using O-OFDM [131, 132, 133, 134]. However, compared to its conventional counterpart applied in RF transmission, the O-OFDM signal is required to be real and unipolar (positive) due to intensity modulation constrain. This imposes the signal to respect a Hermitian symmetry, so as to obtain a real inverse fast Fourier transform (IFFT) output signal. Furthermore, the signal is made positive whether by adding a DC bias current (this is referred to as DC-biased OFDM or DCO-OFDM), or by loading information only on the odd sub-carriers and clipping entirely the negative signal amplitudes after IFFT (referred to as asymmetrically clipped O-OFDM or ACO-OFDM).
The direct consequences of these constrains is a power efficiency penalty due to the added DC bias current for the case of DCO-OFDM, and an important reduction in the signal spectral efficiency, up to a factor of four for the case of ACO-OFDM (when compared to a SC unipolar modulation counterpart such as PAM) [126].

5.2.3 SC-FDE

In order to face the OFDM limitations, essentially the high PAPR and the low power efficiency, an promising alternative based on SC-FDE was proposed in [129]. This technique consists in transferring the IFFT block, undertaken at the Tx side within OFDM, toward the Rx side, where the IFFT, FDE, and FFT operations are performed successively. This way, SC-FDE avoids the generation of a transmit signal with a high PAPR, while taking advantage of the low complexity of frequency-domain channel equalization. It is worth mentioning that SC-FDE has an equivalent performance to OFDM [129], with a main virtue of simpler Tx architecture and lower PAPR. Note that, the Rx in a SC-FDE scheme, is more complex compared to the case of OFDM, the global computation complexity is completely equivalent for the two schemes. In any way, SC-FDE is highly advantageous in terms of computational complexity, compared to TDE. Here, we apply this idea of FDE to the case of optical communication links [126].
We will investigate the performance of several modulation schemes, i.e., OOK, L-ary PAM, and PPM, when associated with FDE.

5.3 Impact of limited system bandwidth on the UWOC link performance

In this section, we investigate the impact of the system bandwidth limitations on the UWOC link performance, when no channel equalization is carried out at the Rx. Considering a typical UWOC link, we start by evaluating the frequency response of the aggregate channel (i.e. including the effect of the Tx, the propagation channel, and the Rx) and the main related assumptions.

5.3.1 System model and main assumptions

Let us consider a typical UWOC link as presented in Fig. 4.6. To be consistent with the previous study in Section 4.5 (which concerned the modulation schemes employed with SiPM), we considerOOK, L-PAM and L-PPM as modulation schemes. Without loss of generality and for the sake of simplicity, we limit our study to $L = 4$ and $L = 16$ for PAM and PPM cases, respectively, given that we have a similar behavior concerning the BER performance for different L values.
In order to compare the BER performance of the different modulation schemes, we consider a constant average transmitted power P_{av} for all modulations. We consider the case where the system is operating in clear ocean waters with $K = 0.08\,\text{m}^{-1}$, and the use of an LED at the Tx and a PQ-SiPM at the Rx. The SiPM parameters are specified in Table 4.2 and the LED main parameters considered hereafter are presented in Table 5.1.

Table 5.1: LED parameters

Parameter	Value
Wavelength, λ	470 nm
HP angle	10°
Average Tx power, P_{av}	1 W
Extinction ratio, EXT	0.2

5.3.2 Frequency response of the aggregate channel

Let us denote by h_{eq} the equivalent aggregate channel impulse response, which can be expressed as follows:

$$h_{\text{eq}}(t) = h_{\text{LED}}(t) * h_{\text{ch}}(t) * h_{\text{SiPM}}(t) \tag{5.1}$$

where h_{LED}, h_{ch} and h_{SiPM} denote the impulse responses of the LED, the physical aquatic channel, and the SiPM, respectively. The operator '*' denotes the convolution operation. As explained earlier, the underwater physical channel is regarded as frequency non-selective, thus we assume $h_{\text{ch}}(t) = L_{\text{ch}}\,\delta(t)$ with L_{ch} the attenuation

factor defined in (3.2).

LED impulse response LEDs have a limited operation bandwidth and are often modelled by a first order RC LPF with a normalized impulse response of [126]:

$$h_{\mathrm{LED}}(t) = \mathrm{e}^{-2\pi f_{\mathrm{c,L}} t} \tag{5.2}$$

where $f_{\mathrm{c,L}}$ denotes the LED 3-dB cut-off frequency. The value of $f_{\mathrm{c,L}}$ is not usually specified in the LED data-sheet. Thus, we conducted a set of experimental measurements within the Ifremer Institute in order to quantify $f_{\mathrm{c,L}}$ for a blue LED of model NICHIA NSPB510AS [60]. For this, we employed a fast SiliconPD at the Rx (model OSD1-5T [135]) and measured the $f_{\mathrm{c,L}}$ as about 10 MHz.
Not that, in addition to a limited bandwidth, an LED can introduce sever non-linear distortion on the optical transmitted signal, mainly due to a limited dynamic range, which is referred to as clipping effect. This occurs if the LED is modulated outside its linear operation range. As we limit our study to the cases of 16-PPM, OOK, and 4-PAM, hereafter, we reasonably assume that the LED is operated within its linear mode and neglect any related clipping effect.

SiPM impulse response In order to study the SiPM effect on the system bandwidth, we consider the MicroSB-30035 SensL model as reference. Its impulse response is presented in [136], and reproduced in Fig. 5.1(a) [1]. In order to exploit these data for our simulations, we approximate the SiPM impulse response by a first order LPF, see (5.2). As shown in Fig. 5.1, this approximation is in accordance with the experimental data from the data sheet, for frequencies up to 100 MHz. Thus, we use this LPF approximation in the following as far as the SiPM is operated within this specific range of bandwidth. The SiPM impulse response is then considered as:

$$h_{\mathrm{SiPM}}(t) = \mathrm{e}^{-2\pi f_{\mathrm{c,S}} t}\,, \tag{5.3}$$

where $f_{\mathrm{c,S}}$ denotes the 3-dB modulation bandwidth of the SiPM which is around 2 MHz.

5.3.3 Link performance without FDE

In order to highlight the effect of the channel frequency selectivity, we first study the UWOC link performance when the data rate R_{b} is increased. Thereby, we investigate the variation of the transmission BER versus Z, for different R_{b}. The simulation results for the case of OOK, 4-PAM and 16-PPM are depicted in Figs. 5.2, 5.3, and 5.4, respectively.
We notice that, as expected, for the three modulations, the BER performance deteriorates when R_{b} increases. Consider the case of OOK modulation in Fig. 5.2.

[1] Note that the impulse response is normalized.

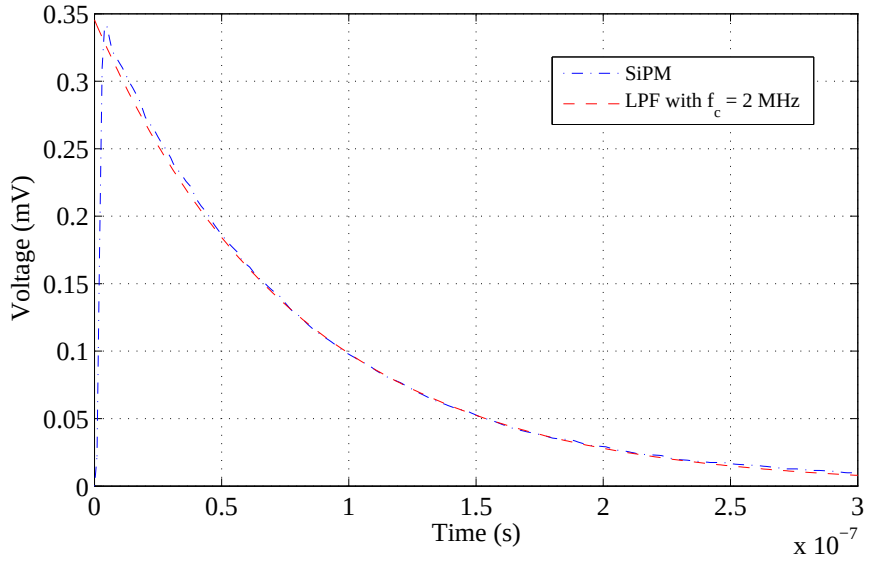

(a) Impulse response

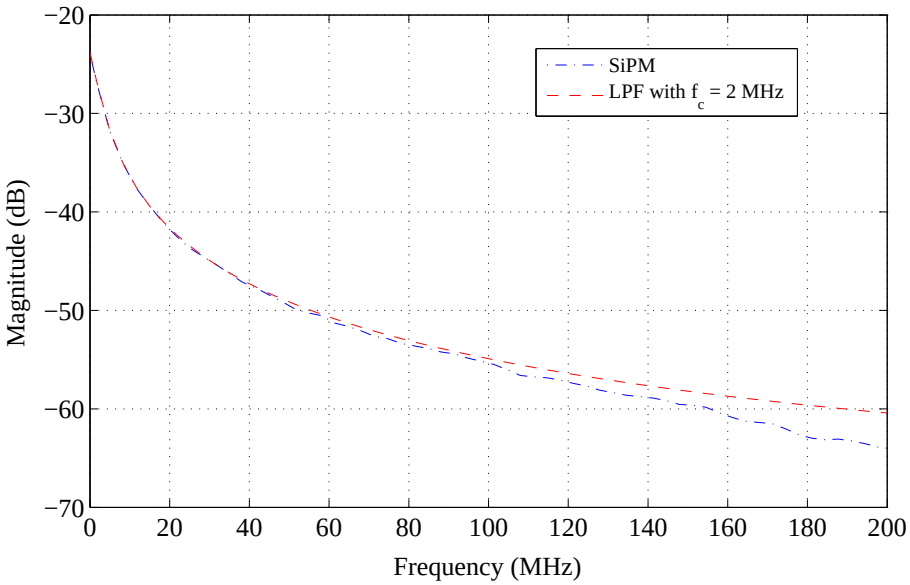

(b) Frequency response

Figure 5.1: SensL MicroSB-30035 SiPM (a) impulse response (reproduced from [136]) and (b) frequency response, and the approximation by a first order LPF.

Here, when R_b is limited to 1 Mbps, we can achieve BER $< 10^{-4}$ for a range of $Z \in [11 - 65\,\text{m}]$. This link span interval is reduced to $[15 - 41\,\text{m}]$ when operating at $R_b = 8$ Mbps, and it gets even more restricted, i.e., $[19 - 31\,\text{m}]$ at $R_b = 14$ Mbps. For $R_b > 16$ Mbps, the link performance is severely affected, resulting in BER $> 10^{-2}$.

For the case of 4-PAM, we observe the same behavior as for OOK. Indeed, increasing R_b from 1 to 4 Mbps involves a decrease of the link range interval corresponding to a BER $< 10^{-4}$, from $Z \in [10 - 54\,\text{m}]$ to $Z \in [10 - 42\,\text{m}]$. Meanwhile, we notice that 4-PAM is more sensitive to the data rate variation than OOK. Indeed, for $R_b \geq 12$ Mbps, 4-PAM is unable to establish a link with BER lower than 10^{-4}, whereas, as noticed above, OOK can tolerate data rates up to 14 Mbps. This can be explained by the fact that the 4-PAM performance is more considerably affected by ISI than OOK.

Similarly, the 16-PPM BER performance deteriorates when R_b increases. However, 16-PPM is more affected by ISI, compared to 4-PAM or OOK. Indeed, starting from $R_b = 10$ Mbps, the BER exceeds the 10^{-4} limit for all considered link ranges Z. This could be predicted since 16-PPM requires four times more bandwidth than OOK and eight times more bandwidth than 4-PAM, for a given R_b. In other words, having much narrower time slots, it is more considerably affected by the channel frequency selectivity.

In order to get more insight into the effect of the channel frequency selectivity, and to better compare the performance of the considered modulation schemes, we present here a study of BER versus R_b for a fixed link range of $Z = 40$ m. Note that the selected value of Z is arbitrary and serves as an illustrative example.
The simulation results presented in Fig. 5.5 confirm the observation made earlier: The transmission system based on 16-PPM achieves the worst BER when the data rate increases, compared to 4-PAM and OOK. In fact, the maximum tolerable R_b to achieve BER $< 10^{-4}$ over 40 m, is equal to 5, 6, and 11 Mbps for the case of 16-PPM, 4-PAM and OOK, respectively. This can be explained by the fact that the channel introduces more sever ISI for the case of 16-PPM, for instance, compared to 4-PAM.

5.4 Frequency domain equalization

5.4.1 SC-FDE overview

Figure 5.6 shows the block diagram of the UWOC link when FDE is performed at the Rx. Information bits to be transmitted are first mapped according the modulation scheme. They are next grouped by blocks of length N_{fft} which corresponds to the FFT size. Then a cyclic prefix (CP) of length M is introduced at the beginning of each block. It consists in a duplicate of the M last symbols of each block. The CP forms a guard interval between the successive blocks in the purpose of preventing

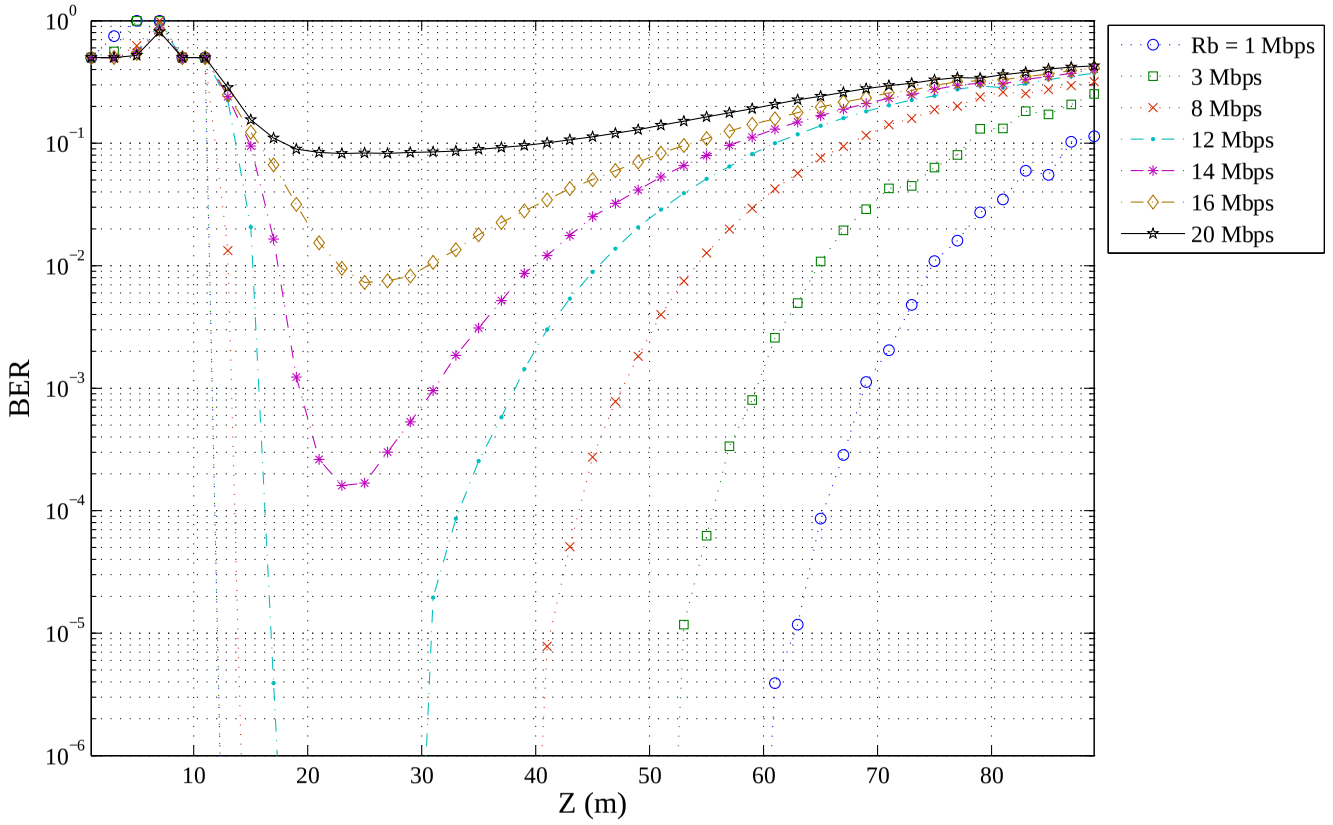

Figure 5.2: BER performance as a function of link range Z of a PQ-SiPM-based Rx with uncoded NRZ-OOK modulation, and for different data rates. System operating in clear ocean waters with $K = 0.08\,\mathrm{m}^{-1}$, $P_1 = 1\,\mathrm{W}$, EXT $= 0.2$.

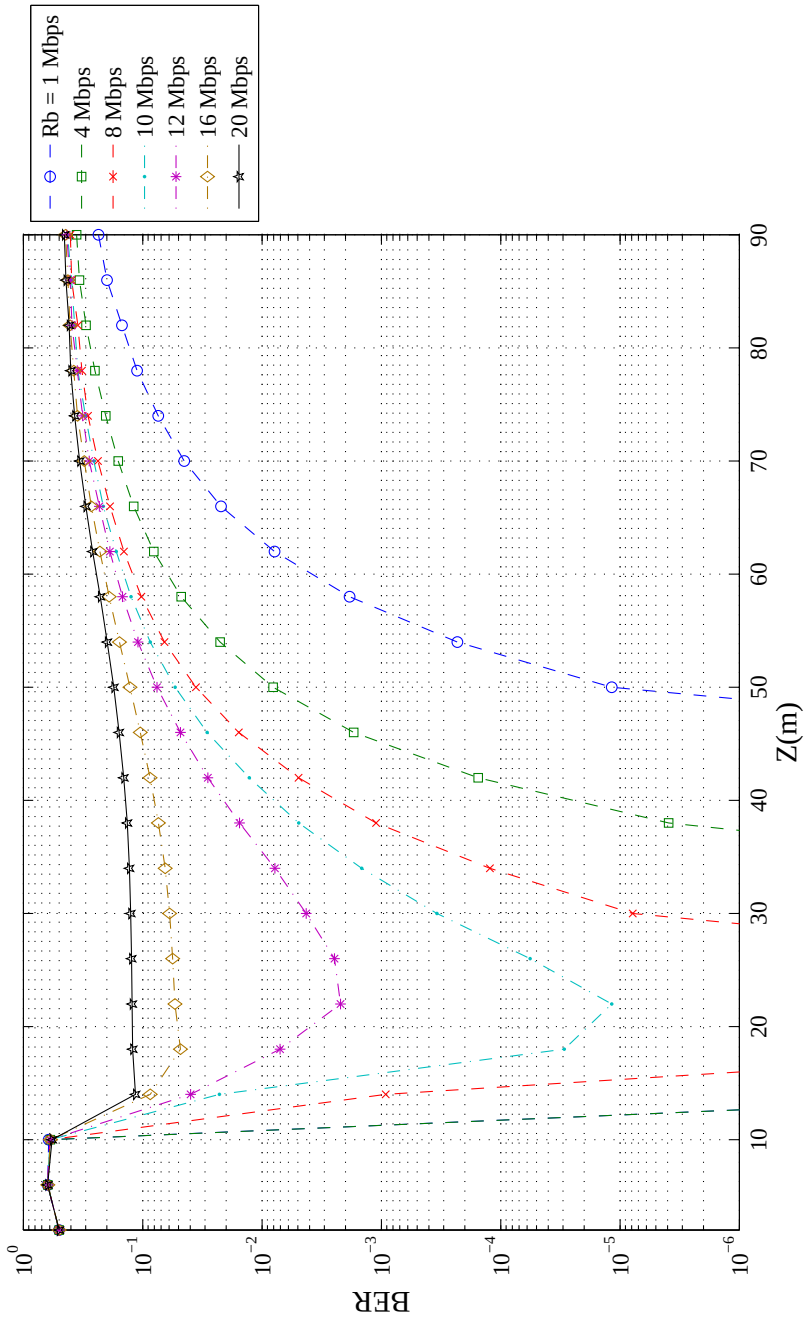

Figure 5.3: BER performance as a function of link distance Z of a PQ-SiPM-based Rx with uncoded 4-PAM modulation, and for different data rates. System operating in clear ocean waters with $K = 0.08\,\mathrm{m}^{-1}$, $P_{\mathrm{On,\,OOK}} = 1\,\mathrm{W}$, EXT $= 0.2$.

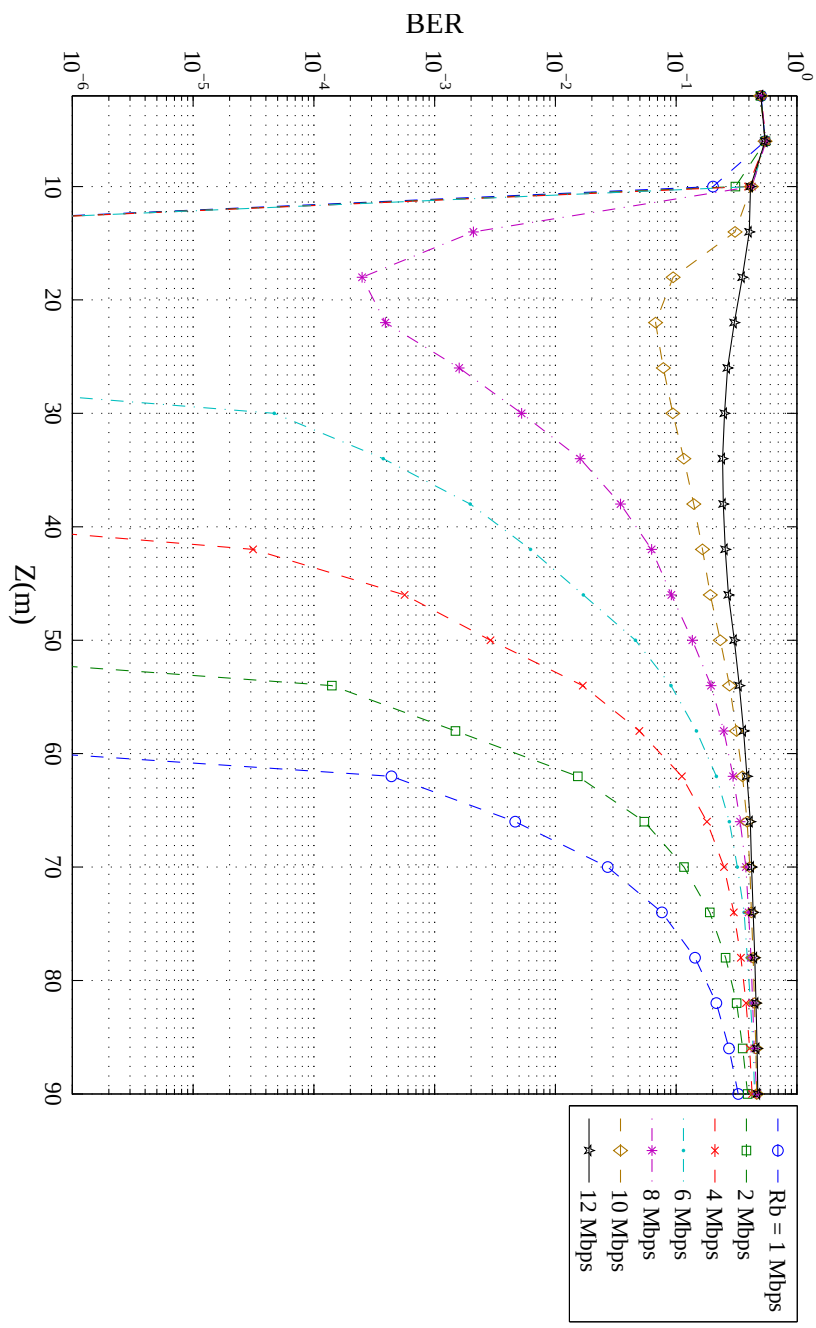

Figure 5.4: BER performance as a function of link distance Z of a PQ-SiPM-based Rx with uncoded 16-PPM modulation, and for different data rates. System operating in clear ocean waters with $K = 0.08\,\mathrm{m}^{-1}$.

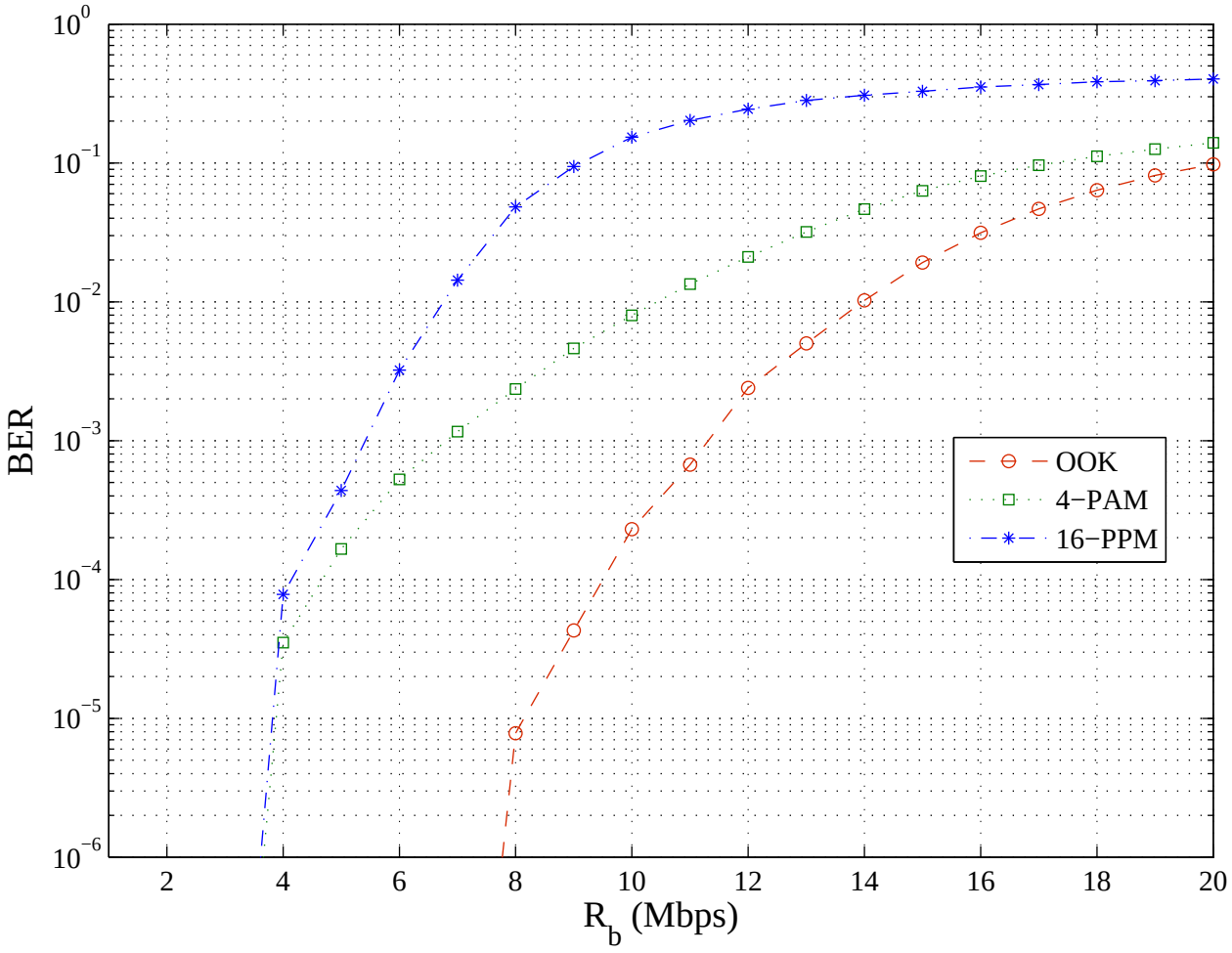

Figure 5.5: BER performance as a function of bit rate R_b of a PQ-SiPM-based Rx with uncoded OOK, 4-PAM and 16-PPM modulations. $Z = 40\,\mathrm{m}$, system operating in clear ocean waters with $K = 0.08\,\mathrm{m}^{-1}$, EXT =0.2 for OOK and 16-PPM.

inter-block interference. Furthermore, it allows circular convolution, as the block of symbols may be regarded as periodic with period M [129]. After pulse shaping, parallel to serial (P/S) and digital to analogue (D/A) operations, the transmitted signal can be written as follows:

$$s(t) = \sum_{i=-\infty}^{\infty} a(i)\, g(t - nT) * h_{\mathrm{LED}}(t) \tag{5.4}$$

where $a(i)$ denotes the transmitted optical power level corresponding to the i^{th} symbol (or slot for the case of PPM modulation), and $g(t)$ the shaping filter impulse response. Here we consider $g(t)$ as having a rectangular shape, for the sake of simplicity.
At the Rx side, after photo-detection and prior to time-sampling (here it is implicit given that the SiPM output is assumed to be discrete time), the signal can be written as follows:

$$\begin{aligned} r(t) &= \sum_{i=-\infty}^{\infty} b(i)\, g(t - nT) * h_{\mathrm{LED}}(t) * h_{\mathrm{ch}}(t) * h_{\mathrm{SiPM}}(t) \\ &= \sum_{i=-\infty}^{\infty} b(i)\, g(t - nT) * h_{\mathrm{eq}}(t) \end{aligned} \tag{5.5}$$

Here, $b(i)$ denotes the number of photons counted by SiPM, corresponding to the Tx power level $a(i)$. The factor $b(i)$ includes a noise component, introduced by SiPM photon-count statistics, see Section 4.3.4.

After discarding the CP, a channel equalization is performed in the frequency domain so as to cancel the channel effect. We specifically conduct a zero forcing (ZF) equalization, which applies the inverse of the channel frequency response $1/H_{\mathrm{eq}}(\omega)$ to the received signal where $H_{\mathrm{eq}}(\omega)$ is the transfer function of $h_{\mathrm{eq}}[n]$. This operation is done by performing FFT and IFFT processing. The ZF equalizer considered in this work offers the advantage of low complexity.

Notice that, for relatively large R_{b} (i.e. signal bandwidths) , a correspondingly large enough FFT size should be used in order to satisfy the condition of almost flat sub-channels (after IFFT). Also, the CP length should be set carefully, depending on the aggregate channel delay spread and R_{b}. In the simulation we present here, we use $N_{\mathrm{fft}} = 256$ and CP $= 20$, which are suitable for a typical data rate of 10 Mbps and the already presented components, i.e., LED and SiPM.

5.4.2 Preliminary study of the interest of FDE

In this section, we present a preliminary study to show the interest of employing FDE in the considered UWOC link. We fix the link range Z, and simulate and compare the BER performance as a function the data rate, for both cases where FDE is or not performed. The simulation results are presented in Figs. 5.7, 5.8, and 5.9, for the cases of OOK, 4-PAM, and 16-PPM, respectively.

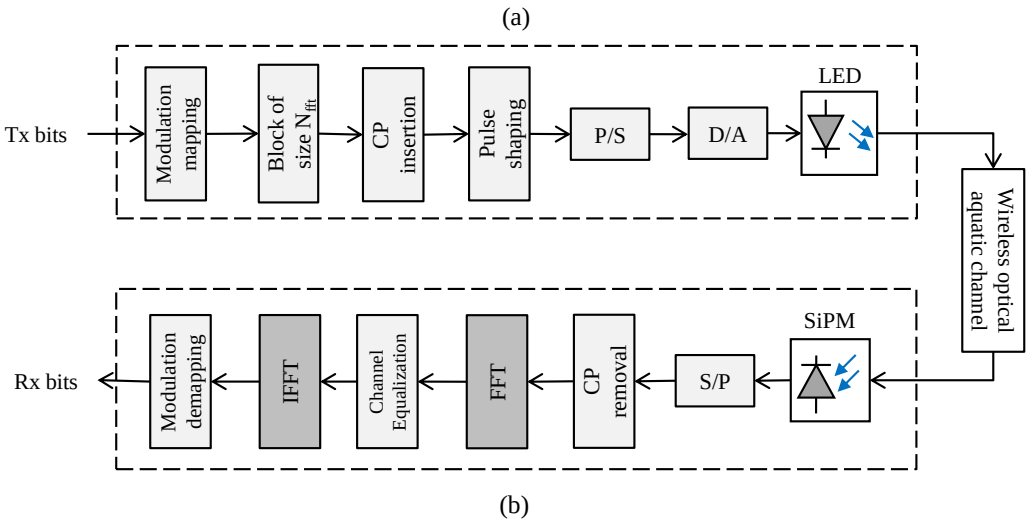

Figure 5.6: Block diagram of an UWOC (a) transmitter and (b) receiver for an FDE-based transmission.

We set $Z = 40\,\text{m}$ for the cases of OOK and 16-PPM, similarly to the study presented earlier in Section 5.3.3. For the case of 4-PAM, we choose $Z = 30\,\text{m}$ because we noticed that it allows a more clear distinction between the two cases.

We notice that the FDE technique allows a significant increase of the maximum achievable data rates at a given target BER (e.g. around 10^{-4}) for all modulation schemes. In fact, when FDE is not performed, the maximum achievable data rate (corresponding to BER $< 10^{-4}$), is on the order of 9 Mbps for the cases of OOK and 4-PAM, and 4 Mbps for 16-PPM. When FDE is employed, these boundaries increase to 16 Mbps for OOK and 4-PAM, and to 8 Mbps for 16-PPM. This shows that using FDE enables us to increase the transmission rate beyond the limitation imposed by LED or SiPM bandwidths.

More specifically, concerning SiPM, we showed that by using FDE at the Rx we can benefit from the high sensitivity offered by SiPM while overcoming its bandwidth limitations, i.e., ensuring high rate data transmission. Focusing on this, after demonstrating the impact of the FDE technique on the system performance enhancement, we present hereafter a more complete performance study in terms of maximum and minimum achievable link ranges, as well as the maximum tolerated bit rates, that can be achieved with an SiPM-based Rx.

5.4.3 Investigating the maximum achievable R_b and Z with FDE

In the previous section, we considered an arbitrary value of Z, in the aim of highlighting the interest of employing FDE and demonstrating its interest in increasing the maximum achievable data rate. In this section, we provide a more exhaustive

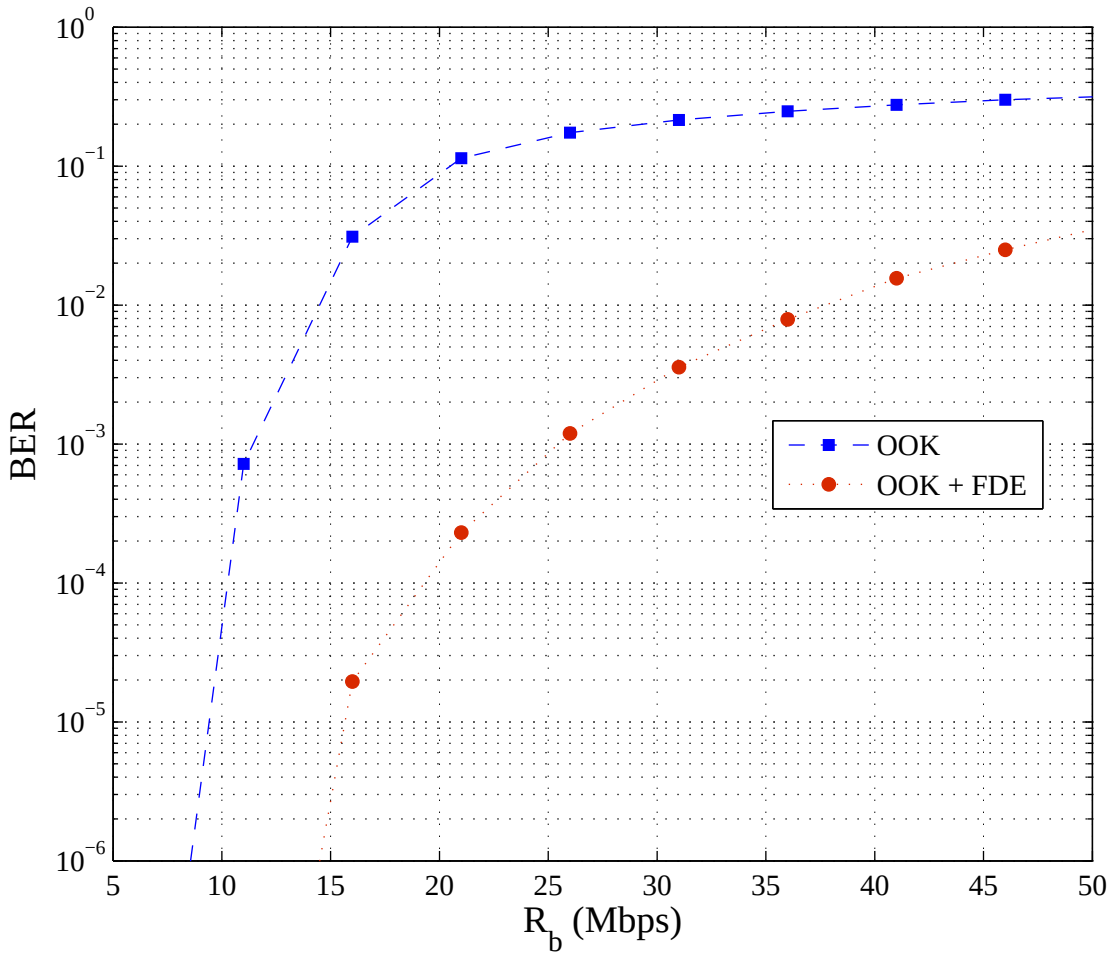

Figure 5.7: Comparing BER performance as a function of bit rate R_{b} with and without FDE, for the case of an uncoded OOK modulation. PQ-SiPM-based Rx, $Z = 40\,\mathrm{m}$, system operating in clear ocean waters with $K = 0.08\,\mathrm{m}^{-1}$, $P_{\mathrm{On}} = 1\,\mathrm{W}$, EXT $= 0.2$.

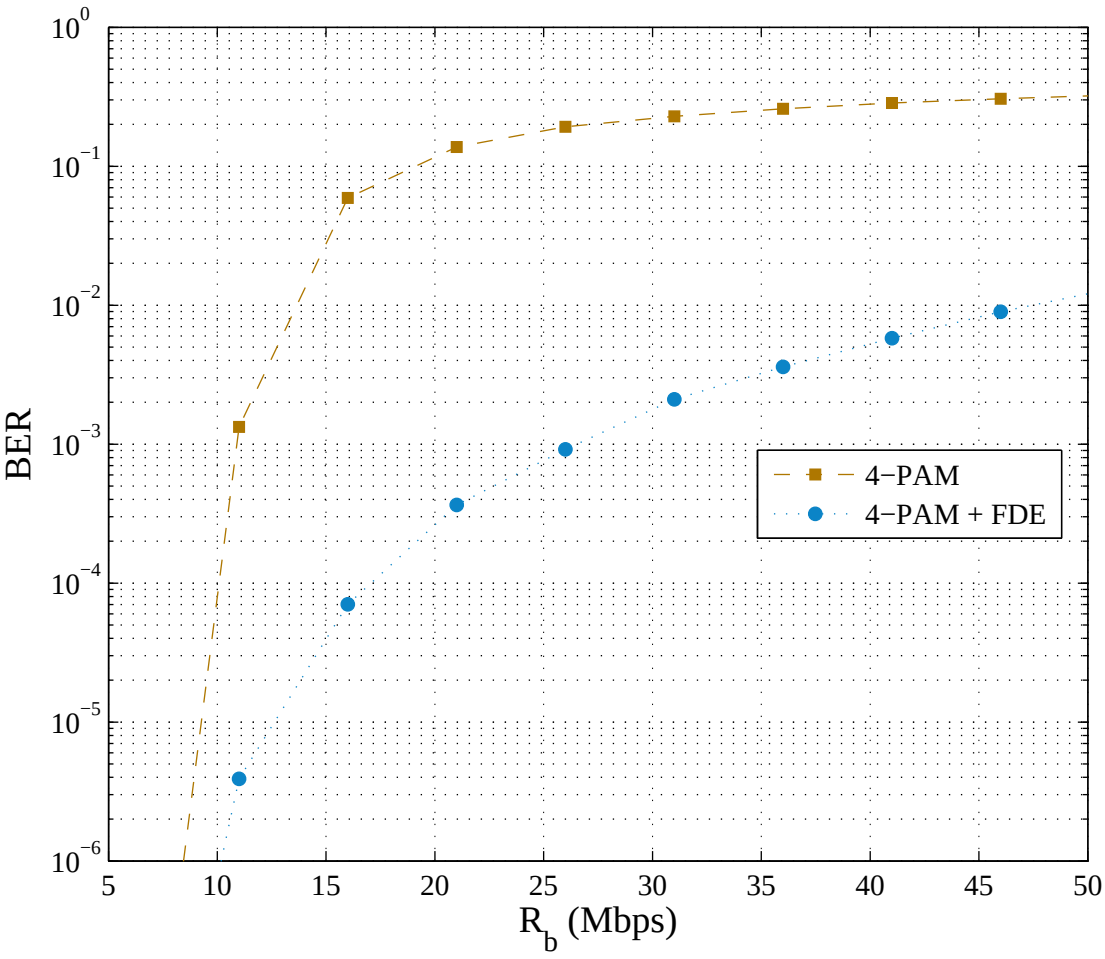

Figure 5.8: Comparing BER performance as a function of bit rate R_b with and without FDE at the Rx, for the case of an uncoded 4-PAM modulation. PQ-SiPM-based Rx, $Z = 30\,\mathrm{m}$, system operating in clear ocean waters with $K = 0.08\,\mathrm{m}^{-1}$.

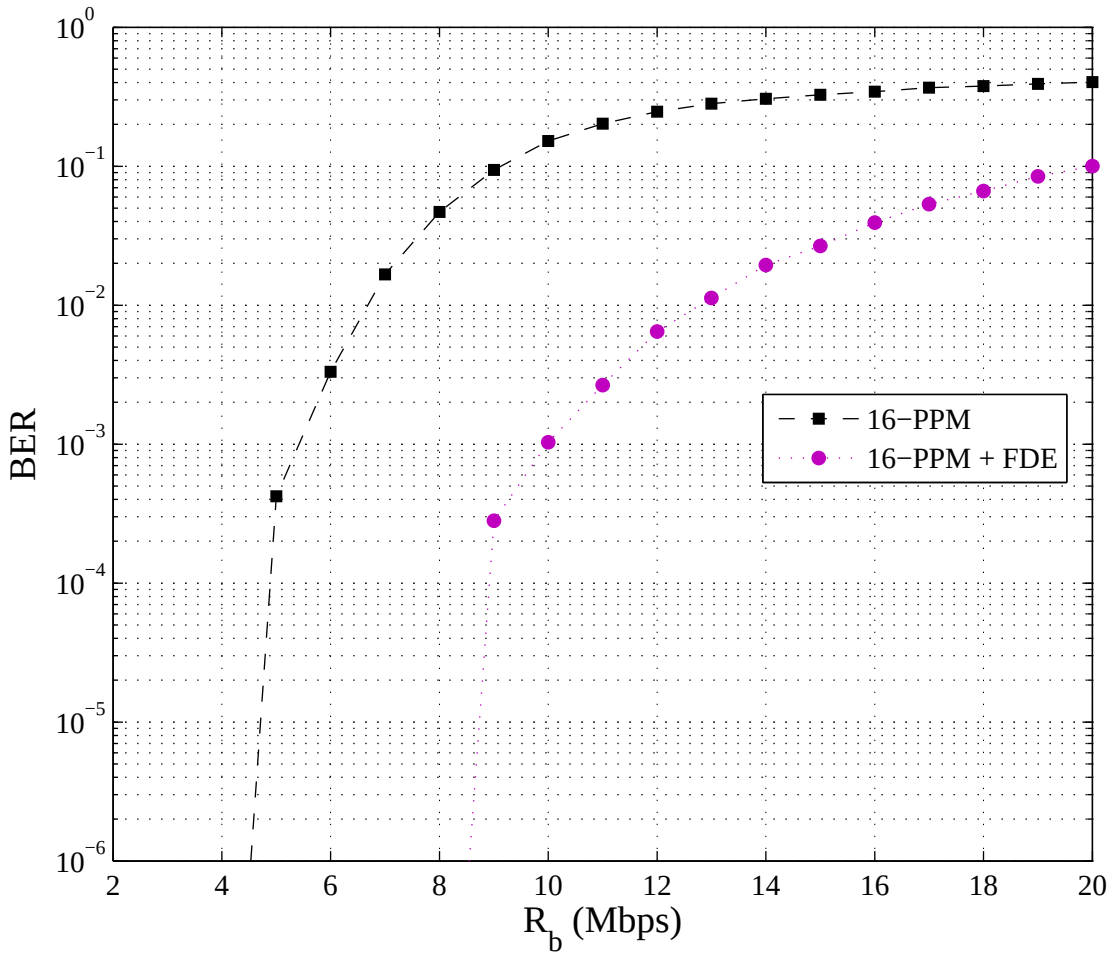

Figure 5.9: Comparing BER performance as a function of bit rate R_b with and without FDE, for the case of an uncoded 16-PPM modulation. PQ-SiPM-based Rx, $Z = 40\,\mathrm{m}$, system operating in clear ocean waters with $K = 0.08\,\mathrm{m}^{-1}$.

and complete study of the performance of an SiPM-based UWOC link when FDE is employed at the Rx.

5.4.3.1 Simulation algorithm

Considering a target BER of $\approx 10^{-4}$, we determine for a given R_b the maximum and the minimum achievable link ranges (denoted by Z_max and Z_min, respectively) where SiPM is operating within its linear mode. We also determine the maximum tolerated data rate $R_\mathrm{b,max}$.
The values of Z_max, Z_min, and $R_\mathrm{b,max}$ are determined according to the following algorithm:

Algorithm 1 Determine the boundaries of Z and R_b for BER $< 10^{-4}$

Data: R_b = [1,2,...,100] Mbps Z = [90, 88, ..., 1] m
Result: Z_min, Z_max and $R_\mathrm{b,max}$
for *each value of* R_b **do**
  for *each value of* Z **do**
    Compute the BER at Z and R_b
    if *BER* $< 10^{-4}$ *and SiPM did not saturate* **then**
      $Z_\mathrm{max} = Z$;
    else if *BER* $> 10^{-4}$ *and SiPM did saturate* **then**
      $Z_\mathrm{min} = Z$
      stop the Z loop
    end
  end
  if *BER* $> 10^{-4}$ *at* R_b *for all* Z **then**
    $R_\mathrm{b,max} = R_\mathrm{b}$
    stop the R_b loop
  end
end

5.4.3.2 Numerical results

The simulation results are presented in Figs. 5.10, 5.11, and 5.12, for the cases of OOK, 4-PAM, and 16-PPM based transmissions, respectively. We have plotted Z_max and Z_min versus R_b, for both cases where FDE is or not employed. We notice two main effects of FDE:

1. Increasing the tolerable data rate:
For a given link distance Z, applying FDE allows to considerably increase the maximum tolerable R_b. For instance, let us consider the case where $Z = 30$ m. Without FDE, for OOK, 4-PAM, and 16-PPM modulations, the maximum tolerable R_b is around 12, 9, and 6 Mbps, respectively. These values increase to about 39, 15, and 15 Mbps with FDE, respectively. This is further highlighted in Table 5.2, where we have presented the maximum achievable R_b.

We also notice that for a given Z, the impact of the channel equalization is more important for the case of 16-PPM, compared to OOK or 4-PAM counterparts. This was expected, knowing that this modulation scheme is the most affected by the bandwidth penalty.

Table 5.2: Maximum tolerable R_{b} for a PQ-SiPM-based UWOC link, for BER $< 10^{-4}$

	OOK	**4-PAM**	**16-PPM**
$R_{\mathrm{b,max}}$ without FDE	13 Mbps	9 Mbps	7 Mbps
$R_{\mathrm{b,max}}$ with FDE	69 Mbps	47 Mbps	29 Mbps

2. Increasing the operational distance range $[Z_{\mathbf{min}} - Z_{\mathbf{max}}]$:
We notice that at equal R_{b}, the FDE technique allows to expend the interval $[Z_{\mathrm{min}} - Z_{\mathrm{max}}]$. For instance, for OOK modulation and at $R_{\mathrm{b}} = 13$ Mbps, a BER of 10^{-4} can be ensured for $Z \in [18 - 29]$ when FDE is not employed. This interval is enlarged to $[13 - 43]$ with the use of FDE. This makes the transmission a bit less sensitive to SiPM saturation, since Z_{min} is reduced, and also allows to establish longer links, given that Z_{max} is increased by more than 10 meters. The same is noticed for the case of 4-PAM and 16-PPM. These findings further highlight the advantage of employing FDE in the UWOC context.

Further comments on the curves' shape:
Regarding the simulation results, we notice that the value of Z_{min} is almost constant for all considered values of R_{b}. This is justified by the fact that, by definition, Z_{min} corresponds to the link distance where the SiPM is about to enter the saturation phase, while this process depends only on the properties of the SiPM and the received power level (which directly depends on Z), and has no dependence on the data rate. On the other hand, we notice that the value of Z_{max} decreases as R_{b} increases. This can be explained by the fact that the SiPM performance (here in terms of BER) depends on the number of photons counted during a the time interval $T = 1/R_{\mathrm{b}}$, where the mean value of photon count is proportional to $P_{\mathrm{Rx}}\,T$, see (4.3). Thus, increasing R_{b} comes to decreasing the time interval over which the SiPM counts photons. Thus, in order to have the photon count needed for a given BER performance, the level of P_{Rx} must be increased, which comes to decreasing Z (remember from (4.6) that P_{Rx} is proportional to $1/Z^2$).

All the above results and discussions reveal the interest of using FDE in enhancing an SiPM-based UWOC link performance, both in terms of tolerable data rate and link distance margin within its linear operation mode.

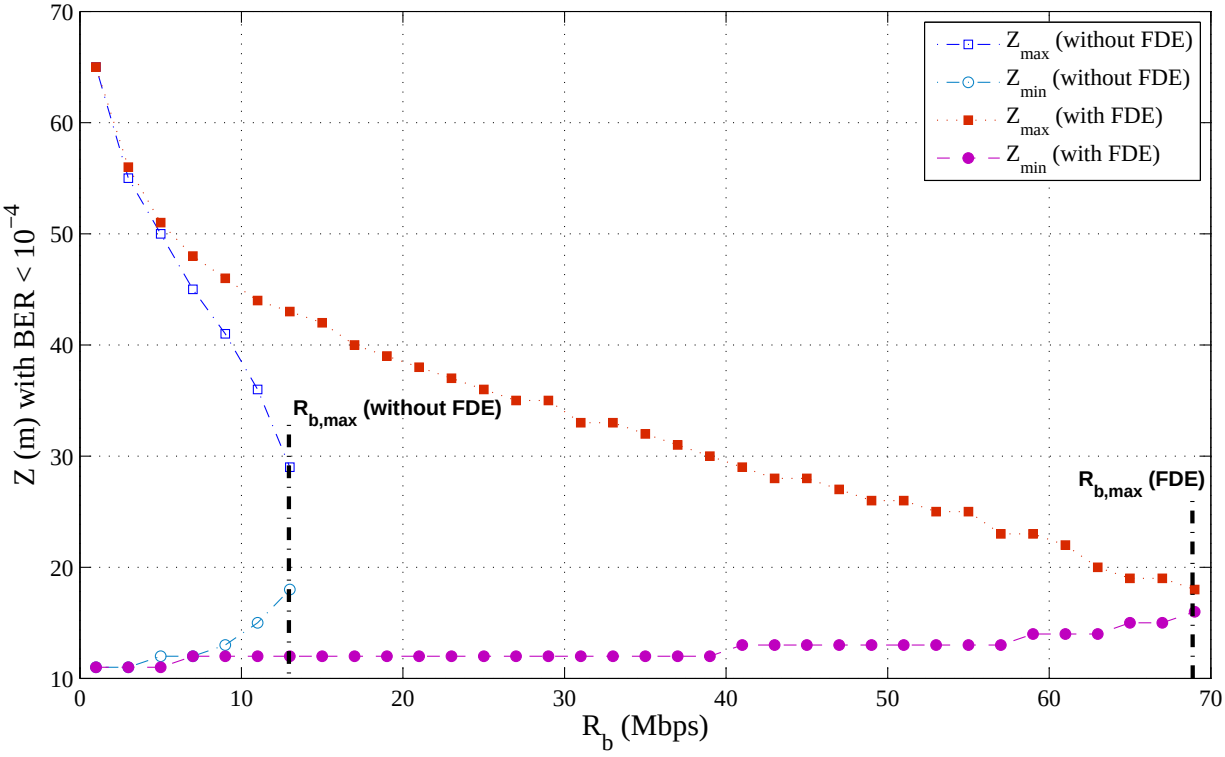

Figure 5.10: Maximum and minimum achievable link distance Z satisfying BER $< 10^{-4}$ versus data rate R_b. Uncoded OOK modulation, PQ-SiPM-based Rx, system operating in clear ocean waters with $K = 0.08\,\mathrm{m}^{-1}$.

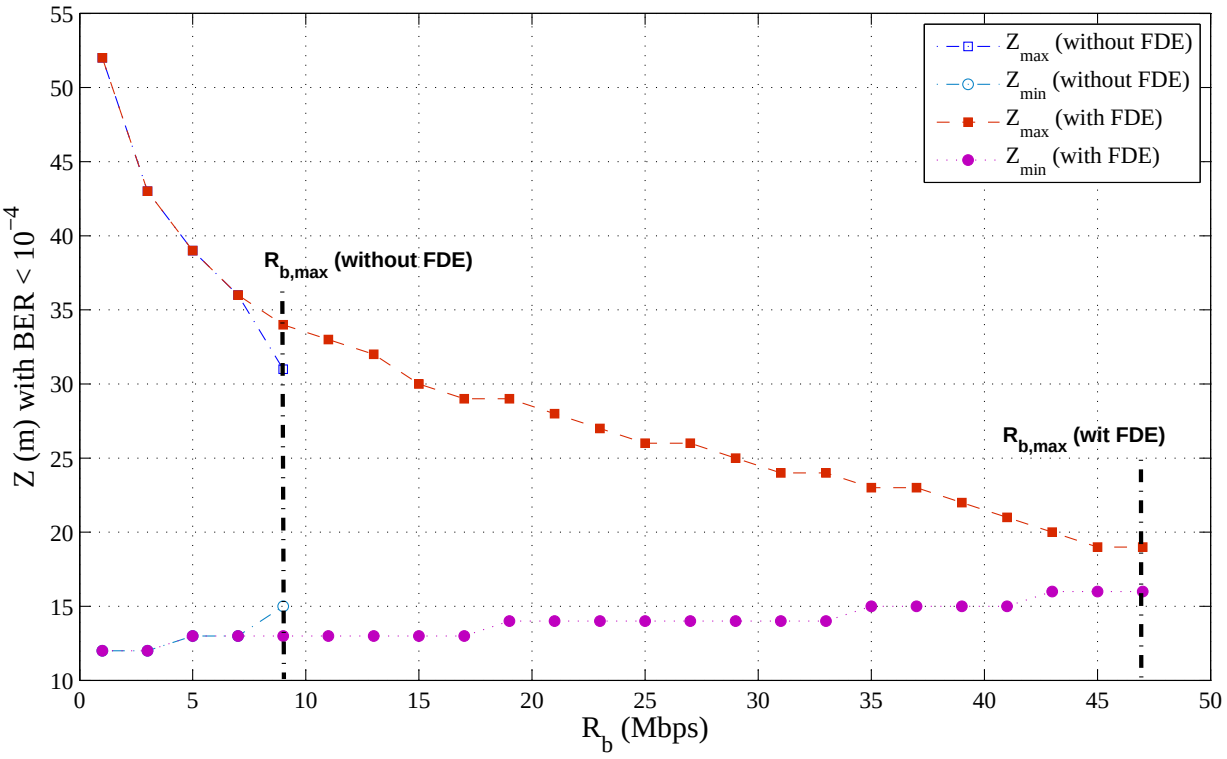

Figure 5.11: Maximum and minimum achievable link distance Z satisfying BER $< 10^{-4}$ versus data rate R_{b}. Uncoded 4-PAM modulation, PQ-SiPM-based Rx, system operating in clear ocean waters with $K = 0.08\,\mathrm{m}^{-1}$.

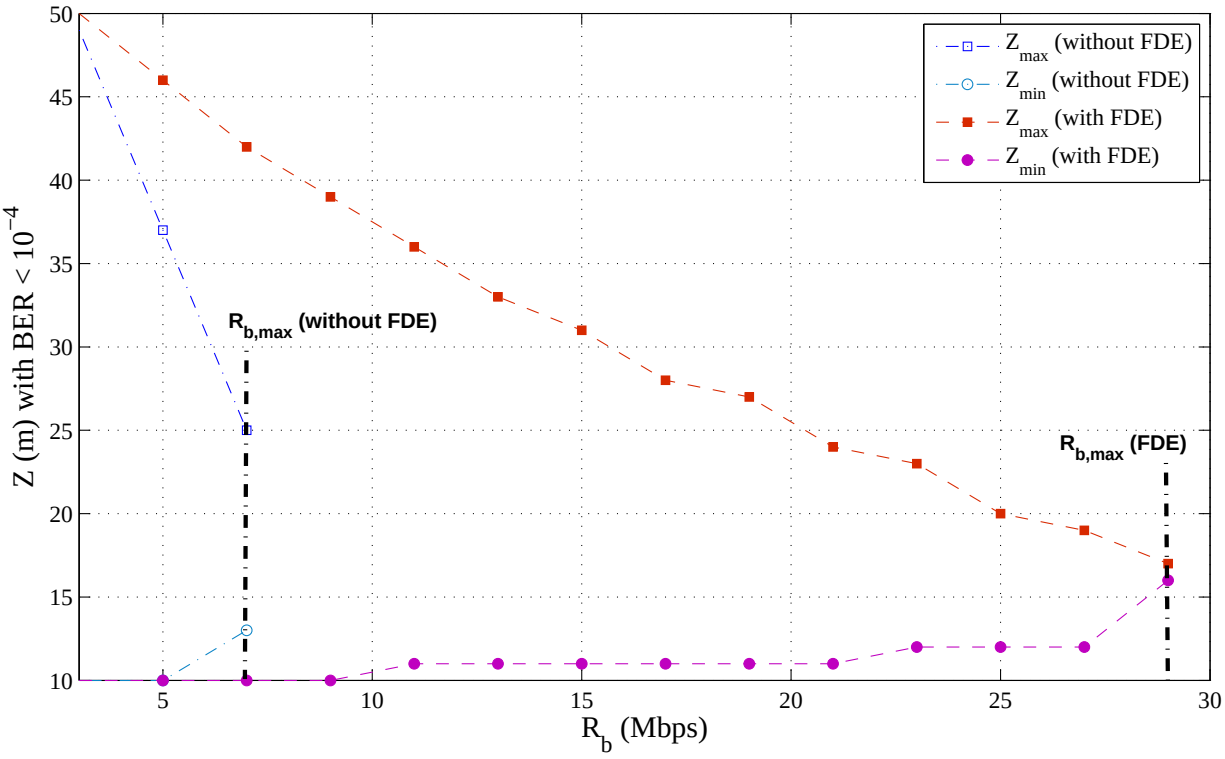

Figure 5.12: Maximum and minimum achievable link range Z satisfying BER $< 10^{-4}$ versus data rate R_b. Uncoded 16-PPM modulation, PQ-SiPM-based Rx, system operating in clear ocean waters with $K = 0.08\,\mathrm{m}^{-1}$.

5.5 Conclusion

In this chapter, we investigated the impact of the LED and the SiPM limited bandwidths on the UWOC link performance. We showed that when no equalization is performed, and for relatively high data rates (∼2 Mbps), the link performance is limited by the frequency selectivity of the aggregate channel, for the three considered modulation schemes, i.e., OOK, 4-PAM, and 16-PPM. We introduced the frequency domain equalization as an interesting solution to mitigate the effect of the limited operation bandwidth. We demonstrated that for a fixed link range, FDE allows to enlarge the interval of Z ensuring a low BER. Furthermore, we showed how FDE allows to attain higher data rates compared to the case where no equalization is performed. This is very important for the design of high speed UWOC links based on an SiPM PD.
In the next chapter, we present a set of experimental works on a simple optical communication link with an LED-based Tx and a PQ-SiPM-based Rx in order to validate the main results we presented so far. In particular, we measure the end-to-end channel response, and experimentally validate the interest of the FDE technique.

Chapter 6

Experimental validations

Contents

6.1 Introduction

In the previous chapters, we evaluated the performance of a typical SiPM-based UWOC link, based on analytical calculations and numerical simulations. Here, we aim to complete our study and validate our theoretical findings through experimental tests. For this purpose, we developed a test-bed and conducted a series of experiments. In particular, we measured the aggregate channel frequency response and studied the link BER performance when varying the data transmission rate.
The description of the experimental setup, and the different electronic and optical components used within it, is provided in Section 6.2. Then, in Section 6.3, we measure the end-to-end channel frequency response, firstly providing the related theoretical description, and secondly presenting the outcome of our experimental tests.

6.2 Experimental Setup description

Our test-bed consists in a simplex point-to-point optical communication link, whose schematic representation is provided in Fig. 6.1. The Tx block is composed of a computer, a *PM8572A* waveform generator from *Tabor Electronics* [137], and a blue Nichia NSPB510AS LED [60]. Here, the binary data to be transmitted are randomly-generated and then modulated offline in the computer. Next, the output bit stream is loaded to the waveform generator, which produces a corresponding electrical signal that will drive the LED. The waveform generator is directly commanded from the computer via *ArbConnection* 4.3 software and is connected to the LED via a coaxial cable.

The optical signal is transmitted through an optical fiber, employed here as a substitute to the underwater propagation channel, given that we did not have available a water tank or basin in the laboratory. Our main objective being to study the SiPM performance when varying the data rate, and given that the optical fiber does not attenuate the signal as expected in water, we simulate the channel attenuation effect by decreasing the light intensity at the Tx.
At the Rx side, the photo-detection is carried out by a MicroSB-30035 SensL SiPM [136], bonded to the optical fiber and wrapped by an opaque tape so as to prevent the detection of parasitic ambient light. The SiPM is employed jointly with a power supply and preamplifier module, regarded as a simple 'plug and play' readout solution to be used with SensL's SiPMs. It interfaces with the PD, performs a signal amplification, and provides the detector bias voltage and the power supply needed by the preamplifier. Thus, it allows working with the SiPM with minimal additional equipments. The PD output is passed via a coaxial cable to the *Wavesurfer Xs-A* oscilloscope from *LeCroy* [138]. This latter enables data acquisition, visualization, and analysis, and has an integrated Windows XP operating system on-board. Lastly, the oscilloscope sampled and low-pass filtered signal is saved and loaded to the computer, where signal demodulation is performed so as to retrieve the transmitted bit stream. Snapshots of our test-bed are provided in Figs. 6.2 and 6.3.

In the following, we will start by measuring the aggregate channel frequency response, which is used later to perform channel equalization. Then we evaluate the BER performance of the communication link as a function of the data rate without and with channel equalization.

6.3 Measuring channel frequency response

Assuming that our system is linear and time-invariant (LTI), we start by measuring the frequency response of the aggregate channel, denoted here by $H_{\text{eq}}(f)$, which includes the LED, the propagation channel, and the SiPM PD. To do so, we generated a bunch of sinusoidal signals at different frequencies, and measured their amplitudes at both the Tx and Rx, denoted by V_{in} and V_{out}, respectively . The magnitude of the frequency response is then calculated as $|H_{\text{eq}}(f)| = V_{\text{out}}/V_{\text{in}}$.

The experimental measurements of $|H_{\text{eq}}(f)|$ obtained are presented in Fig. 6.4 (red line). In order to exploit these data in the following, we fit the curve of $H(f)$ by the frequency response of a second order LPF, whose transfer function is expressed as follows:

$$H_{\text{LPF}}(s) = \frac{b}{a_3 + a_2\, s + a_1\, s^2} \tag{6.1}$$

The related coefficients a and b are calculated using Matlab function 'invfreqs', which transforms an in-laboratory-measured frequency response data into a transfer function. As shown in Fig. 6.4, the second order LPF frequency response (blue line) constitutes a good approximation to the measured data. As depicted in the figure,

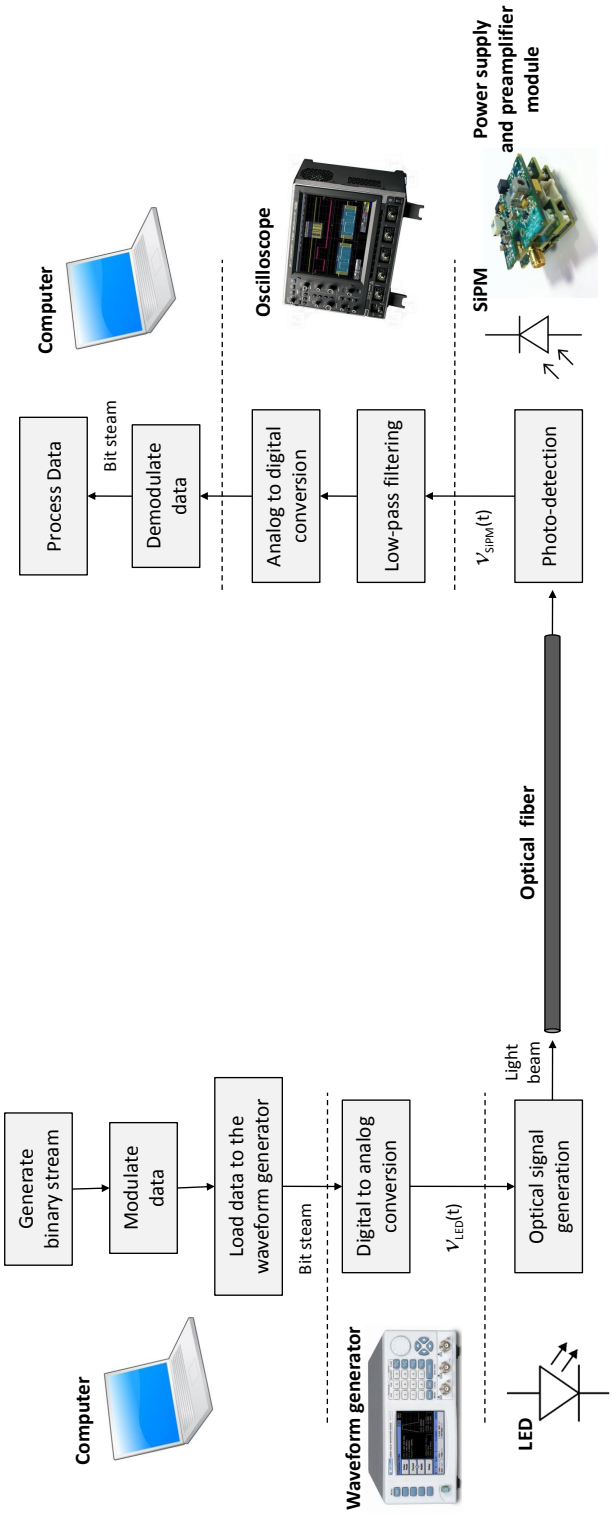

Figure 6.1: Block diagram of the experimental setup.

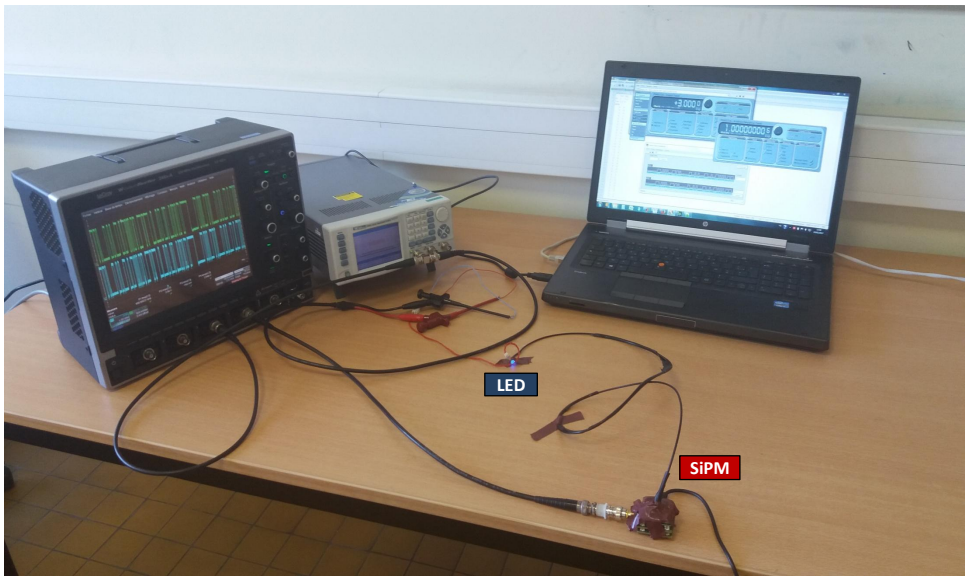

Figure 6.2: Experimental set-up.

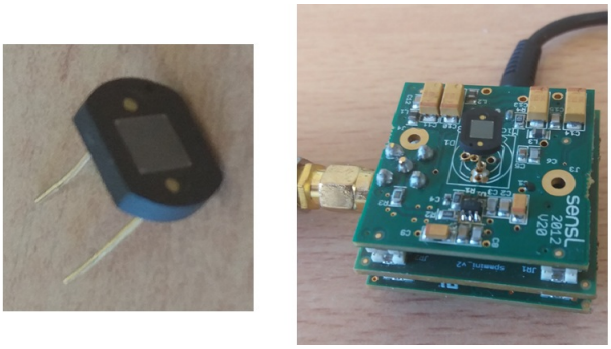

Figure 6.3: SiPM and his power supply and preamplifier module.

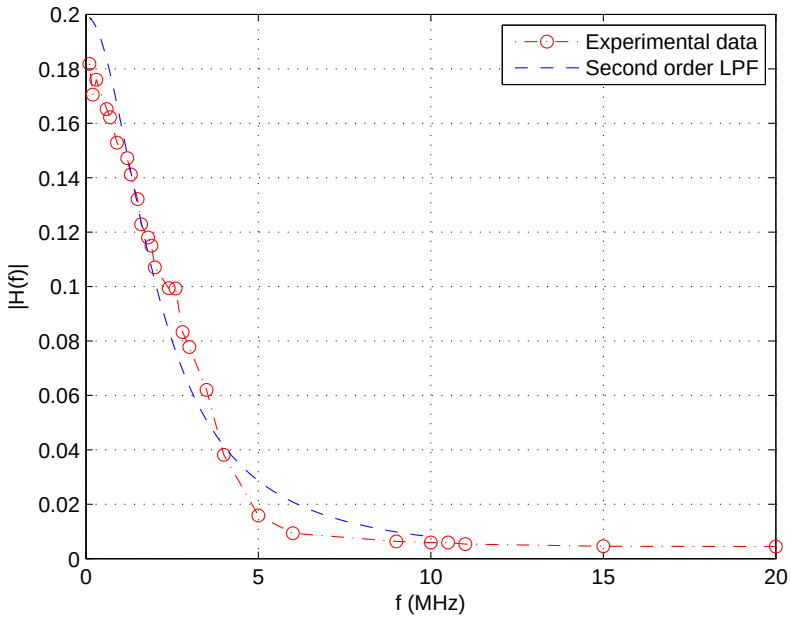

(a) $|H(f)|$

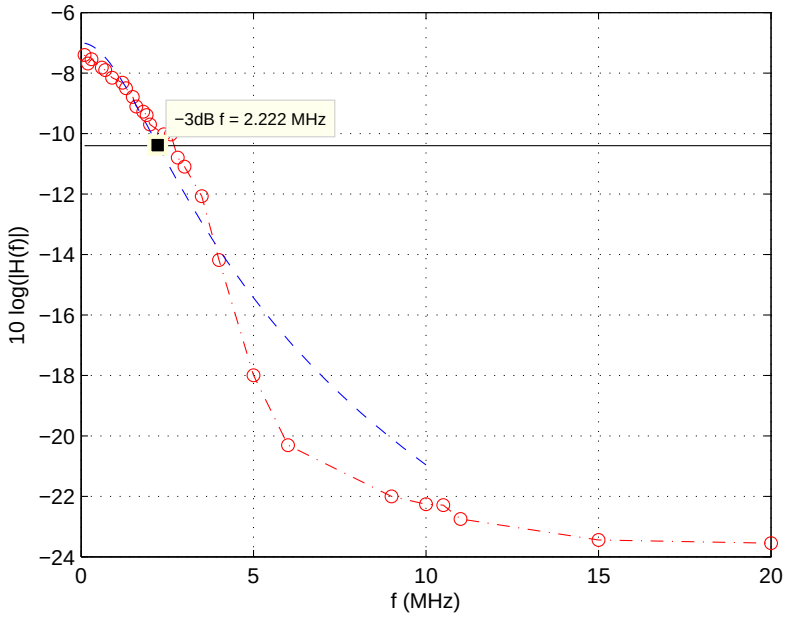

(b) $|H(f)|$ in dB

Figure 6.4: Measured frequency response of the setup aggregate channel.

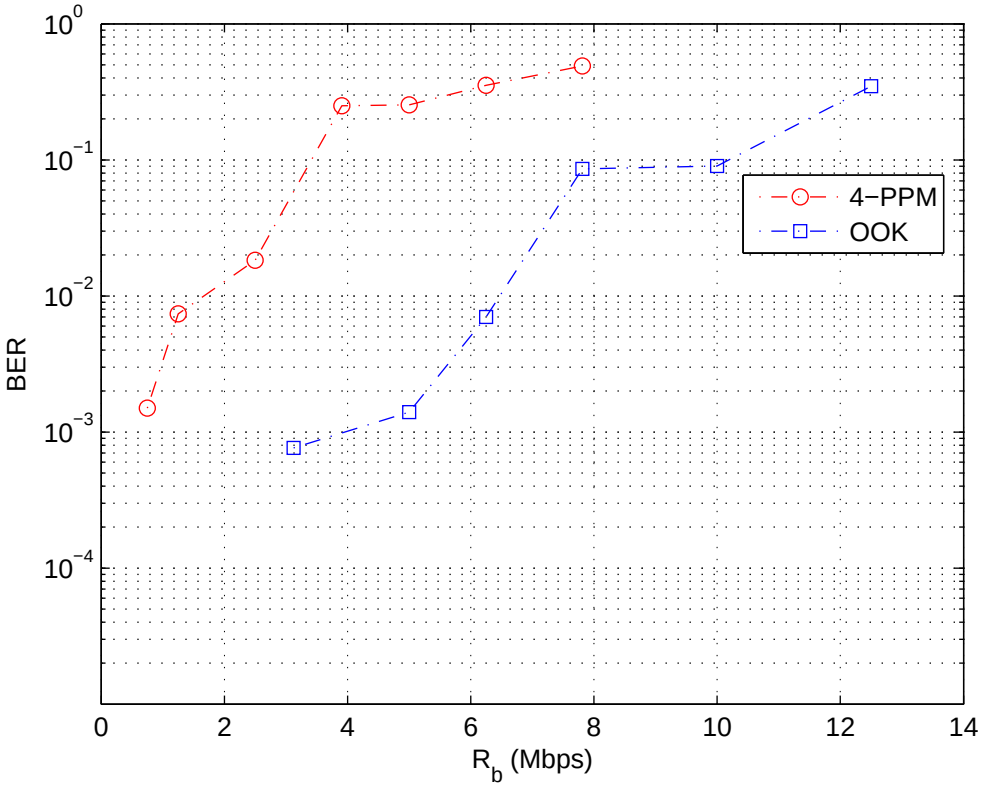

Figure 6.5: Experimental BER for OOK and 4-PPM.

we have a -3 dB cut-off frequency of around 2.2 MHz. This confirms the rationality of the value of $f_{c,SiPM} = 2$ MHz that we adopted in Chapter 5. Furthermore, it confirms that the main limitation over the operation bandwidth is imposed by the SiPM component.

6.4 Measuring BER variation versus data rate

Les us now study the variation of the transmission BER versus the data transmission rate for the cases of uncoded NRZ-OOK and 4-PPM modulations. These latter were considered here for their implementation simplicity and constitute an illustrative example for system performance analysis.

The experimental results are presented in Fig. 6.5. As expected, the BER performance deteriorates when R_b increases, for both considered modulation schemes. Indeed, the BER is approximately 10^{-3} at 3 and 1.5 Mbps, while it reaches 0.5 at 12 and 8 Mbps, for the cases of OOK and 4-PPM, respectively. As expected and in concordance with our theoretical study, OOK has a better performance than 4-PPM. As explained earlier in Subsection 5.3.3, this can be explained by the fact that, at

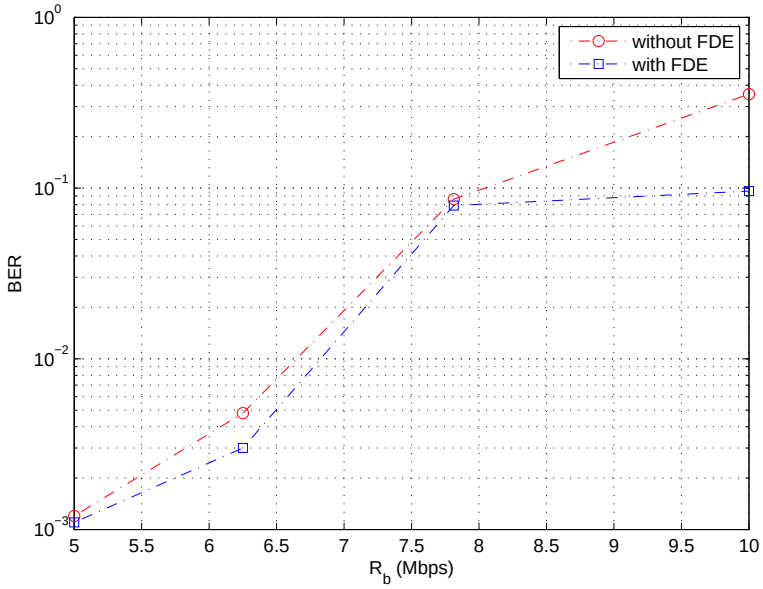

Figure 6.6: Comparing experimental BER versus data transmission rate, of an OOK-based transmission, with and without FDE.

equal data rates, a 4-PPM signal occupies two times more bandwidth as compared to OOK.

6.5 Benefit of channel equalization

To see the benefit of FDE on the BER performance for the case of OOK modulation, given the channel frequency response, we calculate the equalization coefficients to be applied to the Fourier transform of the Rx signal previously recorded. The simulation results are presented in Fig 6.6. We notice that, as expected, FDE provide a BER performance enhancement, albeit minimal. The reduced effect of FDE can be explained referring to Fig. 5.10. In effect, within our test-bed, we simulate the aquatic channel by a optical fiber. This latter does not attenuate power as water, and although we considered a low power level, this last may still be high enough to correspond to the case where an UWOC link is established over a low distance. For this specific case figure, referring to the above mentioned figures, the effect of FDE cannot be clearly noticed.

6.6 Conclusion

In this chapter, we presented a set of experimental result to evaluate the performance of a typical UWOC link employing an SiPM PD. We provided the description of our test-bed and presented the main results we obtained. In particular, we

quantified the propagation channel frequency response and confirmed that the SiPM imposes the main limitation of the system bandwidth, and validated the value of the cut-off frequency that we considered earlier in our theoretical study. We also evaluated the link BER for increasing data rate for the case of an OOK-based transmission.

In conclusion, these experiments enabled us to validate a part of the previous results obtained by simulation, and concerning the performance of an SiPM based communication link. It also allowed us to highlight the main contribution of channel equalization technique to further improve the transmission quality. Additional test should be conducted to evaluate real benefit of FDE in improving the system performance.

Chapter 7

Conclusions and perspectives

Contents

7.1 Conclusions

UWOC is a promising technology for establishing high data-rate and reliable underwater communication links. It provides numerous advantages compared to the acoustics-based counterpart, including a large bandwidth, a high propagation speed, and compact and cost-effective components. However, in terms of achieving long-range transmissions, we are concerned with a major impairment, which consists in the high signal attenuation within the aquatic propagation channel. Furthermore, an additional important impediment to establishing relatively high data rate transmission (over several tens of Mbps) is caused by the limited operation bandwidth of the opto-electronic components and devices employed at the Tx and Rx, for instance, LEDs and PDs. In this thesis, we focused on investigating the potential limitations arising from these two impairments and proposed solutions to mitigate their effects, by considering the use of advanced photo-detectors and signal processing techniques in order to improve the performance of UWOC links.

In this view, we first studied the effect of solar background noise on the performance of UWOC links in Chapter 3, often neglected in the literature. Indeed, we presented an analytic generic model of this noise and studied its impact on the transmission performance in terms of BER. We showed how the sensitivity to solar radiations varies depending on both the operation depth and the Rx characteristics, and that it can severally deteriorate the transmission quality, particularly when operating in shallow depths where the propagation medium cannot be effectively considered as dark.

After this preliminary study, which can provide UWOC system designers and users with insightful information about solar background noise effect, we investigated in Chapter 4 the use of recent promising photo-detectors in the Rx, i.e. SiPMs. We studied the corresponding system performance in different conditions of water turbidity, and demonstrated that, thanks to their high sensitivity to low

optical signal levels down to a single photon, SiPMs can increase significantly the transmission range. Furthermore, we investigated different modulation techniques to be employed with SiPMs, in the aim of further improving the link performance.

In Chapter 5, we studied the effect of the bandwidth limitation of the emitters and SiPMs on the maximum achievable data transmission rates and determined the scenarios where they may effectively limit the data rate and the link span. Then, we proposed and investigated the use of an efficient transmission solution, mainly based on channel equalization in the frequency domain, in order to surpass the bandwidth limitations, and demonstrated its benefits.

Lastly, we validated some of our simulation results through an experimental work in Chapter 6. Thanks to the support from IFREMER institute, we could develop a test-bed and carry out some experimental measurements. After validating our assumptions on the frequency response of the aggregate channel including the LED and the SiPM, we measured the BER performance of an SiPM-based link when varying the data transmission rates, for the cases of NRZ OOK and 4-PPM transmission schemes. We demonstrated to which extent, when no channel equalization is performed, the communication performance deteriorates for relatively high data rates. These results validated our main conclusions in Chapter 5.

7.2 Perspectives

This thesis was devoted to analyzing the performance of long-range and high data rate UWOC links and to proposing the use of advanced opto-electronic components and efficient signal processing techniques in order to face the main related limitations. The work presented in this thesis responds to the main part of the objectives presented in Chapter 1. However, there unquestionably still remains several other aspects to investigate.

Considering background noise affecting UWOCs, we focused in this thesis on solar noise and provided an analytic and generic model to quantify it. To complete this study, it would be judicious to study the impact of ambient light arising from submarine vehicles' lighting in deep waters. Furthermore, as a future extension of this work, it is important to investigate a more general link configuration (with respect to the link optical axis and sun position) and to evaluate the precise level of captured solar noise at the Rx. For such cases, the solar noise power captured at the Rx is not solely determined by the downwelling plane irradiance and a more general model taking into account the diffused light in water should be considered.

Concerning the use of SiPMs in UWOCs examined in Chapter 4, further investigations can focus on the study of the saturation behavior of these components, for the case of very short link distances. Indeed, we noticed that, at a relatively short link spans, the received power can be too high and can result in Rx saturation. A more precise characterization of this phenomenon and design of suitable electronics in order to adaptively modify the SiPM gain when approaching the saturation limit would be an interesting issue to explore. This can also be realized through

the adaptive setting of the transmit power through some adequate transmission protocols, when a feedback channel can be established. Another option could be to design a hybrid UWOC Rx, which combines an SiPM, particularly adapted for long range communications due to its sensitivity, and a classical photo-diode, for instance an APD, which provides high performance for short range links while not being concerned with saturation.

Concerning the impact of the opto-electronic systems' characteristics on an UWOC link performance, particularly the bandwidth limitation investigated in Chapter 5, future research should consider additional impediments related to these components, which can further deteriorates the transmission quality. Among these, it would be interesting to study the effect of the non-ideal characteristics of LEDs which result in a non-linear distortion of their output signal (this is the case when the output signal is no more linearly proportional to input signal). This issue is widely considered in the context of VLC for instance. Then, it would be also interesting to propose efficient non-linear equalization techniques in the aim of mitigating the signal distortion introduced by LEDs.

In addition to the above mentioned directions, future studies should investigate the effect of a wider range of practical challenges facing UWOCs, such as link misalignment, that is very likely to happen for instance when a mobile underwater vehicle is involved in the communication. A loss of beam alignment between the Tx and Rx can severely affect the link and efficient localization and beam tracking mechanisms should be designed. Another practical challenge facing UWOCs which is worth further investigation is the underwater turbulence. Although often neglected in the literature, this phenomenon can have perilous effects on the signal quality and therefore needs to be characterized accurately. Should also be considered the design of efficient error correcting codes adapted to the challenging underwater environment, while focusing on low decoding complexity.

Appendix A

Optical filters and concentrators

A.1 Optical Filters

UWOC receivers typically employ band-pass optical filters to reduce the amount of collected ambient light. These latter can have narrow optical bandwidths, below 1 nm, which results in high ambient light rejection and consequently a better SNR. Obviously, the filter bandwidth should be adapted ti that of the Tx. For the case of typical LDs, this bandwidth could be as narrow as several nm, in contrast to tens on nm for an LED.
The transmission spectrum of a typical optical band-pass filter is presented in Fig. A.1. It shows that the filter pass band can highly depend in the beam incident angle, denoted here by θ. This dependence of the filter bandwidth on θ can be problematic in the case where the Rx is expected to capture light over a wide FOV, i.e. a wide range of incident angles [91]. For such case, the limitations imposed by the optical filter must be taken into consideration.

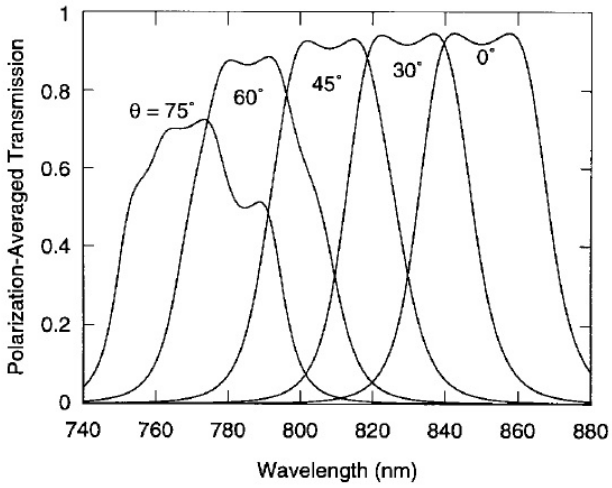

Figure A.1: Averaged transmission of an optical band-pass filter for rays incident at angle θ, reproduced from [91].

A.2 Optical concentrators

The detected optical power by a PD is proportional to its effective light-collection area. However, its photo-sensitive physical area cannot be arbitrary increased, being a costly operation, and leading to the reduction of the PD bandwidth and the increase of the relared noise (e.g. shot noise) [91]. We can alternatively employ an optical concentrator so as to increase the PD effective collection area. There exist two types of optical concentrators: imaging and non-imaging. Imaging concentrators, such as Fresnel lenses, are widely used in long-range, free-space optical links, while short-range infrared links often employ widely non-imaging ones.

A typical example of a non-imaging concentrator is a hemispherical lens. It can achieve a wide FOV and omnidirectional gain, and hence, is regarded as particularly suitable for non-directed links such as in infrared communications. As shown in Fig. A.2, it can be employed jointly with a hemispherical band-pass filter bonded onto its outer surface.

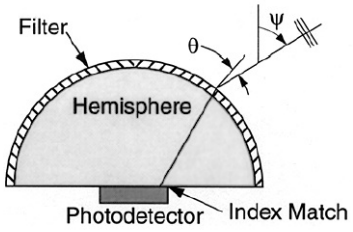

Figure A.2: Non-imaging optical hemispheric concentrator with optical filter, reproduced from [91].

For more directed beam transmissions, compound parabolic concentrators (CPCs) are more suitable than hemispherical lenses, allowing to attain a higher gain, yet at the expense of a narrower FOV, see Fig. A.3. This type of non-imaging concentrator is widely considered in infrared links.

A comparison of the effective signal-collection areas achieved by ideal non-imaging concentrators is presented in Fig. A.4. It shows clearly the trade-off to make between FOV and the concentration gain (represented by the colored area surface) when selecting the optical concentrator.

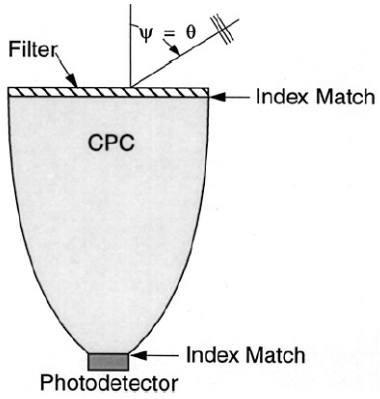

Figure A.3: Non-imaging optical CPC concentrator with planar optical filter, reproduced from [91].

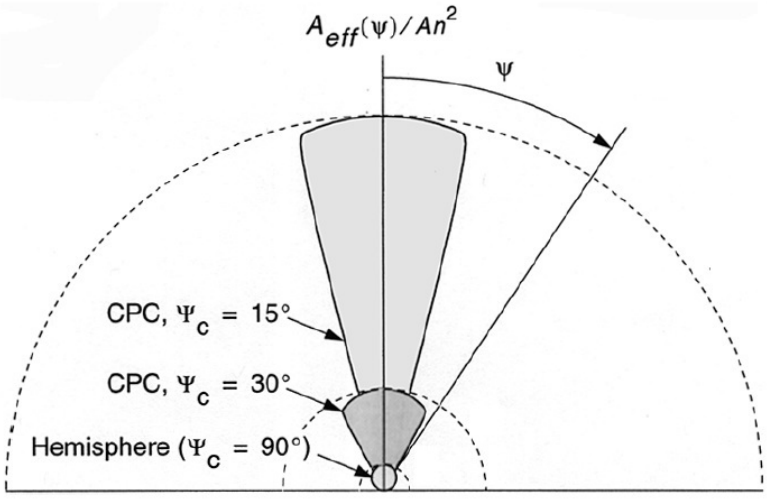

Figure A.4: Effective light-collection areas A_{eff} achieved by ideal concentrators. Here ψ_c denotes the concentrator FOV, A the physical area of the PD, n the refraction index of the concentrator. Reproduced from [91].

Appendix B

Underwater optical modem prototype

B.1 Introduction

This thesis was in part funded by the French Institute for the Study of the Sea (IFREMER) and conducted in collaboration with the submarine system department. Consistent with the research work in this thesis on the feasibility and the interest of employing SiPM photo-detectors in UWOCs, the IFREMER engineers designed, developed, and experimentally tested an underwater optical modem based on the SiPM technology. In this appendix, we provide a description of this prototype, along with the main related experimental results.

B.2 Modem overview

The receiver is composed of 8 fast blue-sensitive SiPMs, each one having an active area of $36\,mm^2$ and providing an FOV of almost 30°. The ensemble of the SiPM array provides an almost omnidirectional pattern. The receiver is integrated in a cylindrical housing with a spherical glass BK7 dome, as depicted in Fig. B.1. Using comparators, the strongest output signal is selected, amplified with a high gain amplifier, following by a threshold comparator. After this front end electronics, signal demodulation is done within an FPGA and the decoded signals are sent to an ARM embedded Ethernet board.

The transmitter is composed of 120 fast blue LEDs, arranged on a circular epoxy board (see Fig. B.2), and associated with a fast high power amplifier. The transmitted beam angle is around 120°. The Ethernet signal input is encoded by the same FPGA/ARM boards as that employed at the receiver.

B.3 Test description

At this stage of development, only on SiPM is used, the communication link is simplex, and no error correction coding is used. The data transmission is based on a Manchester-coded OOK modulation.
Although these considered implementation choices allow limited investigation, they are nevertheless useful for evaluating the performance of an SiPM PD.
In 2015 and 2016, with the support of Total company, IFREMER performed a bench

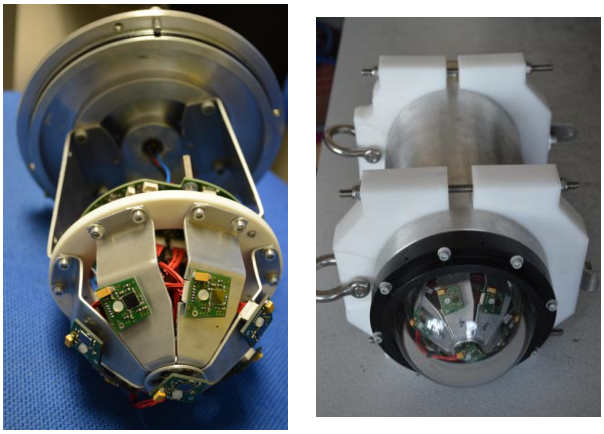

Figure B.1: Receiver SiPM's Antenna with its housing.

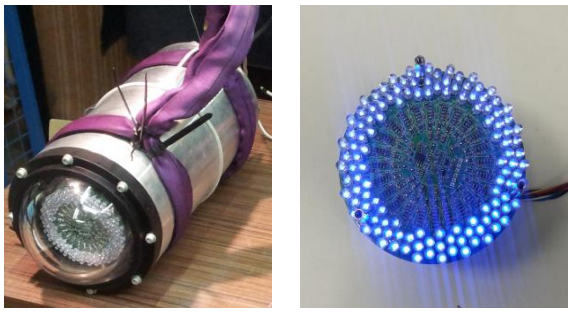

Figure B.2: LEDs Transmitter with its housing.

of experimental tests of this prototype as well as the *BlueComm 200* modem from Sonardyne Co., and which employ PMTs at the Rx. They tested the performance of these two systems in different locations in open sea, with different water qualities ranging from Jerlov I (which corresponds to deep clear ocean waters) to Jerlov 5 (which corresponds to turbid coastal waters). The Vortex ROV (presented in Fig B.3) was employed as the mobile platform, which integrated the transmitter (mounted horizontally on starboard side of Vortex with clamps, see Fig B.4), while the receiver was fixed on the ship. This latter was equipped with WiFi, GPS, and INU. All the measurements were made in the configuration where the Vortex was moving away from the ship. The water turbidity was further measured by a Transmissometer to characterize the aquatic channel.

Given that the optical modems are designed to work with little or no ambient light, all tests in the open sea are carried out during the night, see Fig. B.5.

B.4 Experimental results

The IFREMER testing team concluded that the two optical underwater modems under test are not directly comparable. Indeed, the *BlueComm 200* is an already

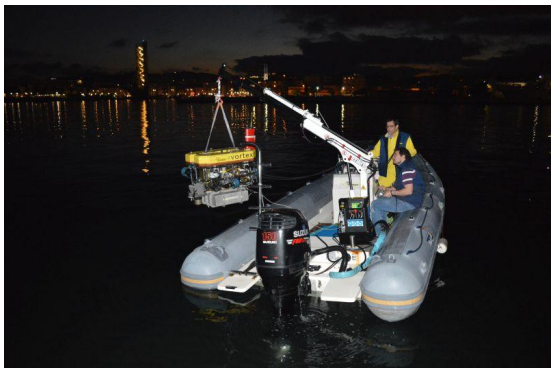

Figure B.3: Vortex's Deployment with RIB.

Figure B.4: Transmitter Ifremer's Optical modem integrated on Vortex.

Figure B.5: First test in the harbor.

commercialized product, while IFREMER's SiPM-based modem is still a prototype with less features.

The PMT-based *BlueComm 200*, seems to perform better, thanks to the high sensitivity of PMTs to very low light intensity, and their high gain and low noise. However, as explained in Section 4.2, they require high operation voltage, are easily damaged by exposure to ambient light, are sensitive to magnetic fields and fragile.

On the other hand, recent SiPMs used within Ifremer's prototype, have become well recognized as being very competitive photo-detectors, thanks to their high sensitivity and time resolution and ease of implementation.

The in-sea tests of SiPM and PMT-based modems, performed in similar situations (in terms of water quality, fixed to fixed platform, fixed to mobile platforms) allowed to make the following conclusions.

The FOV of the PMT is equal to 90° on each side, and is greater than that of the SiPM, which is in the order of 30°. Note that the antenna composed of 8 SiPMs should allow a wider beam diagram.

Regarding the attained transmission range, Table B.1 summarizes the measured performance. It is concluded that the PMT-based modem allows attaining longer ranges than SiPM-based one, by almost 25%.

Table B.1: Range performances

Modem	Water Quality in NTU	Water classification	Max range
BlueComm 200	4	Jerlov 5	24m at 2.5Mbps
Ifremer's SiPM	4	Jerlov 5	17m at 3Mbps
BlueComm 200	0.32	Jerlov I	80m at 2.5Mbps
Ifremer's SiPM	0.32	Jerlov I	60m at 3Mb/s

Regarding the maximum achievable data rate, it was concluded that *BlueComm 200* and SiPM-based prototype tolerate up to 10 Mbps, and 3 Mbps, respectively.

Bibliography

[1] J. R. Potter, M. B. Porter, and J. C. Preisig, "Ucomms: A conference and workshop on underwater communications, channel modeling, and validation," *IEEE Journal of Oceanic Engineering*, vol. 38, no. 4, pp. 603–613, Oct 2013. (Cited on page 2.)

[2] Discover of sound in the sea, http://www.dosits.org/people/history/early1900/. (Cited on page 2.)

[3] P. Lacovara, "High-bandwidth underwater communications," *Marine Technology Society Journal*, vol. 42, no. 1, pp. 93–102, Mar. 2008. (Cited on pages 8, 9, 25, 27, 28, 29, 37, 39, 40, 46, 47 and 56.)

[4] M. Chitre, S. Shahabudeen, and M. Stojanovic, "Underwater acoustic communications and networking: Recent advances and future challenges," *Marine Technology Society Journal*, vol. 42, no. 1, pp. 103–113, Mar. 2008. (Cited on page 8.)

[5] I. F. Akyildiz, D. Pompili, and T. Melodia, "Underwater acoustic sensor networks: Research challenges," *Ad Hoc Networks (Elsevier)*, vol. 3, no. 3, pp. 257–279, Mar. 2005. (Cited on page 8.)

[6] M. Stojanovic, "Underwater wireless communications: current achievements and research challenges." IEEE Oceanic Engineering Society Newsletter, vol. 41, pp. 2–7, 2006. (Cited on page 8.)

[7] M. A. J. Lloret, S. Sendra and J. J. P. C. Rodrigues, "Underwater wireless sensor communications in the 2.4 ghz ism frequency band," *Sensors*, vol. 12, no. 4, pp. 4237–4264, Mar. 2012. (Cited on page 9.)

[8] J. Shi, S. Zhang, and C. J. Yang, "High frequency rf based non-contact underwater communication," in *OCEANS Conference*, May 2012, pp. 1–6, . (Cited on page 9.)

[9] X. Che, I. Wells, G. Dickers, P. Kear, and X. Gong, "Re-evaluation of rf electromagnetic communication in underwater sensor networks," *IEEE Communications Magazine*, vol. 48, no. 12, pp. 143–151, Dec. 2010. (Cited on page 9.)

[10] H. Kaushal and G. Kaddoum, "Underwater optical wireless communication," *IEEE Access*, vol. 4, pp. 1518–1547, 2016. (Cited on pages xv, 9, 11, 12, 13, 14, 25, 26, 27, 29, 33 and 57.)

[11] A. I. Al-Shamma'a, A. Shaw, and S. Saman, "Propagation of electromagnetic waves at mhz frequencies through seawater," *IEEE Transactions on Antennas and Propagation*, vol. 52, no. 11, pp. 2843–2849, Nov 2004. (Cited on page 9.)

[12] M. R. Frater, M. J. Ryan, and R. M. Dunbar, "Electromagnetic communications within swarms of autonomous underwater vehicles," in *Proceedings of the 1st ACM International Workshop on Underwater Networks*, New York, NY, USA, 2006, pp. 64–70. (Cited on page 9.)

[13] H. Kulhandjian, "Inside out: Underwater communications," *The Journal of Ocean Technology (JOT)*, vol. 9, no. 2, pp. 104–105, Jul. 2014. (Cited on page 9.)

[14] H. Brundage, *Designing a Wireless Underwater Optical Communication System.* Master thesis, Massachusetts Institute of Technology, Feb. 2010, [Online]. Available: https://dspace.mit.edu/handle/1721.1/57699. (Cited on pages xi and 9.)

[15] M. A. Khalighi, C. Gabriel, T. Hamza, S. Bourennane, P. Léon, and V. Rigaud, "Underwater wireless optical communication; recent advances and remaining challenges," pp. 1–4, July 2014, Graz, Austria. (Cited on page 9.)

[16] C. Gabriel, M. A. Khalighi, S. Bourennane, P. Léon, and V. Rigaud, "Monte-carlo-based channel characterization for underwater optical communication systems," *IEEE/OSA Journal of Optical Communications and Networking*, vol. 5, no. 1, pp. 1–12, Jan. 2013. (Cited on pages 10, 15, 22, 24 and 79.)

[17] L. J. Johnson, R. J. Green, and M. S. Leeson, "Hybrid underwater optical/acoustic link design," in *16th International Conference on Transparent Optical Networks (ICTON)*, July 2014, pp. 1–4. (Cited on page 10.)

[18] F. Hanson and S. Radic, "High bandwidth underwater optical communication," *Applied Optics*, vol. 47, no. 2, pp. 277–283, Jan. 2008. (Cited on pages 10, 24, 26, 29, 34, 40 and 56.)

[19] S. Arnon, "Underwater optical wireless communication network," *Optical Engineering*, vol. 49, no. 1, pp. 1–6, Jan. 2010. (Cited on page 10.)

[20] Underwater Optical Networks technologies, http://www.uontechnologies.com/. (Cited on page 10.)

[21] WHOI, "Revolutionary communications system promises new generation of untethered, undersea vehicles," *http://phys.org/news/2010-06-revolutionary-untethered-undersea-vehicles.html*, Jun. 2010. (Cited on page 10.)

[22] D. R. Bacon and D. R. Jarvis, "General physics: Acoustics," *Nat. Phys. Lab., Tech. Rep.*, Jul. 2005, [Online]. Available: www.kayelaby.npl.co.uk/general_physics/2_4/2_4_1.html. (Cited on page 11.)

[23] L. Butler, "Underwater radio communication," Amateur Radio, Tech Rep., 1987, [Online]. Available:

http://users.tpg.com.au/users/ldbutler/Underwater_Communication.pdf. (Cited on page 11.)

[24] J. Davies, "Subsea wireless communication: Technology comparison and review," *Work presentation for Juice-DSP, Dorset, U.K.*, [Online]. Available: http://www.oceanologyinternational.com/__novadocuments/49643?v=635314268958030000. (Cited on page 11.)

[25] J. H. Smart, "Underwater optical communications systems part 1: variability of water optical parameters," in *IEEE Military Communications Conference (MILCOM)*, vol. 2, Oct. 2005, pp. 1140–1146. (Cited on page 12.)

[26] J. W. Giles and I. N. Bankman, "Underwater optical communication systems. part 2 : Basic design considerations," *Military Communications Conference (MILCOM)*, vol. 3, pp. 1700–1705, Oct. 2005, Atlantic City, NJ, USA. (Cited on pages 12, 22, 23, 39 and 40.)

[27] C. E. D. C. Richard L. Miller and B. A. McKee, *Remote Sensing of Coastal Aquatic Environments: Technologies, Techniques and Applications*. Springer Science & Business Media, Mar. 2007. (Cited on page 12.)

[28] R. C. Smith and K. S. Baker, "Optical properties of the clearest natural waters (200–800 nm)," *Appl. Opt.*, vol. 20, no. 2, pp. 177–184, Jan 1981. (Cited on page 13.)

[29] L. J. Johnson, *The underwater optical channel*. Dept. Eng., Univ. Warwick, Coventry, U.K., Tech. Rep., 2012. (Cited on page 13.)

[30] S. Q. Duntley, "Light in the sea," *Journal of the Optical Society of America (JOSA)*, vol. 53, no. 2, pp. 214–233, Feb. 1963. (Cited on pages 14, 22, 23, 37, 40 and 44.)

[31] L. Mullen, "Optical propagation in the underwater environment," *Atmospheric Propagation VI, Proc. SPIE*, vol. 7324, pp. 732 409–732 409–9, May 2009, . (Cited on page 14.)

[32] W. Cox, J. Simpson, and J. Muth, "Monte carlo simulation of turbid water channels and use of segmented field of view smart transmitters and receivers for underwater optical communications," in *Underwater Communications Networking (UComms)*, Sep. 2012, Sestri Levante, Italy. (Cited on page 14.)

[33] B. M. Cochenour, L. J. Mullen, and A. E. Laux, "Characterization of the beam-spread function for underwater wireless optical communications links," *IEEE Journal of Oceanic Engineering*, vol. 33, no. 4, pp. 513–521, Oct 2008. (Cited on page 15.)

[34] B. Cochenour, L. Mullen, and A. Laux, "Spatial and temporal dispersion in high bandwidth underwater laser communication links," in *IEEE Military Communications Conference (MILCOM)*, Nov 2008, pp. 1–7. (Cited on page 15.)

[35] C. Mobley, *Light and Water: Radiative Transfer in Natural Waters*. Academic Press, 1994. (Cited on pages 15, 16, 19, 21, 22, 23 and 40.)

[36] B. Woźniak and V. N. Pelevin, "Optical classifications of the seas in relation to phytoplankton characteristics," *Oceanologia*, vol. 31, pp. 25–55, Dec. 1991. (Cited on pages 15, 16, 17, 18, 19 and 20.)

[37] Y. Ding, Q. Ding, and Q. Liu, "Performance analysis of optical modulation in underwater slant transmission," *International Journal of Innovative Computing, Information and Control*, vol. 9, no. 9, pp. 3799–3805, Sep. 2013, . (Cited on pages 15 and 23.)

[38] N. Jerlov, "The optical classification of sea water in the eutrophic zone," *Kobenhabns Univ. Instit. Fys. Oceanogr.*, vol. Report No. 36, 1978, Copenhagen, Denmark. (Cited on page 16.)

[39] E. B. C. Mobley and C. Roesler, *Ocean Optics Web Book*, http://www.oceanopticsbook.info/, 2016. (Cited on pages 17, 23, 44 and 45.)

[40] C. Gabriel, *Channel Characterization and Performance Analysis for an Underwater Optical Transmission System*. Aix-Marseille University: PhD Thesis, May 2013. (Cited on pages 21, 22, 48 and 71.)

[41] T. Hamza, M. A. Khalighi, S. Bourennane, P. Léon, and J. Opderbecke, "On the Suitability of Employing Silicon Photomultipliers for Underwater Wireless Optical Communication Links," in 10th International Symposium on Communication Systems, Networks and Digital Signal Processing (CSNDSP), 2016 IEEE, Jul 2016. (Cited on pages 21 and 59.)

[42] J. Tyler, "Radiance distribution as a function of depth in an underwater environment," *Bulletin of the Scripps Institution of Oceanography*, vol. 7, no. 5, pp. 363–412, 1960. (Cited on pages 22 and 39.)

[43] W. Cox and J. Muth, "Simulating channel losses in an underwater optical communication system," *Journal of the Optical Society of America A*, vol. 31, no. 5, pp. 920–934, May 2014. (Cited on page 22.)

[44] C. Wang, H. Y. Yu, and Y. J. Zhu, "A long distance underwater visible light communication system with single photon avalanche diode," *IEEE Photonics Journal*, vol. 8, no. 5, pp. 1–11, Oct 2016. (Cited on page 22.)

[45] F. R. Dalgleish, J. J. Shirron, D. Rashkin, T. E. Giddings, A. K. Vuorenkoski Dalgleish, I. Cardei, B. Ouyang, F. M. Caimi, and M. Cardeic, "Physical layer simulator for undersea free-space laser communications," *Optical Engineering*, vol. 53, no. 5, Apr. 2014. (Cited on pages 22 and 42.)

[46] M. Doniec, M. Angermann, and D. Rus, "An end-to-end signal strength model for underwater optical communications," *IEEE Journal of Oceanic Engineering*, vol. 38, no. 4, pp. 743–757, Oct. 2013. (Cited on pages 22, 27, 31, 34, 39 and 56.)

[47] E. W. Abrahamson, Ch. Baumann, C. D. B. Bridges, F. Crescitelli, H. J. A. Dartnall, R. M. Eakin, G. Falk, P. Fatt, T. H. Goldsmith, R. Hara, T. Hara, S. M. Japar, P. A. Liebman, J. N. Lythgoe, R. A. Morton, W. R. A. Muntz, W. A. H. Rushton, T. I. Shaw, and J. R. Wiesenfeld, T. Yoshizawa, *Photochemistry of Vision*. Herbert J. A. Dartnall, 1972. (Cited on pages 23 and 46.)

[48] S. Jaruwatanadilok, "Underwater wireless optical communication channel modeling and performance evaluation using vector radiative transfer theory," *IEEE Journal on Selected Areas in Communications*, vol. 26, no. 9, pp. 1620 – 1627, Dec. 2008. (Cited on page 24.)

[49] B. Cochenour, L. Mullen, and J. Muth, "Temporal response of the underwater optical channel for high-bandwidth wireless laser communications," *IEEE Journal of Oceanic Engineering*, vol. 38, no. 4, pp. 730–742, Oct. 2013. (Cited on pages 25, 29, 32, 39, 40 and 56.)

[50] W. C. Cox, *A 1 Mbps Underwater Communication System Using a 405 nm Laser Diode and Photomultiplier Tube*. Raleigh: M.S. thesis, North Carolina State University, 2007. (Cited on page 26.)

[51] H. M. Oubei, C. Li, K.-H. Park, T. K. Ng, M.-S. Alouini, and B. S. Ooi, "2.3 gbit/s underwater wireless optical communications using directly modulated 520 nm laser diode," *Opt. Express*, vol. 23, no. 16, pp. 20 743–20 748, Aug. 2015. (Cited on page 26.)

[52] M. H. K. Nakamura, I. Mizukoshi, "Optical wireless transmission of 405 nm, 1.45 gbit/s optical im/dd-ofdm signals through a 4.8 m underwater channel," *Opt Express*, vol. 23, no. 2, pp. 1558–1566, Jan. 2015, . (Cited on page 26.)

[53] C. Shen, Y. Guo, H. M. Oubei, T. K. Ng, G. Liu, K.-H. Park, K.-T. Ho, M.-S. Alouini, and B. S. Ooi, "20-meter underwater wireless optical communication link with 1.5 gbps data rate," *Opt. Express*, vol. 24, no. 22, pp. 25 502–25 509, Oct. 2016. (Cited on page 26.)

[54] *Thor Labs product: Visible Laser Diodes: Center Wavelengths from 404 nm to 690 nm*, https://www.thorlabs.com/. (Cited on page 27.)

[55] S. H. Y. Ito and M. Nakagawa, *Short-range underwater communication using visible light LEDs.* Tokyo, Japan: Tech. Rep., Dept. Sci. Technol., Keio Univ. (Cited on page 27.)

[56] N. Farr, A. Chave, L. Freitag, J. Preisig, S. White, D. Yoerger, and P. Titterton, "Optical modem technology for seafloor observatories," *OCEANS Conference*, pp. 1–6, Sep. 2006, Boston, MA. (Cited on pages 27, 29 and 40.)

[57] M. W. Doniec, I. Vasilescu, M. A. Chitre, C. Detweiler, D. Rus, and M. Hoffmann-Kuhnt, "Aquaoptical: A lightweight device for high-rate long-range underwater point-to-point communication," in *IEEE OCEANS Conference*, Oct. 2009, pp. 1–6, biloxi, MS. (Cited on pages 27, 29 and 34.)

[58] M. Doniec and D. Rus, "Bidirectional optical communication with AquaOptical II," in *International Conference on Communication Systems (ICCS)*, Nov. 2010, singapore. (Cited on pages 27 and 34.)

[59] D. Malacara and B. J. Thompson, *Handbook of Optical Engineering.* CRC Press, May 2001. (Cited on pages 27 and 28.)

[60] NICHIA Corporation, "Specifications for blue LED: NSPB510AS," *http://www.nichia.co.jp.* (Cited on pages 27, 83 and 101.)

[61] Dialight, "Getting to Know LEDs, Applications and Solutions," *www.dialight.com/*, 2008. (Cited on page 27.)

[62] C. Moursund, *LEDs vs. Laser Diodes for Wireless Optical Communication.* ClearMesh Networks, 2006. (Cited on page 27.)

[63] N. E. Farr, A. D. Bowen, J. D. Ware, C. Pontbriand, and M. A. Tivey, "An integrated, underwater optical/acoustic communications system," in *IEEE OCEANS Conference*, May 2010, pp. 1–6, sydney. (Cited on pages 27 and 34.)

[64] RP Photonics Encyclopedia, https://www.rp-photonics.com/laser_diodes.html. (Cited on page 28.)

[65] C. Kittel, *Introduction to solid state physics.* Wiley, 8th Edition, Nov. 2004. (Cited on page 28.)

[66] G. Cossu, R. Corsini, A. M. Khalid, S. Balestrino, A. Coppelli, A. Caiti, and E. Ciaramella, "Experimental demonstration of high speed underwater visible light communications," *International Workshop on Optical Wireless Communications (IWOW)*, pp. 11–15, Oct. 2013, Newcastle upon Tyne, UK. (Cited on pages 29, 31, 34, 39 and 49.)

[67] Sonardyne, "Sonardyne," *http://www.sonardyne.com/.* (Cited on pages 29, 33 and 56.)

[68] C. Gabriel, M. A. Khalighi, S. Bourennane, P. Léon, and V. Rigaud, "Investigation of suitable modulation techniques for underwater wireless optical communication," pp. 1–3, Oct. 2012, Pisa, Italy. (Cited on page 30.)

[69] Z. Ghassemlooy, A. Hayes, N. Seed, and E. Kaluarachchi, "Digital pulse interval modulation for optical communications," *IEEE Communications Magazine*, vol. 36, no. 12, pp. 95–99, Dec. 1998. (Cited on page 30.)

[70] T. Ohtsuki, "Multiple-subcarrier modulation in optical wireless communications," *IEEE Communications Magazine*, vol. 41, no. 3, pp. 74–79, Mar. 2003. (Cited on page 30.)

[71] B. Cochenour, L. Mullen, and A. Laux, "Phase coherent digital communications for wireless optical links in turbid underwater environment," in *Proc. OCEANS Conference*, 2007. (Cited on pages 31 and 34.)

[72] F. Xu, M. A. Khalighi, and S. Bourennane, "Impact of different noise sources on the performance of PIN- and APD-based FSO receivers," *COST IC0802 Workshop, IEEE ConTEL Conference*, pp. 211–218, June 2011, Graz, Austria. (Cited on pages 31, 41, 42, 43 and 44.)

[73] J. S. Everett, *Forward-Error Correction Coding for Underwater Free-Space Optical Communication*. Raleigh: M.S. thesis, North Carolina State University, 2009. (Cited on page 31.)

[74] J. A. Simpson, W. C. Cox, J. R. Krier, and B. Cochenour, "5 mbps optical wireless communication with error correction coding for underwater sensor nodes," in *OCEANS Conference*, Sep. 2010, Seattle, WA. (Cited on pages 31 and 34.)

[75] C. Gabriel, M. A. Khalighi, S. Bourennane, P. Léon, and V. Rigaud, "Misalignment considerations on point-to-point underwater wireless optical links," *IEEE Oceans Conference*, Jun. 2013, Bergen, Norway. (Cited on pages 32 and 34.)

[76] J. A. Simpson, B. L. Hughes, and J. F. Muth, "Smart Transmitters and Receivers for Underwater Free-Space Optical Communication," *IEEE Journal on Selected Areas in Communications*, vol. 30, no. 5, pp. 964–974, Jun. 2012. (Cited on pages 32 and 34.)

[77] W. W. Hou, "A simple underwater imaging model," *Opt. Lett.*, vol. 34, no. 17, pp. 2688–2690, Sep 2009. (Cited on page 32.)

[78] S. Woods, W. Hou, W. Goode, E. Jarosz, and A. Weidemann, "Measurements of turbulence for quantifying the impact of turbulence on underwater imaging," in *IEEE/OES 10th Current, Waves and Turbulence Measurements (CWTM)*, March 2011, pp. 179–183. (Cited on page 32.)

[79] W. G. E. J. W. Hou, S. Woods and A. Weidemann, "Impacts of optical turbulence on underwater imaging," *Proc. SPIE Ocean Sensing and Monitoring III*, vol. 8030, p. 803009, May 2011, . (Cited on page 32.)

[80] M. L. Holohan and J. C. Dainty, "Low-order adaptive optics: A possible use in underwater imaging?" *Optics and Laser Technology*, vol. 29, no. 1, pp. 51–55, Feb. 1997, . (Cited on page 32.)

[81] W. Liu, Z. Xu, and L. Yang, "Simo detection schemes for underwater optical wireless communication under turbulence," *Photon. Res.*, vol. 3, no. 3, pp. 48–53, Jun 2015. (Cited on page 32.)

[82] Y. Ata and Y. Baykal, "Structure functions for optical wave propagation in underwater medium," *Waves in Random and Complex Media*, vol. 24, no. 2, pp. 164–173, Feb. 2014. (Cited on page 32.)

[83] M. V. Jamali, J. A. Salehi, and F. Akhoundi, "Performance studies of underwater wireless optical communication systems with spatial diversity: Mimo scheme," *ArXiv e-prints*, Dec. 2016, provided by the SAO/NASA Astrophysics Data System. (Cited on page 32.)

[84] P. Kwatra, "Arq protocol studies in underwater communication networks," in *international Conference on Signal Processing and Communication (ICSC)*, Dec 2013, pp. 121–126. (Cited on page 33.)

[85] *Ambalux High Bandwidth Underwater Transceivers*, http://www.ambalux.com/underwater-transceivers.html. (Cited on page 33.)

[86] I. Vasilescu, K. Kotay, D. Rus, M. Dunbabin, and P. Corke, "Data collection, storage, and retrieval with an underwater sensor network," in *International Conference on Embedded networked sensor systems*, Nov. 2005, pp. 154–165, San Diego, CA. (Cited on page 34.)

[87] J. A. Simpson, B. L. Hughes, and J. F. Muth, "A spatial diversity system to measure optical fading in an underwater communications channel," in *OCEANS 2009*, Oct 2009, pp. 1–6. (Cited on page 34.)

[88] C. D. Mobley, "A numerical model for the computation of radiance distributions in natural waters with wind-roughened surfaces," *Limnology and Oceanography*, vol. 34, no. 8, pp. 1473–1483, 1989. (Cited on page 39.)

[89] T. Petzold, *Volume Scattering Functions for Selected Ocean Waters.* San Diego, CA, USA: Scripps Institute of Oceanography, 1972. (Cited on page 40.)

[90] Philips-LUMILEDS-Lighting-Company, "Luxeon rebel color portfolio datasheet ds68 20140527," *http://www.lumileds.com*, 2014. (Cited on pages 40 and 47.)

[91] J. M. Kahn and J. R. Barry, "Wireless infrared communication," *Proceedings of the IEEE*, vol. 85, no. 2, pp. 265–298, Feb. 1997. (Cited on pages xiii, 41, 113, 114 and 115.)

[92] R. Ramirez-Iniguez, S. M. Idrus, and Z. Sun, *Optical Wireless Communications: IR for Wireless Connectivity.* CRC Press, Avr. 2008. (Cited on page 41.)

[93] M. Kavehrad, M. I. S. Chowdhury, and Z. Zhou, *Fundamentals of Optical Wireless Communications, in Short-Range Optical Wireless: Theory and Applications.* Chichester, UK: John Wiley and Sons, Ltd, 2015. (Cited on page 41.)

[94] R. Toledo-Crow, S. Shi, and Y. Li, "Analysis of a two-PMT system for simultaneous back- and forward-fluorescence detection in multiphoton microscopy," *Biomedical Optics, Optical Society of America*, p. BMD56, 2008. (Cited on page 42.)

[95] B. E. A. Saleh and M. C. Teich, *Fundamentals of Photonics.* Wiley, Apr. 2007. (Cited on page 42.)

[96] M. A. Khalighi, F. Xu, Y. Jaafar, and S. Bourennane, "Double-laser differential signaling for reducing the effect of background radiation in free-space optical systems," *IEEE/OSA Journal of Optical Communications and Networking*, vol. 3, no. 2, pp. 145–154, Feb. 2011. (Cited on page 42.)

[97] R. M. Gagliardi and S. Karp, *Optical Communications (Second Edition).* Wiley, 1995. (Cited on page 42.)

[98] Hamamatsu, *Photomultiplier Tubes, Basics and Applications (Edition 3a).* HAMAMATSU PHOTONICS K. K, 2007. (Cited on pages 42, 43 and 47.)

[99] F. Qiang, *Encyclopedia of Atmospheric Sciences*, 2003, ch. Radiation (solar), pp. 1859 – 1863. (Cited on page 44.)

[100] T. Komine and M. Nakagawa, "Fundamental analysis for visible light communications using led lights," *IEEE transactions on Consumer Electronics*, vol. 50, no. 1, pp. 100–107, Feb. 2004. (Cited on page 47.)

[101] Hamamatsu, "R3896, R12896 High Sensitivity Multialkali Photocathode 28 mm (1-1/8 Inch) Diameter, 9-Stage, Side-On Type," *http://www.hamamatsu.com.* (Cited on page 47.)

[102] W. C. Cox, *Simulation, Modeling and Design of Underwater Optical Communication Systems.* Raleigh, North Carolina, USA: PhD Thesis, North Carolina University, 2012. (Cited on page 48.)

[103] S. R. Z. Ghassemlooy and W. Popoola, *Optical Wireless Communications: System and Channel Modelling with MATLAB.* CRC Press, 2013. (Cited on page 48.)

[104] "ITU-T Recommendation G.975.1," (02/2004). (Cited on page 49.)

[105] A. H. Az-ar, T.-A. Tran, and D. O'Brien, "A Gigabit/s indoor wireless transmission using MIMO-OFDM visible-light communications," *IEEE Photonics Technology Letters*, vol. 25, no. 2, pp. 171–174, Jan. 2013. (Cited on page 49.)

[106] SensL, "Introduction to the Silicon Photomultiplier, Technical Note," *http://www.sensl.com/*, 2011. (Cited on pages xv, 55, 56, 57, 60 and 64.)

[107] G. Baiden, Y. Bissiri, and A. Masoti, "Paving the way for a future underwater omni-directional wireless optical communication systems," *Ocean Engineering*, vol. 36, no. 9, pp. 633–640, 2009. (Cited on page 56.)

[108] N. Otte, "The Silicon Photomultiplier - a new device for high energy physics, astroparticle physics, industrial and medical applications," in IX International Symposium on Detectors for Particle, Astroparticle and Synchrotron Radiation Experiments, SNIC Symposium, Stanford, California, Apr. 2006, pp. 1–9. (Cited on pages 57 and 58.)

[109] Hamamatsu, "Opto-semiconductor handbookChapter 03 Si APD, MPPC," *http://www.hamamatsu.com*, 2014. (Cited on page 57.)

[110] Hamamatsu Photonics, "S10362-11-025P Mppc Multi-pixel Photon Counter pdf datasheet." *http://www.datasheetlib.com/*, 2010. (Cited on page 57.)

[111] I. Alsolami, D. Chitnis, D. C. O'Brien, and S. Collins, "Broadcasting over photon-counting channels via multiresolution ppm: Implementation and experimental results," *IEEE Communications Letters*, vol. 16, no. 12, pp. 2072–2074, Dec 2012. (Cited on page 57.)

[112] G. Zhang, C. Yu, C. Zhu, and L. Liu, "Feasibility study of Multi-Pixel Photon Counter serving as the detector in digital optical communications," *Optik - International Journal for Light and Electron Optics*, vol. 124, no. 22, pp. 5781 – 5786, 2013. (Cited on page 57.)

[113] D. Chitnis and S. Collins, "A SPAD-Based Photon Detecting System for Optical Communications," *Journal of Lightwave Technology*, vol. 32, no. 10, pp. 2028–2034, May 2014. (Cited on page 57.)

[114] Y. Li, S. Videv, M. Abdallah, K. Qaraqe, M. Uysal, and H. Haas, "Single photon avalanche diode (SPAD) VLC system and application to downhole monitoring," in *Global Communications Conference (GLOBECOM), 2014 IEEE*, Dec 2014, pp. 2108–2113. (Cited on pages 57, 61 and 65.)

[115] Y. Li, M. Safari, R. Henderson, and H. Haas, "Optical OFDM with single-photon avalanche diode," *Photonics Technology Letters, IEEE*, vol. 27, no. 9, pp. 943–946, May 2015. (Cited on page 57.)

[116] Y. Li, M. Safari, R. Henderson, and H. Haas, "Nonlinear distortion in SPAD-based optical OFDM systems," *Global Telecommunications (Globecom) Conference, Workshop on Optical Wireless Communications*, Dec. 2015, San Diego, CA, USA. (Cited on pages 57, 59, 60, 61 and 62.)

[117] D. Chitnis, L. Zhang, H. Chun, S. Rajbhandari, G. Faulkner, D. O'Brien, and S. Collins, "A 200 Mb/s VLC demonstration with a SPAD based receiver," in *2015 IEEE Summer Topicals Meeting Series (SUM)*, July 2015, pp. 226–227. (Cited on page 57.)

[118] Kektek, "Products Â» SiPM Technology Â» Working Principle," *http://www.ketek.net/*, 2016. (Cited on pages 58 and 60.)

[119] X. Chen, *Study of the Silicon Photomultipliers and Their Applications in Positron Emission Tomography.* Hamburg University: PhD Thesis, 2014. (Cited on page 59.)

[120] ID Quantique, "ID150 VIS 8 Channel SPAD : Miniature 8-channel photon counter for OEM applications ," *http://www.idquantique.com*, 2010. (Cited on pages 59 and 71.)

[121] SensL, "B-Series Fast, Blue-Sensitive Silicon Photomultiplier Sensors Datasheet," *http://www.sensl.com/*, 2013. (Cited on pages 59, 65 and 71.)

[122] A. Eisele, R. Henderson, B. Schmidtke, T. Funk, L. Grant, J. Richardson, and W. Freude, "185 mhz count rate, 139 db dynamic range single-photon avalanche diode with active quenching circuit in 130nm cmos technology," *International Image Sensor Workshop*, pp. 278–281, Jun. 2011, Japan. (Cited on pages 62 and 63.)

[123] S. Donati and T. Tambosso, "Single-photon detectors: From traditional pmt to solid-state spad-based technology," *IEEE Journal of Selected Topics in Quantum Electronics*, vol. 20, no. 6, pp. 204–211, Nov 2014. (Cited on page 63.)

[124] WET Labs, "C-Star Brochure," *http://wetlabs.com/cstar*, Jun. 2010. (Cited on page 64.)

[125] S. G. Wilson, *Digital Modulation and Coding.* Prentice Hall, Aug. 1995. (Cited on page 71.)

[126] S. Long, M. A. Khalighi, M. Wolf, Z. Ghassemlooy, and S. Bourennane, "Performance of carrier-less amplitude and phase modulation with frequency domain equalization for indoor visible light communications," Sep. 2015, pp. 16–20, Istanbul, Turkey. (Cited on pages 79, 81 and 83.)

[127] S. U. H. Qureshi, "Adaptive equalization," *Proceedings of the IEEE*, vol. 73, no. 9, pp. 1349–1387, Sept 1985. (Cited on page 80.)

[128] L. Hong, *PhD thesis: Frequency-domain equalization of single carrier transmissions over doubly selective channels.* Ohio State University, Nov. 2016, Retrieved from https://etd.ohiolink.edu/ . (Cited on page 80.)

[129] D. Falconer, S. L. Ariyavisitakul, A. Benyamin-Seeyar, and B. Eidson, "Frequency domain equalization for single-carrier broadband wireless systems," *IEEE Communications Magazine*, vol. 40, no. 4, pp. 58–66, Apr 2002. (Cited on pages 80, 81 and 90.)

[130] S. Dimitrov, S. Sinanovic, and H. Haas, "Clipping noise in ofdm-based optical wireless communication systems," *IEEE Transactions on Communications*, vol. 60, no. 4, pp. 1072–1081, April 2012. (Cited on page 80.)

[131] J. Vucic, C. Kottke, S. Nerreter, K. D. Langer, and J. W. Walewski, "513 mbit/s visible light communications link based on dmt-modulation of a white led," *Journal of Lightwave Technology*, vol. 28, no. 24, pp. 3512–3518, Dec 2010. (Cited on page 81.)

[132] G. Cossu, A. M. Khalid, P. Choudhury, R. Corsini, and E. Ciaramella, "3.4 gbit/s visible optical wireless transmission based on rgb led," *Opt. Express*, vol. 20, no. 26, pp. B501–B506, Dec 2012. (Cited on page 81.)

[133] D. Tsonev, H. Chun, S. Rajbhandari, J. J. D. McKendry, S. Videv, E. Gu, M. Haji, S. Watson, A. E. Kelly, G. Faulkner, M. D. Dawson, H. Haas, and D. O'Brien, "A 3-Gb/s Single-LED OFDM-Based Wireless VLC Link Using a Gallium Nitride μLED ," *IEEE Photonics Technology Letters*, vol. 26, no. 7, pp. 637–640, April 2014. (Cited on page 81.)

[134] A. M. Khalid, G. Cossu, R. Corsini, P. Choudhury, and E. Ciaramella, "1-gb/s transmission over a phosphorescent white led by using rate-adaptive discrete multitone modulation," *IEEE Photonics Journal*, vol. 4, no. 5, pp. 1465–1473, Oct 2012. (Cited on page 81.)

[135] Centronic Co., "Silicon Photodetector OSD1-5T datasheet," *http://www.centronic.co.uk*. (Cited on page 83.)

[136] SensL, "B-Series Fast, Blue-Sensitive Silicon Photomultiplier Sensors USER MANUAL," *http://www.sensl.com/*, 2013. (Cited on pages xii, 83, 84 and 102.)

[137] Model PM8572A : 50MHz Dual-Channel Pulse Waveform Generator, http://www.taborelec.com/pm8572a/. (Cited on page 101.)

[138] LeCroy website, http://www.lecroy.com/. (Cited on page 102.)

Efficient Transmission and Tracking techniques for Underwater Optical Communications

Abstract: Today we are witnessing a growing need to high-rate data transmission in underwater missions in a wide range of application areas. Within this context, traditional cable- or fiber-based communications imply costly deployments with very limited flexibility, andthe conventional acoustic communications offer very low operational performance. Recently, with the development of small and low-cost optoelectronic components and devices, it has become feasible to realize small and compact wireless optical communication transceivers providing unprecedentedly high transmission rates and energy efficiency. However, there still remain several shortcomings of this technology, in particular to attain high data rates over relatively long communication ranges.In order to overcome some of these limitations, this PhD thesis considers the use of advanced optoelectronic components and signal processing techniques in order to improve the performance of underwater wireless optical communication (UWOC) links.
Keywords: Underwater optical communications, signal processing, digital communications, optronics, Silicon photo-multipliers.

Communications optiques sous-marines : Transmission longue-portée haut-débit et analyse des performances

Résumé: Aujourd'hui, un large éventail d'activités d'exploration et d'exploitation du milieu sous-marin requière l'établissement de transmissions de données à haut débit. Dans ce contexte, les solutions de communications traditionnelles par câble ou par fibre optique impliquent des déploiements coûteux et une flexibilité trs limitée. D'autre part, les communications acoustiques offrent des performances opérationnelles trs faibles. Récemment, avec le développement de composants optoélectroniques compacts et peu coûteux, il est devenu possible de réaliser des modems optique pour les communications sans-fil, qui soient compacts et offrent des vitesses de transmission et une efficacité énergétique sans précédentes. Cependant, cette technologie souffre encore de plusieurs limitations, notamment quand il s'agit d'établir des liens de communication sur des distance relativement longues et à des débits de transmission élevés. Pour faire face à certaines de ces faiblesses, cette thse considre l'utilisation de nouveaux composants optoélectroniques et des techniques de traitement du signal adaptées afin d'améliorer les performances des liaisons de communication optique sans fil sous-marine.
Mots clés: Communications optiques sous-marines, traitement du signal, communications numériques, optroniques, Photo-multiplicateurs en Silicium.
